Electrochemical Reduction of Carbon Dioxide to the Value-Added Product Ethanol

Elektrochemische Reduktion von Kohlenstoffdioxid zum wertgesteigerten Produkt Ethanol

Von der Fakultät für Mathematik, Informatik und Naturwissenschaften der RWTH Aachen Universität zur Erlangung des akademischen Grades einer Doktorin der Naturwissenschaften genehmigte Dissertation

vorgelegt von

Elisabeth Gräfin von Westarp, M.Sc.

geborene Robens

aus

Neuss

Berichter: Univ.-Prof. Dr. rer. nat. Rüdiger-Albert Eichel
Univ.-Prof. Dr. rer. nat. Joachim Mayer

Tag der mündlichen Prüfung: 16.12.2024

Diese Dissertation ist auf den Internetseiten der Universitätsbibliothek verfügbar.

b

Eidesstattliche Erklärung

Ich, Elisabeth Gräfin von Westarp, erkläre hiermit, dass diese Dissertation und die dargelegten Inhalte die eigenen sind und selbstständig, als Ergebnis der eigenen originären Forschung, generiert wurden.

Hiermit erkläre ich an Eides statt:

1. Diese Arbeit wurde vollständig oder größtenteils in der Phase als Doktorand dieser Fakultät und Universität angefertigt;

2. Sofern irgendein Bestandteil dieser Dissertation zuvor für einen akademischen Abschluss oder eine andere Qualifikation an dieser oder einer anderen Institution verwendet wurde, wurde dies klar angezeigt;

3. Wenn immer andere eigene- oder Veröffentlichungen Dritter herangezogen wurden, wurden diese klar benannt;

4. Wenn aus anderen eigenen- oder Veröffentlichungen Dritter zitiert wurde, wurde stets die Quelle hierfür angegeben. Diese Dissertation ist vollständig meine eigene Arbeit, mit der Ausnahme solcher Zitate;

5. Alle wesentlichen Quellen von Unterstützung wurden benannt;

6. Wenn immer ein Teil dieser Dissertation auf der Zusammenarbeit mit anderen basiert, wurde von mir klar gekennzeichnet, was von anderen und was von mir selbst erarbeitet wurde;

7. Ein Teil oder Teile dieser Arbeit wurden zuvor veröffentlicht. Eine Auflistung befindet sich unter „Publications“.

Ort, Datum, Unterschrift

d

Danksagung

Sehr geehrter Professor Eichel, ich möchte mich herzlich bei Ihnen bedanken, dass Sie mich im Rahmen Ihrer Vorlesung „Elektrochemische Speicher und Wandler“ und den anschließenden Diskussionen auf den Pfad der Elektrochemie geführt haben. Mit der Möglichkeit, eines meiner Forschungspraktika bei Ihnen am Institut absolvieren zu dürfen, begann meine Zeit am IEK-9 (heute IET-1), die nun mit dem Abschluss meiner Doktorarbeit endet. Ich möchte mich jedoch nicht nur für die wissenschaftlichen Möglichkeiten bedanken, sondern auch dafür, dass Sie mir die Chance gegeben haben, in die Welt außerhalb der Wissenschaft hineinzuschnuppern, beispielsweise im Rahmen des Parlamentarischen Frühstücks im Landtag in Düsseldorf - vielen Dank!

Sehr geehrter Professor Mayer, vielen Dank, dass Sie sich bereit erklärt haben, doch relativ spontan mein Zweitprüfer zu werden und somit meine Doktorprüfung ermöglicht haben. Mit Ihrer Antwort innerhalb von 12 Minuten haben Sie bei mir den Rekord für die schnellste jemals erhaltenen Antwort eines Professors aufgestellt - vielen Dank!

Lieber Hermann, als Teil deiner Abteilung konnte ich mich als Wissenschaftlerin entwickeln. Du hast mir den Freiraum gegeben, um zu wachsen, und gleichzeitig durch deine Erfahrung und Vorschläge meine Forschung unterstützt - vielen Dank!

Lieber Burkhard, ohne dich wäre meine Doktorarbeit so nie möglich gewesen. Du hast mich sowohl theoretisch als auch fachlich in das Thema der CO_2 Elektrolyse eingearbeitet und standest mir immer mit Rat und Tat zur Seite. Du standest aber auch immer hinter mir, und ich konnte auf deine Unterstützung zählen. Neben dem Fachlichen werde ich mich aber auch immer mit Freude an unsere Koordinationsmeetings erinnern - vielen Dank!

Liebe Kollegen, es heißt, dass bei einem Job nicht nur das fachliche Thema passen muss, sondern auch das berufliche Umfeld besonders wichtig ist, um sich wohlzufühlen. Das habt ihr geschafft, und dafür möchte ich euch von Herzen danken. Besonders hervorheben möchte ich meine C2/C3-Untergruppe mit Burkhard, Deniz, Albert und Darius, meine Bürokollegen Marcel und Henrike, meine Fahrgemeinschaft mit Ansgar, Victor, Steffi und Bea sowie den IEK-9lern in 9.7 und friends - vielen Dank euch allen!

Lieber Igor, du warst mir die ganze Zeit über eine große Stütze, und ich konnte mich immer darauf verlassen, dass du an meiner Seite bist. Du hast mit mir Erfolge gefeiert, aber mich auch in schwierigeren Phasen immer wieder aufgebaut - vielen lieben Dank!

f

Publications

Parts of this thesis are based on the following publications:

- **Power-to-Ethanol using Bimetallic Catalysts: Reactions Paths, Transfer to Gas Diffusion Electrode, and Future Perspectives**
  Elisabeth Gräfin von Westarp, Burkhard Hecker, Hermann Tempel, Rüdiger-A. Eichel
  Electrochemical Science Advances, **2024**, 1-7.

  Contribution: Elisabeth Gräfin von Westarp (née Robens) is the main contributor to this publication: The literature research, the experiments, data evaluation and interpretation, as well as the writing of the paper were performed by her.

  Parts of chapters 2 and 4.3 are based on this publication.

- **Bimetallic Copper-Silver Catalyst for the Electrochemical Reduction of CO_2 to Ethanol**
  Elisabeth Robens, Burkhard Hecker, Hans Kungl, Hermann Tempel, Rüdiger-A. Eichel
  ACS Appl. Energy Mater., **2023**, *6*, 7571-7577.

  Contribution: Elisabeth Gräfin von Westarp (née Robens) is the main contributor to this publication: She conducted all experiments, except of the ICP-MS and XPS measurements, which were done by ZEA 3, and was responsible for data evaluation and interpretation, as well as writing the paper.

  Parts of chapters 3.2.1, 3.2.3, 3.4, and 4.2 are based on this publication.

Additional publication that the author worked on:

- **Effects of Synthesized Silver Nanoplate Structures on the Electrochemical Reduction of CO_2**
  Burkhard Hecker, Elisabeth Robens, Helen E. Valencia, Anna Windmüller, Falk Muench, Maria Meledina, Hermann Tempel, Hans Kungl, Joachim Mayer, Rüdiger-A. Eichel
  J. Electrochem. Soc., **2023**, *170*, 096505.

Contribution: Elisabeth Gräfin von Westarp (née Robens) developed the synthesis for the bead-like silver structure, performed CO_2 reduction reaction experiments of plate- and bead-like silver structures and evaluated them. In collaboration with Dr. Burkhard Hecker she performed the Lead Underpotential Deposition measurements.

Conference Contributions

- Poster: **Bimetallic Catalyst for CO_2 Reduction to Ethanol**
  Elisabeth Robens, Burkhard Hecker, Hans Kungl, Hermann Tempel, Rüdiger-A. Eichel
  4th ELECTRA Symposium, 14 September - 15 September 2023, Jülich, Germany

- Presentation: **Copper-Silver Catalyst for Electrochemical Reduction of CO_2 to Ethanol**
  Elisabeth Robens, Burkhard Hecker, Hans Kungl, Hermann Tempel, Rüdiger-A. Eichel
  20th International Conference on Carbon Dioxide Utilization – ICCDU, 25-29 June 2023, Bari, Italy

- Poster: **New Bimetallic Catalyst for CO_2 Reduction to Ethanol**
  Elisabeth Robens, Burkhard Hecker, Hans Kungl, Hermann Tempel, Rüdiger-A. Eichel
  GDCh Electrochemistry – At the interface between Chemistry and Physics, 27-30 September 2022, Berlin, Germany

- Presentation: **New Bimetallic Catalyst for CO_2 Reduction to Ethanol**
  Elisabeth Robens Burkhard Hecker, Hans Kungl, Hermann Tempel, Rüdiger-A. Eichel
  3rd ELECTRA Symposium, 31 August - 1 September 2022, Aachen, Germany

- Poster: **Study of New Bimetallic Cu-Ag Catalyst for CO_2 Reduction**
  Elisabeth Robens, Burkhard Hecker, Hans Kungl, Hermann Tempel, Rüdiger-A. Eichel
  10th International Conference "Fuel Science – From Production to Propulsion" – FSC, 10-12 May 2022, Aachen, Germany

j

Kurzfassung

Um dem deutlich sichtbaren Klimawandel entgegenzuwirken, ist es wichtig, die lineare Kohlenstoffwirtschaft in einen Kohlenstoffkreislauf umzuwandeln. Ein vielversprechender Ansatz ist die elektrochemische CO_2 Reduktionsreaktion (CO_2RR). Um diese Technologie zeitnah wirtschaftlich zu machen, wird ein wertsteigerndes Produkt benötigt, das die hohen Anfangskosten ausgleicht. Ein mögliches Produkt ist Ethanol. Die Herstellung von Ethanol mittels CO_2RR ist jedoch herausfordern, da unter anderem die Konkurrenz zur Ethylenbildung die selektive Ethanolbildung erschwert.

In dieser Doktorarbeit wird ein neuer bimetallischer Katalysator hergestellt, der diese Herausforderung angeht. Er besteht aus Silber-Nanoplättchen (Ag NPls), die teilweise mit Kupfer beschichten sind (CuAg NPls). Durch die Verringerung des oberflächennahen Kupfergehaltes von 99 % auf 45 % bei einer Stromdichte von -20 mA cm^{-2} erhöht sich die Faraday Effizienz von Ethanol von 5 % auf 23 %, und das Ethanol-Ethylene-Verhältnis steigt von 0,4 auf 2,6. Diese Verbesserung wird dem Überschuss an *CO zugeschrieben, der durch den erhöhten Silberanteil entsteht und einen alternativen und selektiven Reaktionsweg für Ethanol eröffnet.

Diese Studie wurde jedoch in einem H-Typ-Elektrolyseur durchgeführt, bei dem der Massentransport begrenzt ist und die Stromdichten daher unzureichend sind. Um dieses Problem zu lösen, wird der untersuchte Katalysator in eine Gasdiffusionselektrode übertragen, bei der der Diffusionsweg für CO_2 kürzer ist. Vorab werden kommerzielle Kupfernanopartikel in beiden Aufbauten untersucht, um die Vergleichbarkeit der Daten zu testen. Diese Messungen zeigen, wie wichtig es ist, das jeweilige Potenzial an der Arbeitselektrode zu kennen, um festzustellen, ob gemessene Unterschiede bei der Produktbildung auf die Systeme selbst oder auf mögliche unterschiedliche Potenziale zurückzuführen sind.

Anschließend wird die Hauptstudie zum Transfer der CuAg NPls in eine Gasdiffusionselektrode durchgeführt. Zunächst werden nur Produkte detektiert, die auf den Silberteil des Katalysators zurückzuführen sind, während die katalytischen Eigenschaften des Kupfers nicht sichtbar sind. Diese Beobachtung wird den sauren Eigenschaften von Nafion zugeschrieben, die das abgeschiedene Kupfer korrodieren. Durch die Verwendung eines weniger sauren Binders können die Kupfereigenschaften erhalten werden. Der Wechsel von einer statischen Zelle zu einer Durchflusszelle ermöglicht zudem die konstante Bildung von Alkoholen über den Messzeitraum. Zudem bieten Untersuchungen an reinen Ag NPls interessante Ansätze für zukünftige Arbeiten, wie die Aktivierung durch einen Stromimpuls oder den „Druckmodus“.

l

Abstract

In order to counteract the climate change that is clearly visible today, it is essential to transform the linear carbon economy to a circular economy. A promising approach to accomplish this task is the electrochemical CO_2 reduction reaction (CO_2RR). For near-term feasibility of this technology, a value-added product is needed to overcome the high initial costs. Ethanol can serve this purpose. However, ethanol formation via CO_2RR faces several challenges, one of which is that it competes with ethylene evolution, making it difficult to selectively produce ethanol.

This thesis addresses the presented challenge with a new bimetallic catalyst. It consists of silver nanoplates (Ag NPls) partially covered with copper, referred to as copper-silver nanoplates (CuAg NPls). By decreasing its near-surface copper content from 99 % to 45 % at a current density of -20 mA cm^{-2}, the Faradaic efficiency of ethanol is enhanced from 5 % to 23 %. Concurrently, the ethanol-to-ethylene ratio increases from 0.4 to 2.6. This improvement is attributed to the abundant *CO provided by the increased silver content, which activates an alternative and selective reaction path for ethanol.

However, this study is carried out in an H-type electrolyzer, which has mass transport limitations and thus insufficient current densities. To address this issue, the studied catalyst is transferred to a gas diffusion electrode, where the diffusion path for CO_2 is shorter. As preliminary work, commercial copper nanoparticles are investigated in both setups to test the comparability of data from these two cell designs. These measurements highlight the importance of knowing the respective potential at the working electrode to determine whether the differences in product formation are due to the systems themselves or to possible different potentials.

Subsequently, the main study on the transfer of the CuAg NPls into a gas diffusion electrode is carried out. Initially, only the formation of products associated to the silver part of the catalyst are detected, with no catalytic copper properties visible. This observation is attributed to the acidity of Nafion, which corrodes the copper deposited on the Ag NPls. To address this issue, a less acidic binder is used, which allows to maintain the copper properties. By switching from a static cell to a flow cell, it is also possible to constantly form alcohols over the measurement period. Furthermore, investigations on pure Ag NPls are performed, which provide interesting solutions for future work, such as activation through a current pulse or the “pressure-mode”.

n

Contents

1 Motivation **1**

2 Theoretical Background **3**
2.1 Electrochemical CO_2 Reduction Reaction 3
2.2 Ethanol as Target Product 11
2.3 Cell Concepts for the CO_2 Reduction Reaction 12
2.3.1 H-Type Electrolyzer 12
2.3.2 Liquid-Phase Electrolyzer 13
2.3.3 Structure and Manufacturing Techniques of Gas Diffusion Electrodes 17
2.4 Electrochemical Basics and Formulas 19

3 Experimental **21**
3.1 Chemicals 21
3.2 H-Type Electrolyzer 22
3.2.1 Catalyst Synthesis 22
3.2.2 Electrode Preparation 24
3.2.3 CO_2 Reduction Reaction 25
3.3 Liquid-Phase Electrolyzer 28
3.3.1 Catalyst Synthesis 28
3.3.2 Electrode Preparation 28
3.3.3 CO_2 Reduction Reaction 30
3.4 Catalyst Characterization 32
3.4.1 Scanning Electron Microscopy 33
3.4.2 X-Ray Diffraction 33
3.4.3 Inductively Coupled Plasma Mass Spectrometry 33
3.4.4 X-Ray Photoelectron Spectroscopy 34

4 Results and Discussion **35**
4.1 Optimization of H-Type Electrolyzer 35
4.2 Investigation of CuAg NPls in H-Type Electrolyzer 40
4.2.1 Catalyst Morphology, Composition, and Activity 40
4.2.2 Catalytic Performance in CO_2RR 44
4.3 Transfer of Catalyst to Gas Diffusion Electrode 48
4.3.1 Influence of the Cell Design on Commercial Cu NPs 49
4.3.1.1 Performance of Cu NPs in H-Type Electrolyzer 49

4.3.1.2 Performance of Cu NPs in Static Liquid-Phase Electrolyzer . . . 56
4.3.2 Investigation of CuAg NPls in FlexCell . . . 59
4.3.2.1 Modification of Synthesis and Manufacturing of GDE . 59
4.3.2.2 Catalytic Performance in CO_2RR . . . 60
4.3.3 Investigation of Pure Ag NPls – Inspiration for Future Experiments . . . 70

5 Conclusion **77**

Bibliography **81**

A List of Abbreviations and Symbols **89**

B List of Figures **93**

C List of Tables **101**

1 Motivation

Climate change and its impact on our lives are clearly visible today. It is recognizable by more floods, droughts, heat, and storms around the world. In its report from 2023, the Intergovernmental Panel on Climate Change (IPPC) cites the drastic increase in carbon dioxide (CO_2) emissions in recent decades as the reason for sea level rise and global warming.[1] If not rethought and acted upon, global warming may increase by a value of 2.8 °C by 2100. To meet the goal of limiting global warming to 1.5 °C, CO_2 emissions must be substantially reduced. And even a net-zero emission target must be pursued, since the CO_2 budget for the 1.5 °C target is already nearly depleted.[1] Therefore, it is our responsibility as a society to find suitable solutions to achieve the net zero emission target.

A very straight-forward approach would be to avoid the formation of CO_2. However, this is not easy to implement in all sectors, for instance, in aviation, long-distance transport, shipping, and the production of steel and cement.[2] Therefore, an alternative idea is also needed, namely the capture of formed and emitted CO_2 so that the net emission is still zero. Storage of captured CO_2, for example in underground caves, is termed "carbon capture and storage" (CCS).[2,3] However, it is also possible not only to store the CO_2, but to reuse it, which is referred to as "carbon capture and utilization" (CCU).[3,4] This would lead to a shift from a linear to a more circular carbon economy, so CCU is an opportunity to close the anthropogenic carbon cycle.[4]

However, CO_2 is a highly inactive species due to its thermodynamic stability.[5,6] Therefore, CO_2 must first be activated before it can be recycled. There are several ways to activate and recycle captured CO_2, for instance, by bioconversion, photoreduction, and by electrochemical and thermochemical processes.[4,7] In this work, the electrochemical reduction of CO_2 is used. This allows two advantages to be combined: By using renewable energy sources such as wind and solar energy, the waste product CO_2 can be converted into a carbon-neutral chemical feedstock that can be used for chemicals and e-fuels.[8–10] In addition, the energy from these intermittent energy sources can be stored in the chemical bonds of the resulting products.[4] Thus, the CO_2RR can be used as a long-term energy storage system with a high storage capacity, which also helps to stabilize the energy grid.[7,11] However, there are still challenges that need to be overcome in order to use this technology in larger applications, such as the stability and selectivity of the electrocalyst, the efficiency of the cell system, and the need to expand renewable energy sources.

In one sentence, then, it can be said that CO_2RR could be one piece of the complex

puzzle of achieving the net-zero emission target, so it is worthwhile to continue and intensify research on this topic.

2 Theoretical Background

This chapter is based on the publication "Power-to-Ethanol using Bimetallic Catalysts: Reactions Paths, Transfer to Gas Diffusion Electrode, and Future Perspectives".[12] To form this chapter, the publication is supplemented with additional parts and information.

2.1 Electrochemical CO_2 Reduction Reaction

This section provides an overview of the electrochemical reduction of CO_2 by covering the reaction equations and the impact of the utilized electrocatalyst. In more detail, the use of copper (Cu) and bimetallic cathodes is discussed.

For the CO_2RR, an electrolysis cell is needed while CO_2 and water are used as reactants (see figure 1). On the cathode side, the desired CO_2RR takes place according to equation (1).

$$x\mathrm{CO_2} + k\mathrm{H_2O} + z\mathrm{e^-} \quad \longrightarrow \quad \text{product} + y\mathrm{OH^-} \tag{1}$$

Which product is formed depends strongly on the used electrocatalyst. This impact was already measured in 1993, which resulted in a categorization of pure metal electrodes into four groups: In the first group, consisting of nickel (Ni), iron (Fe), platinum (Pt), and titanium (Ti), no or only a small amount of CO_2RR takes place and hydrogen (H_2) is formed instead. In contrast, gold (Au), silver (Ag), and zinc (Zn) mainly invoke carbon monoxide (CO) formation (second group), while tin (Sn), bismuth (Bi), and lead (Pb) produce formate (third group). The only pure metal which can form hydrocarbons and alcohols, e.g. ethylene and ethanol, in significant quantities is Cu, which thus represents the fourth group.[13,14]

The CO_2RR is always in competition with the parasitic hydrogen evolution reaction (HER) due to the aqueous electrolyte.[15–17]

$$2\mathrm{H_2O} + 2\mathrm{e^-} \quad \longrightarrow \quad \mathrm{H_2} + 2\mathrm{OH^-} \tag{2}$$

As anodic reaction, often the well-known oxidation of water to oxygen is used. However, in order to improve the overall energy conversion efficiency and to increase the economic benefits of the process, other anodic reactions are also being investigated,

namely chloride oxidation, organic synthesis, waste water treatment, and convergent reactions.[18] Since this study focuses only on the cathodic half cell reaction and not on the overall performance, the well-known oxygen evolution reaction (OER) is used as anodic reaction (equation (3)).

$$2H_2O \longrightarrow O_2 + 4H^+ + 4e^- \tag{3}$$

By combination of cathode and anode reaction, the following overall reaction is obtained:

$$xCO_2 + lH_2O \longrightarrow \text{product} + pO_2 \tag{4}$$

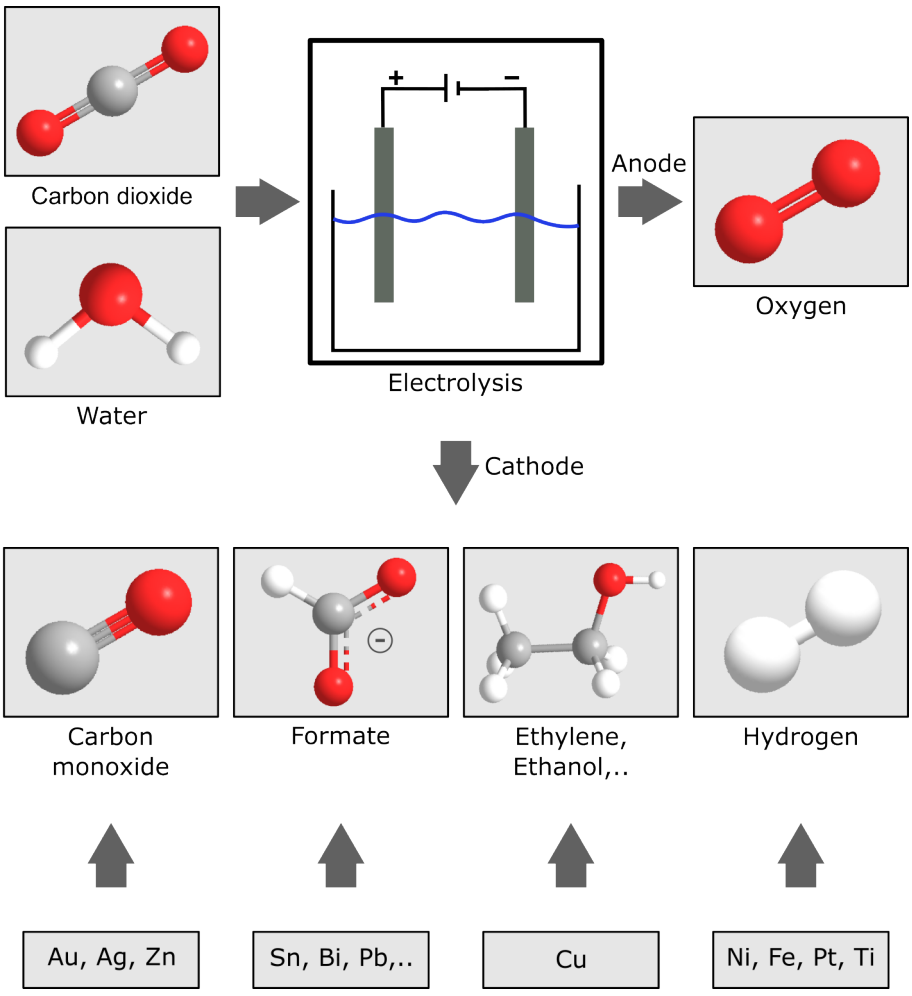

Figure 1: Schematic diagram of CO_2 electrolysis showing the reactants and formed products on the anode and cathode sides. The influence of pure metal electrocatalysts on the product formation is also illustrated.

As mentioned above, Cu is the only pure metal that can produce CO_2RR products beyond CO and formate with significant Faradaic efficiency (FE), namely methane, methanol, and C_{2+} products.[13] This behaviour can be explained by binding energies (see figure 2). For the formation of products other than CO and formate, adsorbed CO is the key intermediate.[3] Therefore, the binding energy of CO to the cathode is important. A distinction can be made between weak (depicted in blue and yellow), moderate (depicted in turquoise), and strong (depicted in red) binding energy. If a weak binding energy is present, either the formed CO desorbs from the cathode and cannot react further or no CO is formed at all and formate is produced instead. The former is the case for CO-forming materials such as Au and Ag, whereas the latter applies to, for example, Sn and Bi cathodes. On the other hand, if there is a strong bond between adsorbed CO and the cathode, poisoning of the cathode occurs. In this case, a higher overpotential is necessary for a further reduction of CO. However, typically HER is then favored and only H_2 would be formed, as it is the case for, e.g., Ni and Pt. Therefore, a moderate binding energy is required for further reduction of adsorbed CO to methane, methanol, and C_{2+} products. Since this is only the case for Cu, it is the only pure metal that can form these products in significant quantities.[19–21]

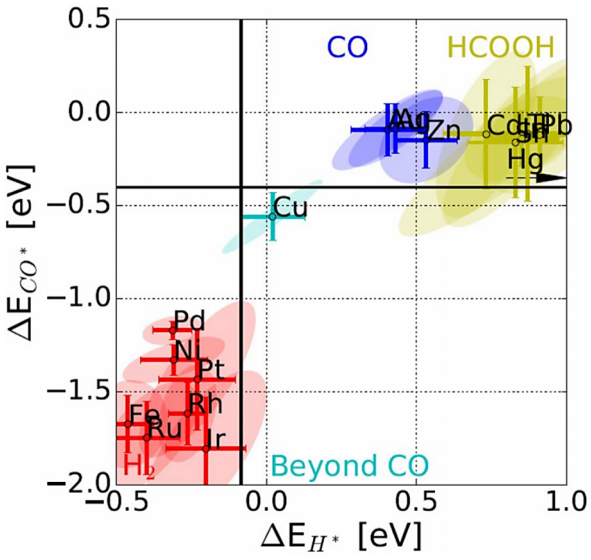

Figure 2: Computed binding energies of adsorbed CO and H on different metal catalysts. The metals that form H_2, CO, or formate are depicted in red, blue, and yellow, respectively. In turquoise, Cu is marked as material forming products beyond CO. The black lines represent the boundaries between adsorbed and non-adsorbed H or CO.[20] Clearance was granted via the licence number 5811940310401.

Many different CO_2RR products can be detected with Cu electrodes. In one publication, for example, 16 different products were found, which are listed in table 1.[22] In addition to the name of the products, the amount of CO_2 (x), H_2O (k), trans-

ferred electrons (z), and OH^- (y) required per molecule of product are specified. The standard reduction potential is also given. This study further investigated the overpotential at which the various products are formed (see figure 3). At low overpotentials ($E >$ -0.75 V *vs.* reversible hydrogen electrode (RHE)), the HER is preferred over the CO_2RR. The only CO_2RR products are CO and formate. CO cannot be further reduced because the binding energy between CO and Cu is not sufficient at this overpotential. With increasing overpotential, the formation of H_2 decreases and more CO_2RR products are formed. Moreover, products other than CO and formate are also formed. This can be explained by a stronger binding energy between CO and Cu: At a higher overpotential, the negative surface charge of the Cu electrode is larger and thus a stronger π-back donation from the Cu electrode to the adsorbed CO is possible.[23,24] At even higher overpotentials ($E <$ -1.05 V *vs.* RHE), H_2 and methane are the dominant products. The concept of "limiting current density" can be used to explain the increased *FE* of H_2. The limiting current density describes the turning point beyond which an increase in the total current density no longer leads to an increase in the current density for CO_2RR, but to a higher selectivity for the evolution of H_2. This is caused by limitations in the mass transport of CO_2 to the cathode at elevated current densities.[25] At $E <$ -1.05 V *vs.* RHE there is an increased current density, as a higher overpotential is accompanied by an increased negative current density. The increase in the *FE* of methane, on the other hand, can be explained by a decrease in the activation energy for its formation with increasing overpotential.[26]

Table 1: CO_2 reduction reaction (CO_2RR) products on Cu electrodes with the amount of CO_2 (x), H_2O (k), transferred electrons (z), and OH^- (y) required per molecule of product. In addition, the standard reduction potential E° at pH = 6.8 versus RHE is listed.[22]

CO_2RR products	x	k	z	y	E° vs. RHE [V]
Formate	1	1	2	1	-0.02
Carbon monoxide	1	1	2	2	-0.10
Methanol	1	5	6	6	0.03
Glyoxal	2	4	6	6	-0.16
Methane	1	6	8	8	0.17
Acetate	2	5	8	7	-0.26
Glycolaldehyde	2	6	8	8	-0.03
Ethylene glycol	2	8	10	10	0.20
Acetaldehyde	2	7	10	10	0.05
Ethanol	2	9	12	12	0.09
Ethylene	2	8	12	12	0.08
Hydroxyacetone	3	10	14	14	0.46
Acetone	3	11	16	16	-0.14
Allyl alcohol	3	11	16	16	0.11
Propionaldehyde	3	11	16	16	0.14
1-Propanol	3	13	18	18	0.21

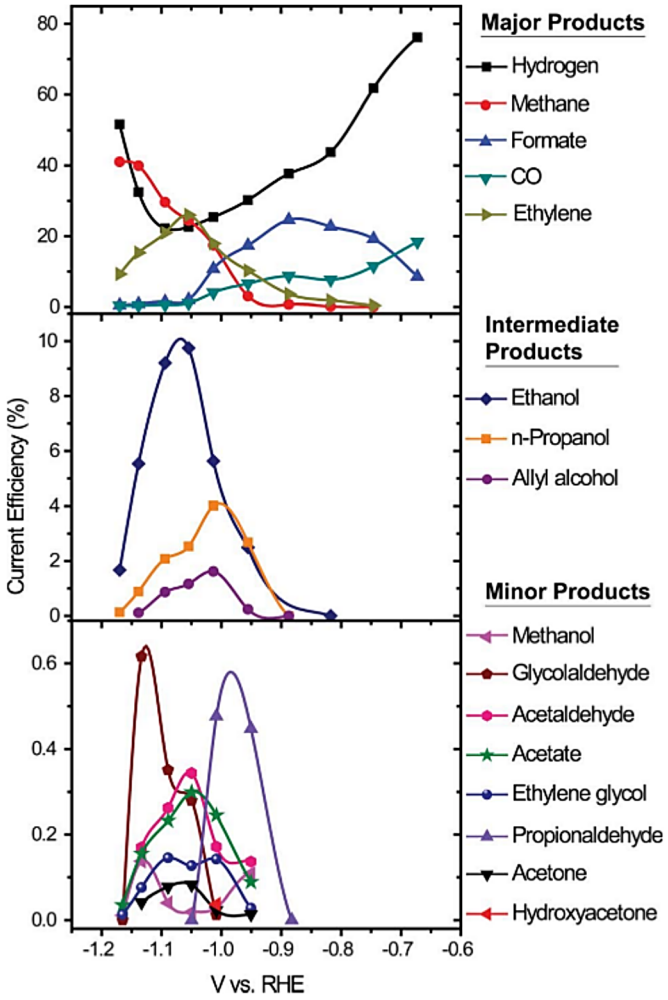

Figure 3: Product formation of the CO_2 reduction reaction (CO_2RR) at a Cu electrode as a function of the applied potential.[22] The products are divided into major, intermediate, and minor products depending on their current efficiency. Clearance was granted via the licence ID 1495778-1.

The reaction mechanisms on Cu electrodes are not yet fully understood. This applies particularly to the products for which more than two electrons are required (see table 1), as several reaction steps with multiple proton and electron transfers are involved, making the reaction complex.[3,19,27] In the literature, several different reaction paths are proposed for specific target molecules. The stated mechanisms deviate significantly from each other, including various intermediates. While some suggested approaches rely on results of theoretical calculations, others are based on experimental observations. Apparently, the reaction mechanisms are not yet clear. The four key steps of one proposed mechanism, which features the formation of ethanol and ethylene on a Cu electrode, are shown below as an example (see figure 4). Here, CO_2 first reacts to *CO with *COOH as intermediate. In this notation, the asterisk denotes an adsorbed molecule. The intermediate is formed either by a proton-coupled

electron transfer or by two successive steps in which first the electron and then the proton transfer takes place. *CO is formed after an additional proton-coupled electron transfer. For the formation of ethylene and ethanol, a subsequent *CO dimerization step is proposed, which is separated into the rate-determining electron transfer and the subsequent proton transfer. After several further proton and electron transfers, the selectivity-determining intermediate is formed, which finally converts either to ethylene or ethanol.[27]

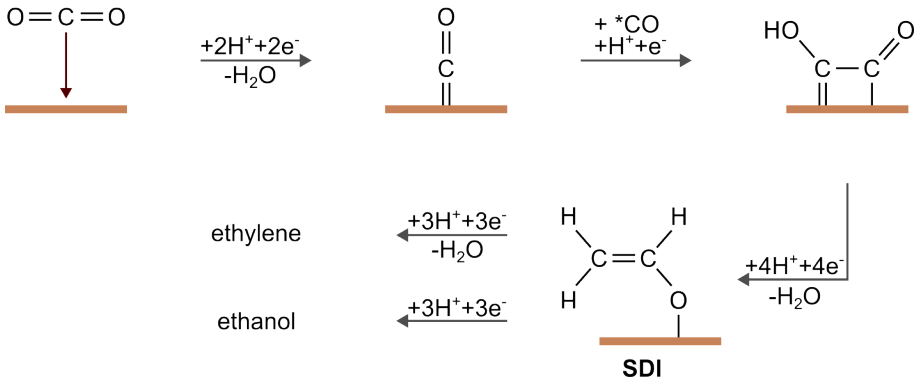

Figure 4: The four key steps of one proposed reaction mechanism for the formation of ethanol and ethylene on Cu electrodes (SDI: selectivity-determining intermediate).[27]

In addition to the unclear reaction mechanism, a major problem with Cu electrodes is their insufficient selectivities for certain C_{2+} products, which leads to more by-products and thus to higher energy-intensive downstream separation processes that decrease the overall energy efficiency. There are several approaches in literature to address the selectivity issue, including alloying[17,28,29], morphology modifications[30,31], defect engineering[32,33], electrolyte engineering[34,35], and electrochemical cell optimization[36,37].

Due to versatile and promising tuning options, the alloying approach is used in this thesis to address the problem of selectivity. For this reason, the approach is described in more detail below. There is consensus in the literature that the key intermediate for all C_{2+} products at a Cu electrode is CO.[22,27,38–40] Therefore, the use of a bimetallic catalyst consisting of Cu and a CO-forming material such as Ag or Au is a promising approach. The CO-forming material should increase the amount of the key intermediate CO for the Cu electrode and thus promotes the formation of C_{2+} products (see equation (5)).[3,29,41] However, it is still difficult to tailor the reaction to a specific product. For instance, ethanol can often not be favored over ethylene (see table 2).[19]

$$CO_2 \xrightarrow{\mathbf{Ag},Cu} CO \xrightarrow{Cu} C_{2+} \tag{5}$$

Table 2: Faradaic efficiencies (*FE*s) of ethanol and ethylene and their ratios for different bimetallic Cu-Ag catalysts from the literature.

conditions	$FE_{ethanol}$ [%]	$FE_{ethylene}$ [%]	$FE_{ethanol}/FE_{ethylene}$	reference
0.1 M $KHCO_3$ -1.1 V vs RHE	17	15	1.1	[42]
1 M $KHCO_3$ -300 mA cm^{-2}	14	25	0.6[1]	[43]
0.1 M $KHCO_3$ -1.1 V vs RHE	<5	37	0.1	[44]
1 M KOH -800 mA cm^{-2}	40	35	1.1	[45]
1 M KOH -0.71 V vs RHE	20	34	0.6	[46]
0.1 M K_2CO_3 -1.2 V vs RHE	34	10	3.4	[47]

[1] Measurement with highest ethanol formation was taken.

However, according to calculations, a new reaction path becomes availabe with abundant *CO.[42] Here, instead of *CO dimerization, *CO reacts with $*CH_x$ (x = 1, 2) to the intermediate $*CH_xCO$ (x = 1, 2) that selectively reacts to form ethanol instead of ethylene (see figure 5).

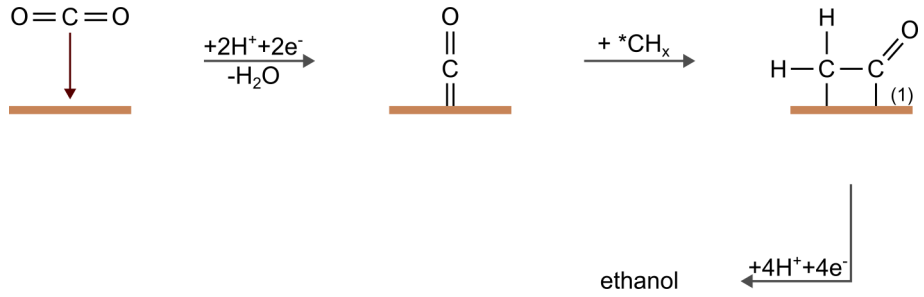

Figure 5: The three key steps of the CO_2 reduction reaction to ethanol in abundance of *CO (1: shown for x = 2).[42]

To validate the calculations, CO_2RR experiments were performed with pure oxide-derived Cu nanowires and with oxide-derived Cu nanowires mixed with 20 nm Ag

particles at a ratio of 1:20.[42] The bimetallic mixture increases the *FE* of ethanol from 7.3 % to 16.5 % and decreases the *FE* of ethylene from 20.1 % to 14.9 % as compared to pure Cu nanowires. However, the ratio of the *FE*s of ethanol and ethylene is still only 1.1. The question therefore remains whether this calculated hypothesis can also be proven with experiments in which a higher ratio of the *FE*s of ethanol and ethylene is achieved.

2.2 Ethanol as Target Product

In this thesis, special attention is drawn to the formation of ethanol via CO_2 electrolysis (Power-to-ethanol) for two good reasons: First, it can help to enable the near-term feasibility of the CO_2RR; and second, it can enhance production of green ethanol on a larger scale.

For a better understanding, a closer look is taken at a possible business case for the CO_2RR (see figure 6). If a new technology is found, in this case the CO_2RR, the initial costs are substantial due to lacking optimization of technology and so-called first-of-a-kind plants. Nevertheless, in order to achieve a near-term feasibility of new technologies, high-value products are essential to overcome the initial high costs.[48] Ethanol fulfills this requirement, e.g. as carrier component of high value perfumes. It can therefore enable near-term feasibility of the CO_2RR and can act as a pioneer process, such that it is worth to be investigated.

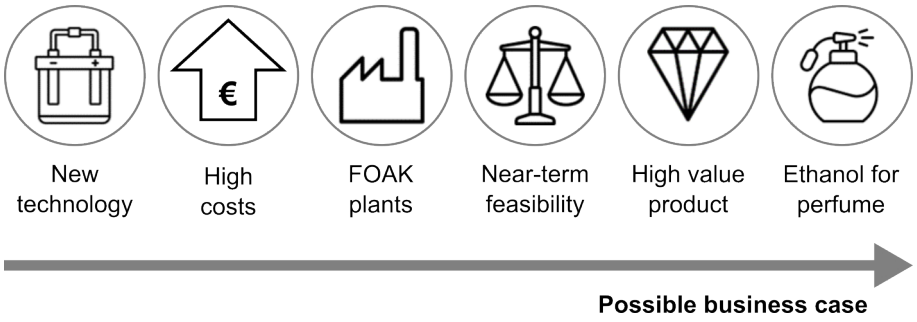

Figure 6: Possible business case for the CO_2 reduction reaction with ethanol as target product (FOAK: first-of-a-kind).

In addition, CO_2RR can also solve a problem in ethanol production. Today, ethanol is mainly produced by fermenting biomass, e.g. sugarcane, which is a green synthesis route using biomass as renewable carbon source.[19,49] In the future, however, green ethanol will be needed in larger quantities, for example, to compensate for the loss of fossil fuels. On the other hand, the use of biomass on larger scales would pose problems in terms of biodiversity and food security.[19] In Brazil alone, it is assumed that between 2012 and 2030, around 35,000 km^2 of cropland, natural grassland, and shrubland will be reallocated to sugar cane cultivation.[50] Therefore, an additional

green production process for ethanol is required, a challenge which the CO_2RR can deal with.

Ethanol in general has a wide range of applications, making ethanol an interesting intermediate product. For example, it can be used in the production of food and pharmaceuticals, as coolant and solvent, as raw material for organic synthesis and as an energy source.[51]

2.3 Cell Concepts for the CO_2 Reduction Reaction

For the CO_2RR, three general types of cathode architectures can be found in the literature, namely planar electrodes (e.g. metal foil or glassy carbon) and porous electrodes (e.g. carbon paper or mesh), which are used in H-type electrolyzers, as well as gas diffusion electrodes (GDEs), which can be used in either liquid- or gas-phase electrolyzers.[52] In the following section, the main focus is drawn to the H-type and the liquid-phase electrolyzer, as they are used in this thesis.

2.3.1 H-Type Electrolyzer

The H-type electrolyzer gets its name from its shape, which is reminiscent of the letter H (see figure 7). There are two compartments, one for the working electrode (WE) and one for the counter electrode (CE). As already mentioned, the WE can be planar or porous, and the well-known OER often is used as the oxidation reaction at the CE (see section 2.1 and equation (3)) to complete the overall reaction. In addition, a reference electrode (RE) can be introduced into the WE compartment with a Haber-Luggin capillary to control or measure the potential at the WE. The two compartments can be separated by an ion-exchange membrane, which allows different types of electrolytes to be used in the two chambers and prevents product crossover to the other electrode side. The catholyte (= electrolyte in the cathode compartment) is pre-saturated with CO_2 and during the reaction, CO_2 is continuously bubbled into the catholyte through a glass frit, which is why these electrolyzers are sometimes also referred to as aqueous-fed electrolyzers.[52,53] In H-type electrolyzers only neutral or acidic catholytes can be used, as the CO_2 bubbled into the catholyte would form carbonate with an alkaline catholyte.[16]

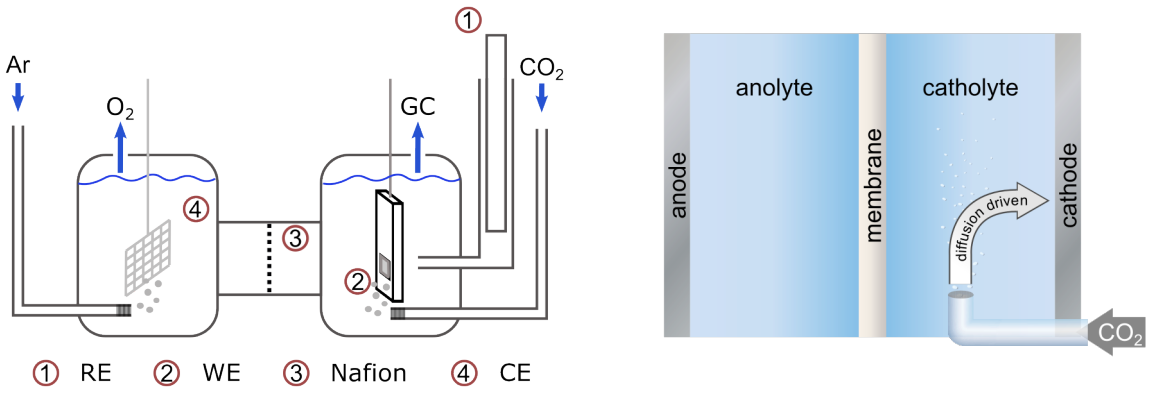

(a) **(b)**

Figure 7: Schematic illustration of an H-type electrolyzer for the electrochemical reduction of CO_2: (a) based on the real shape of the cell (RE: reference electrode, WE: working electrode, CE: counter electrode; note: For simplicity, the RE is drawn on the backside of the cathode; in reality, the RE points to the front side of the WE.)[54] and (b) more schematic and thus easier to compare with the other cell schemes shown below.[12] Note: For figure (b), graphical support was provided by Sebastian Lehmann.

H-type electrolyzers are often used for catalyst screening because they are simple in setup, the stability of the system is only limited by the stability of the catalyst, they can be adapted to various electrodes, and they allow fast and cost-effective studies.[36,52,53] In H-type electrolyzers, however, the CO_2 must first be dissolved in the catholyte before it diffuses to the WE. This limits the performance of the reaction due to the low solubility of CO_2 in water (~ 33 mM at 1 atm and 25 °C)[29,53], the slow mass transport, and the long diffusion pathways for CO_2.[36,52] Therefore, H-type electrolyzers can only be used with maximum current densities of -100 mA cm^{-2}, which is below industrially relevant current densities (minimum -200 mA cm^{-2})[19].[36,37,52] Depending on the specific setup of the H-type electrolyzer, the maximum current density can even be lower than -100 mA cm^{-2}. Moreover, this system is not scalable, so it is only suitable for lab-scale applications.[36]

To overcome these issues, cell concepts with a GDE such as the liquid-phase electrolyzer are required, which is described below.

2.3.2 Liquid-Phase Electrolyzer

Liquid-phase electrolyzers consist of three compartments, designated to the CO_2 gas, the catholyte, and the anolyte, respectively (see figure 8). The GDE with the catalyst layer facing the catholyte is located between the gas and the catholyte chamber. Through the gas diffusion layer (GDL) of the GDE, CO_2 gas can penetrate into the electrode and thus into the catalyst layer, where it reacts. As a result, CO_2 does

not have to diffuse through the aqueous bulk electrolyte, which shortens the diffusion paths such that mass transport limitations are overcome and the reaction is accelerated. Current densities of more than -1 A cm^{-2} are therefore possible. Due to the direct supply of CO_2 to the catalyst layer, these electrolyzers are sometimes also called gas-fed electrolyzer.[53] More information on the structure and manufacturing of GDEs can be found in section 2.3.3. Furthermore, the catholyte and anolyte compartments are separated by an ion-exchange membrane, which has the same functions as in the H-type electrolyzer. Which type of ion-exchange membrane should be used depends on the products formed. For example, if a negatively charged product is formed (e.g. formate), a cation exchange membrane (CEM) should be used to prevent product crossover into the anolyte chamber. In addition, the pH value of the electrolytes should also be taken into account when selecting the membrane. It is also possible to pump the catholyte and/or the anolyte within a liquid-phase electrolyzer, which is then referred to as flow cell.[36] Apparent improvements of pumping are increased mass transfer and enhanced mixing of the electrolyte as well as better heat management.[53]

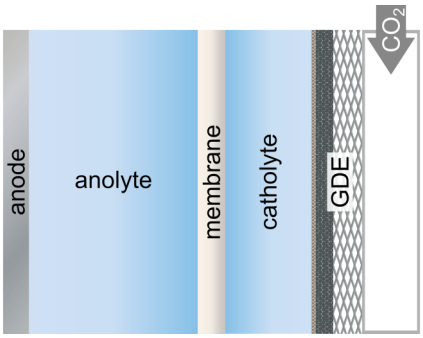

Figure 8: Schematic illustration of a liquid-phase electrolyzer (GDE: gas diffusion electrode).[12] Note: Graphical support was provided by Sebastian Lehmann.

Liquid-phase electrolyzers can be operated in two ways with regard to the gas supply to the catalyst layer, namely in flow-through and flow-by mode. They can be distinguished by the differential pressure Δp between the liquid phase (catholyte) and the gas phase (CO_2). At a sufficiently high gas phase pressure (compared to the liquid phase pressure), Δp is smaller than the capillary forces of the GDE. Given this situation, CO_2 gas penetrates into the catholyte and causing gas bubbles, which is why it is referred to as "bubble point". If this is the case, the mode is called flow-through. If, on the other hand, the pressures on the liquid side and gas side are balanced, there is no breakthrough of CO_2 and the flow-by mode is applied.[53,55,56] Operating in flow-through mode can cause several problems: Firstly, the CO_2 gas bubbles formed increase the Ohmic resistance in the catholyte and thus minimize the energy efficiency of the cell. Secondly, the bubbles can lead to mechanical degradation of the catalyst layer. Moreover, the bubbling of CO_2 into the catholyte can cause a higher carbonation of the catholyte, which changes its pH value and thus the reaction environment. In addition, the GDE can dry and salt crystal can form, blocking the pores for the

CO_2 transport. In contrast, in flow-by mode, small droplets of catholyte are formed on the gas side of the GDE, which is referred to as "perspiration". This prevents salt formation and thus the blocking of the GDE by salt crystals. However, catholyte penetrating into the GDE can also block CO_2 channels.[53]

In the next paragraph, the stability of the electrolyte composition is discussed. In particular, the influence of catholyte and anolyte in presence of a CEM is featured. A typical electrolyte for CO_2RR is potassium bicarbonate ($KHCO_3$),[42–44] thus it appears to be a viable first choice to use $KHCO_3$ as both catholyte and anolyte. However, this would lead to instability of the electrolyte at high currents and/or long experiment times.[57] The instability that occurs can be explained by figure 9a: (1) When a current or potential is applied to the cell, K^+ ions move from the anolyte through the CEM into the catholyte, which is caused by the electric field. (2) Simultaneously, water is oxidized to H^+ ions and oxygen (O_2) at the anode (OER). The H^+ ions formed compensate for the transfer of K^+ ions into the catholyte by maintaining charge neutrality in the anolyte. At the cathode, CO_2 and water react, for instance to CO and OH^-. (3) Subsequently, the H^+ ions can react with the bicarbonate ions in the anolyte to gaseous CO_2 and water and the OH^- combines with CO_2 to bicarbonate in the catholyte. As a result, the concentration of $KHCO_3$ in the anolyte decreases while it increases in the catholyte. The cation crossover thus causes an instability of the electrolyte. As the amount of K^+ ions that pass from the anolyte to the catholyte is proportional to the applied current and the duration of the experiment, its effect on the electrolyte stability only becomes apparent if the current is sufficiently high and/or the experiment lasts long enough. This is not the case in H-type electrolyzers, so that $KHCO_3$ can be used both as catholyte and anolyte. In a liquid-phase electrolyzer assembled with a CEM, however, a different anolyte must be chosen at higher currents.

To counteract the instability of the electrolyte, sulfuric acid (H_2SO_4) can be used as anolyte instead of $KHCO_3$ (see figure 9b): (1) In this case, H^+ ions cross over from the anolyte to the catholyte instead of K^+ ions. (2) The transferred H^+ ions are then replaced by other H^+ ions, which are formed in the OER at the anode. (3) The OH^- formed at the cathode reacts with CO_2 to HCO_3^-, which in turn reacts with the transferred H^+ in the bulk electrolyte to water and CO_2. This allows the concentrations in the catholyte and anolyte to be kept stable.[57]

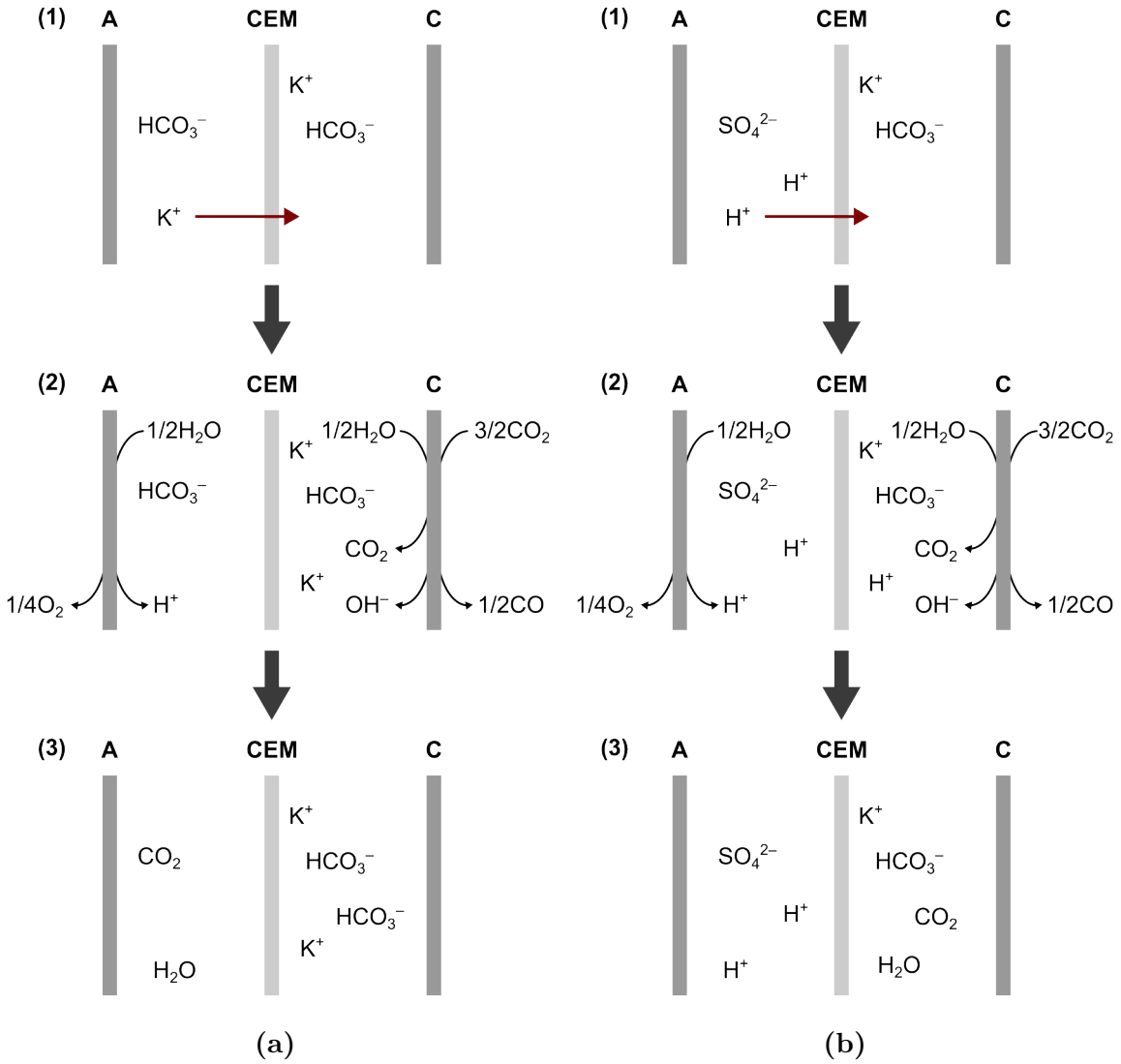

Figure 9: Sketches of influence of the cation crossover in an electrolyzer using a cation exchange membrane: (a) $KHCO_3$ is used as catholyte and anolyte, (b) $KHCO_3$ is used as catholyte and H_2SO_4 as anolyte (C: cathode, CEM: cation exchange membrane, A: anode). Graphic inspired by [57].

Finally, the drawbacks of liquid-phase electrolyzers are addressed and the gas-phase electrolyzer is briefly discussed as a further cell concept. The main difficulties in setting up a liquid-phase electrolyzer are flooding of the GDE, high Ohmic losses due to catholyte resistance, and dilution of any liquid products formed in the catholyte. If one of the liquid products is the target molecule, an energy-intensive downstream separation process is required, which makes the process impractical.[58] An alternative setup is the gas-phase electrolyzer, also known as membrane electrode assembly (MEA) (see figure 10). Here, the cathode and membrane are arranged in a zero-gap configuration in which the catalyst is in direct contact with the membrane. Thus, there is

no catholyte that floods the GDE, increases the Ohmic resistance of the cell, or can dilute liquid products.[36,53,59] However, crossover issues have been reported in this setup, where, for instance, ethanol penetrates the membrane by convection and diffusion and enters the anolyte.[58] In the anolyte, the ethanol is wasted due to dilution and possible oxidation at the anode. In addition, there are problems such as drying of the membrane, a possible increased evolution of H_2 due to acidification when using a CEM, and the fact that a RE cannot be easily included in the setup, which makes it difficult to consider the cathodic and anodic reaction separately.[36,53]

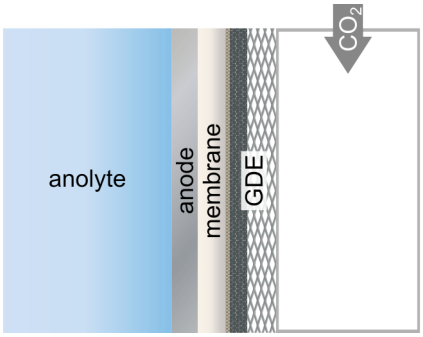

Figure 10: Schematic illustration of a gas-phase electrolyzer (GDE: gas diffusion electrode).[12] Note: Graphical support was provided by Sebastian Lehmann.

2.3.3 Structure and Manufacturing Techniques of Gas Diffusion Electrodes

A GDE contains a GDL and a catalyst layer. The GDL has three functions: Firstly, it enables the transport of CO_2 to the catalyst layer, secondly, it provides physical support for the catalyst layer, and thirdly, it serves as a current collector.[53,60] GDLs are generally hydrophobic to prevent flooding of the GDE, which would block the pathways for the CO_2 to the catalyst layer. A distinction can be made between single-layer and dual-layer GDLs. The single-layer GDL consists of only one macroporous layer (e.g. carbon paper, carbon cloth, carbon felt, carbon foam) with a thickness of 100 - 500 μm.[53] Carbon is chosen as material since it has high stability in an acidic environment, high gas permeability, good electronic conductivity, elasticity under compression, and tunable porosity.[53,61] Additionally, the surface of the macroporous layer can be treated hydrophobically to regulate the wettability.[53] The dual-layer GDL, on the other hand, includes an additional microporous layer (MPL) made of carbon black powder and a hydrophobic agent (e.g. polytetrafluoroethylene (PTFE)) with a thickness of 10 - 100 μm. This enhances the electrical conductivity of the GDL and improves the water management. Moreover, the surface of the GDL is smoothed by the MPL, which is beneficial for subsequent catalyst coating.[53]

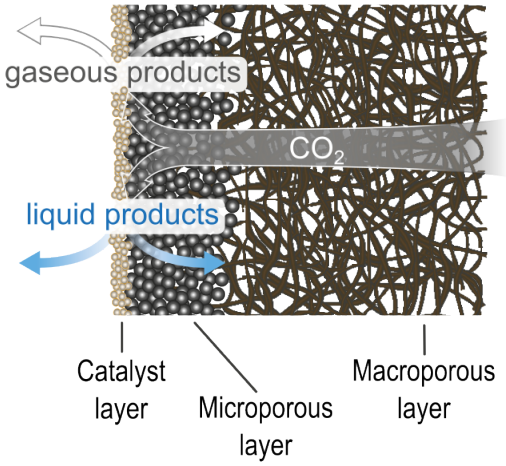

Figure 11: Schematic illustration of a gas diffusion electrode, consisting of a catalyst layer applied on a dual-layer gas diffusion layer with a macro- and microporous layer. The diffusion pathways for the reactant CO_2 and the products are are also shown.[12] Note: Graphical support was provided by Sebastian Lehmann.

As already mentioned, a GDE also contains a catalyst layer in addition to the GDL. Two general techniques can be distinguished for the deposition of the catalyst layer on the GDL, namely the ink-based and ink-free method. The ink-based method starts off with preparation of the respective ink. It consists of the catalyst powder, a solvent (e.g. water, ethanol, isopropyl alcohol), a non-volatile ionic binder as a conductive scaffold (e.g. Nafion, Piperion), and, if desired, carbon black or carbon nanotubes for improved electrical conductivity. The catalyst loading, the binder loading, the choice of the solvent, the evaporation rate of the solvent, and the ink deposition method are parameters that influence the appearance and properties of the catalyst layer. Typical ink deposition methods are drop-casting, hand-painting, and air-brushing.[62] In all techniques, the ink must first be homogenized, which can be done in an ultra sonic bath, for instance. In the drop-casting method, the homogenized ink is casted drop by drop onto the GDL using a pipette. With hand-painting, on the other hand, the ink is applied to the GDL with a paint brush. To ensure a homogeneous catalyst layer, the painting direction is often changed. In the air-brushing method, the ink is sprayed onto the GDL from a certain distance using an airbrush gun. Here, the speed of spraying should be constant in order to obtain a homogeneous catalyst layer.[63]

In contrast, the ink-free methods do not require an ionic binder and the catalyst can be applied directly onto the GDL, for example, by electrodeposition, sputter pulsed laser deposition, and ion-beam deposition.[62] Since the ink-free method is not used in this thesis, its various techniques are not explained in detail here.

2.4 Electrochemical Basics and Formulas

This section first explains the voltage drop (IR drop) in a three-electrode setup, then presents the four key parameters for evaluating the performance of a CO_2RR experiment, and finally gives conversion formulas between different reference systems.

To explain the IR drop in a three-electrode setup, it is first necessary to know what type of electrode the third electrode is and what properties it needs. The third electrode is a RE, which measures the potential of the WE. For the RE, it is required that its electrochemical potential is known and that no current flows through the RE, so that the potential is independent of the current applied in the cell. However, the potential E_p of the WE measured with the RE is distorted by the IR drop between RE and WE, which is caused by the resistance of the electrolyte between these two electrodes. In order to determine the correct potential of the WE, the voltage drop must therefore be measured. To do this, the resistance R_I between WE and RE has to be detected, for example by electrochemical impedance spectroscopy, and then multiplied by the applied current I.[64] The IR-corrected potential E_{IR} can then be calculated according to equation (6).[65]

$$E_{IR} = E_p - I \cdot R_I \tag{6}$$

In addition to subtracting the IR drop, its value can also be minimized by decreasing the distance between WE and RE as well as by enhancing the conductivity of the electrolyte.

Next, the four key parameters for evaluating the performance of a CO_2RR experiment are introduced, namely activity, efficiency, selectivity, and stability.[53,66–70] The activity can be measured by the current density j, which is calculated by dividing the current I by the area A of the WE. A distinction can be made between the geometric A_{geo} and the electrochemically active surface area A_{ECSA} of the WE (see equation (7)).

$$j_{geo} = \frac{I}{A_{geo}} \quad \text{or} \quad j_{ECSA} = \frac{I}{A_{ECSA}} \tag{7}$$

The efficiency, on the other hand, can be described by the overpotential η, which is the potential difference between the applied potential E and the thermodynamically necessary potential E_{TD} (see equation (8)) at a given current density.[71] The smaller this difference, the better is the efficiency of the experiment. As the efficiency (or overpotential) is related to the activity (or current density), both have to be considered together.

$$\eta_i = E - E_{TD,i} \tag{8}$$

Furthermore, the selectivity can be determined using the *FE*, which describes the percentage of charge that is used for a desired product i.[72] For this purpose, the charge Q_i is calculated taking into account the number of moles formed n_i, the number of electrons exchanged z_i (see table 1), and the Faraday constant F (see equation (9)).[17,73]

$$FE_i = \frac{Q_i}{Q} = \frac{n_i \cdot z_i \cdot \mathrm{F}}{Q} \tag{9}$$

For dynamic reactions, n_i can be replaced by the formation rate, $\dot{n}_i$, and Q by the current I (see equation (10)).

$$FE_i = \frac{\dot{n}_i \cdot z_i \cdot \mathrm{F}}{I} \tag{10}$$

To do this, $\dot{n}_i$ can be calculated using the volume flow $\dot{V}$ at the gas outlet, the volume fraction ϕ_i, and the molar gas volume V_m (see equation (11)).[74]

$$\dot{n}_i = \frac{\dot{V} \cdot \phi_i}{V_\mathrm{m}} \tag{11}$$

In addition, the stability of a CO_2RR experiment can be described by the duration of the experiment. More than 1000 operating hours are required for industrial use.[19]

Finally, formulas for converting potentials into different reference systems are given. If the potential measured versus any RE is to be converted into the standard hydrogen electrode (SHE) system, this is done by considering the standard electrode potential E° of the used RE according to equation (12).[75]

$$E(\text{vs. SHE}) = E(\text{vs. RE}) + E^\circ(\text{RE}) \tag{12}$$

For the conversion between the SHE and the RHE, the pH value of the electrolyte is required (see equation (13)).[76]

$$E(\text{vs. RHE}) = E(\text{vs. SHE}) + 0.0591\,\mathrm{V} \cdot \mathrm{pH(electrolyte)} \tag{13}$$

Combining equation (12) and (13), the direct conversion of any RE system into the RHE system is possible (see equation (14)).

$$E(\text{vs. RHE}) = E(\text{vs. RE}) + E^\circ(\text{RE}) + 0.0591\,\mathrm{V} \cdot \mathrm{pH(electrolyte)} \tag{14}$$

Since in all experiments in this thesis a Ag/AgCl electrode filled with a saturated KCl solution is used as RE and the data are mainly presented versus the RHE, the explicit conversion formula for these two reference systems is given in equation (15).

$$E(\text{vs. RHE}) = E(\text{vs. Ag/AgCl (sat.)}) + 0.197\,\mathrm{V} + 0.0591\,\mathrm{V} \cdot \mathrm{pH(electrolyte)} \tag{15}$$

3 Experimental

In this chapter, the used chemicals are listed first (see section 3.1), followed by a description of the experimental procedure in the H-type electrolyzer (see section 3.2) and the liquid-phase electrolyzer (see section 3.3). The respective experimental procedure includes the specific catalyst synthesis, the electrode preparation, and the conduction of the CO_2RR.

3.1 Chemicals

The used chemicals were supplied by the Institute of Energy and Climate Research, Fundamental Electrochemistry (IEK-9), now renamed the Institute of Energy Technologies, Fundamental Electrochemistry (IET-1), located at Forschungszentrum Jülich. The supplier and purity of the chemicals are listed in table 3.

Table 3: List of supplier and purity of the used chemicals (ACS: Fulfills the requirements for an analytical chemical as defined by the American Chemical Society, BP and USP: Fulfills the purity requirements of the British and United States Pharmacopoeia, respectively; MEK: methyl ethyl ketone.)

Chemical compound	Supplier	Purity
1-propanol	Merck	99 %
2,2'-bipyridine	Merck	ACS
Acetonitrile	Sigma-Aldrich	≥ 99.9 %
Ammonia (28.0 - 30.0 %)	Sigma-Aldrich	ACS
Copper nanopowder (20 - 50 nm)	thermo scientific	99.9 %
Copper nanopowder (40 - 60 nm)	Sigma-Aldrich	≥ 95 %
Copper nanopowder (60 - 80 nm)	Sigma-Aldrich	≥ 95 %
Copper(II) sulphate pentahydrate	VWR	≥ 99 %
Dimethyl sulfoxide	Sigma-Aldrich	≥ 99.9 %
Ethylenediaminetetraacetic acid	Sigma-Aldrich	99.4 - 100.6 %
Ethanol	Chemsolute	≥ 99.5 %
Ethanol (technical)	Fa. Hofmann	96 % + MEK

Formaldehyde (37 %)	Merck	BP, USP
Heptafluorobutyric acid	Thermo scientific	99 %
Hydrochlorid acid (37 %)	Merck	≥ 99 %
Hydrogen peroxide (30 %)	Merck	Suprapur
Iron(III) nitrate nonahydrate	Merck	≥ 99 %
Isopropanol (technical)	Bernd Kraft	≥ 98 %
Lithium hydroxide solution	Alfa Aesar	≥ 98 %
Nafion (20 w%)	Ion Power	
Nitric acid (65 %)	Merck	Emplura
Piperion (5 w%)	Versogen	
Potassium bicarbonate	Honeywell	≥ 99.7 %
Potassium sodium tartrate tetrahydrate	Chemsolute	99.5 %
Silver nitrate	Alfa Aesar	99.9995 %
Sodium hydroxide	Sigma-Aldrich	≥ 98 %
Tin(II) chloride hydrate	Alfa Aesar	99.995 %

3.2 H-Type Electrolyzer

3.2.1 Catalyst Synthesis

The basic synthesis of copper-silver nanoplates (CuAg NPls) for the H-type electrolyzer has already been developed in the master thesis "Preparation and Characterization of Modified Metal Surfaces as a Catalyst for the Electrochemical Reduction of Carbon Dioxide" by Elisabeth Robens 2020 at IEK-9 (now renamed IET-1). Nevertheless, for the sake of completeness, the synthesis route used for this PhD project is described below. Part of the description is based on the publication "Bimetallic Copper-Silver Catalyst for the Electrochemical Reduction of CO_2 to Ethanol" published by Elisabeth Robens *et al.* 2023 in ACS Applied Energy Materials.[54]

Table 4: Composition of the different synthesis solutions (S1: seeding solution 1, S2: seeding solution 2, P1: plating solution 1, P2: plating solution 2, and EDTA: ethylenediaminetetraacetic acid).

Name	Substances	Concentration [mmol L^{-1}]	Solvent
S1	Tin(II) chloride	20	water-ethanol (1:1)
	Hydrochloric acid	55	
S2	Silver nitrate	20	water
	Ammonia	80	
P1	Potassium sodium tartrate	240	water
	Iron(III) nitrate	25	
P2	Silver nitrate	40	water
	Nitric acid	12	
	Ammonia	200	
Cu bath	Formaldehyde	100	water
	Copper sulfate pentahydrate	50	
	EDTA	100	
	2,2'-bipyridine	0.032	

The synthesis of CuAg NPls comprises the preparation of silver nanoplates (Ag NPls) as a basic structure and the subsequent electroless Cu deposition on top of them (see figure 12). The Ag NPls themselves are synthesized in two steps: first a seeding and then an electroless Ag plating is performed.[77–79] As a pre-treatment, Ag foil (15 mm × 10 mm) was first cleaned with a polishing paper (P4000, Struers), then with ethanol and water. Finally, a solution of hydrogen peroxide and ammonia (ratio 1:2 and diluted with water in a ratio of 3:7) was applied for ten seconds to reduce the silver oxide at the surface. Two seeding solutions (S1 and S2) and two plating solutions (P1 and P2) were thereafter prepared according to table 4. The Ag foil was immersed in 10 mL of S1 for one minute and then cleaned five times with a water-ethanol solution (ratio 1:1). This was repeated with 10 mL of S2, using only pure water for the cleaning step. Subsequently, the electroless plating of Ag was performed. This was done by pouring 5 mL of P1 and 5 mL of P2 together onto the pre-seeded Ag foil in a 30 mL glass vial, sealing it, and placing it in an oven at 70 °C for one hour. To complete, the Ag foil with the Ag catalyst layer grown on it was cleaned with water.

For the electroless Cu deposition, an aqueous Cu bath consisting of formaldehyde, copper sulfate pentahydrate, ethylenediaminetetraacetic acid (EDTA), and 2,2‘-bipyridine

was used (see table 4).[80,81] The pH value of the solution was adjusted between 11.5 and 13.5 by adding sodium hydroxide platelets and the bath was purged with nitrogen for 15 minutes. Afterward, the Ag foil with the previously synthesized Ag structure on top was inserted into 25 mL of the Cu bath. In contact with the Ag NPls, the Cu ions were reduced by formaldehyde in an alkaline solution. The Ag NPls acted as a catalyst for the reaction. Therefore, the reduction of Cu occurs only on the surface of the Ag NPls and not in solution.[80,81] Thus, the separation of the solution after the reaction was simple since no elemental Cu remained in the solution. The amount of Cu on the surface of the Ag NPls was controlled by the duration of the electroless Cu deposition. The duration was varied between 1 second and 15 minutes.

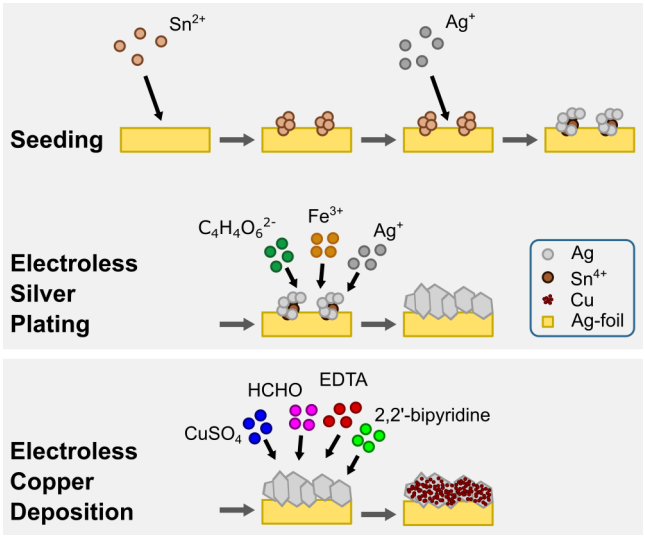

Figure 12: Scheme of the synthesis of copper-silver nanoplates used in the H-type electrolyzer: first, silver nanoplates are formed in a two-step synthesis followed by electroless copper deposition.[54]

3.2.2 Electrode Preparation

For the CuAg NPls, no further electrode preparation is required for H-type electrolyzer applications, as the catalyst grows on Ag foil and thus not only the catalyst but also the entire electrode is produced during the catalyst synthesis.

In addition to the CuAg NPls, commercial copper nanoparticles (Cu NPs) with two ranges of diameter (40 - 60 nm and 60 - 80 nm) were also used as electrocatalysts in the H-type electrolyzer. The manufacturing of electrodes with these Cu NPs is based on the work of Christina Martens. To form an electrode, the Cu NPs were sprayed onto glassy carbon. For this, two pieces of glassy carbon (1 cm × 1 cm) were first cleaned with isopropanol and then mechanically with a fine laboratory paper. Afterward, the pieces were attached to a glass plate with Kapton tape in a marked area of 4 cm × 5 cm (see figure 13). An ink was prepared containing Cu NPs (catalyst loading: 2 mg cm^{-2}

or 0.7 mg cm^{-2}), Nafion as binder (m(Nafion)/m(catalyst) = 7.5 %), and 2.5 mL of 1-propanol as solvent. The ink was homogenized in an ultrasonic bath (Elmasonic S, Elma) for 40 minutes. An airbrush gun (HG trigger-type, Tamiya) with 0.75 bar nitrogen was used to spray the ink onto the glass plate from a distance of about 20 cm. During this process, the airbrush gun was moved across the spray area in a serpentine pattern. After each pass, the glass plate was rotated by 90 ° to ensure a homogeneous coating. The electrodes were stored in a glove box until they were used in the CO_2RR. Finally, the airbrush gun was cleaned with ethanol and water and then immersed in a beaker filled with dimethyl sulfoxide. The beaker was placed in an ultrasonic bath for at least one hour.

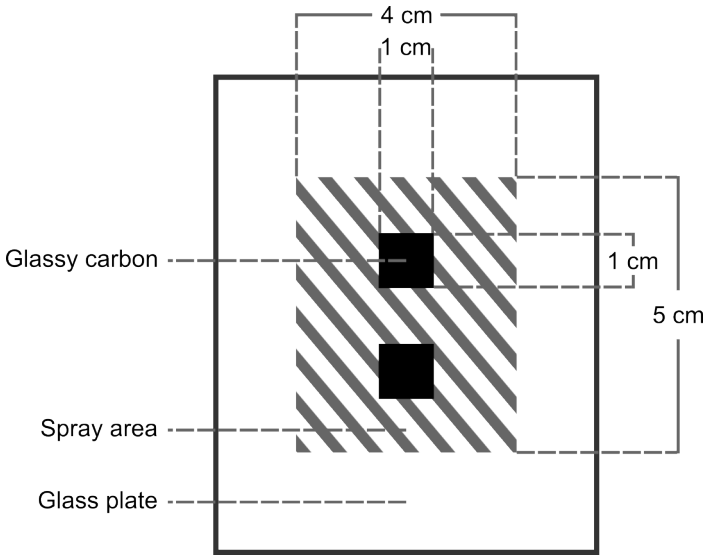

Figure 13: Scheme of the electrode preparation with copper nanoparticles as electrocatalyst and glassy carbon as substrate using spray coating as manufacturing technique.

3.2.3 CO_2 Reduction Reaction

The description of the CO_2RR in the H-type electrolyzer is based on the publication "Bimetallic Copper-Silver Catalyst for the Electrochemical Reduction of CO_2 to Ethanol" published by Elisabeth Robens *et al.* 2023 in ACS Applied Energy Materials.[54]

For the CO_2RR, a custom-made H-type electrolyzer (see figure 14) separated by a Nafion 117 membrane and containing a 0.1 mol L^{-1} $KHCO_3$ electrolyte was used. Additionally, a platinum mesh and a commercial Ag/AgCl electrode (saturated, RE-1CP, ALS) were applied as CE and RE, respectively. The CO_2 gas inlet containing a frit with a pore size of 100 to 160 µm was positioned such that the gas bubbles entered the system on the front side of the working electrode. The cathode compartment was filled with 55 mL and the anode compartment with 60 mL of electrolyte. Prior

to the electrochemical measurements, the cathode and anode compartments were purged with CO_2 (99.995 %) and argon (99.9992 %), respectively, at a flow rate of 10 mL_n min^{-1} for 30 minutes. Argon is used to purge oxygen formed at the anode from the anolyte to prevent diffusion of small amounts of oxygen through the membrane to the cathode and subsequent reduction of oxygen. The cathode was inserted into the system with a custom-made Teflon sample holder that set the geometric surface area of the catalyst to 0.5 cm^2.



Figure 14: Photo of the custom-made H-type electrolyzer, in whose cathode compartment the self-made sample holder and the reference electrode are inserted. Note: The cathode compartment is on the left-hand side, as otherwise it would not be possible to show the reference electrode in the photo.

To prevent the oxidation of the catalyst, a reductive potential of -0.9 V vs. RE was already applied when the catalyst was inserted. For the electrochemical measurements, a VSP-300 potentiostat from Biologic was used. The potentiostat was additionally connected to an internal 30 V booster card when the Cu NPs were used as electrocatalyst. To determine the IR drop between the RE and WE, a potentio electrochemical impedance spectroscopy (PEIS) measurement was conducted. The IR drop-corrected potential versus a RHE is then calculated by combining equation (6) and equation (15):

$$E_{\text{IR-corr.}}(\text{vs. RHE}) = E(\text{vs. Ag/AgCl}) + 0.197\,\text{V} + 0.0591\,\text{V} \cdot \text{pH(electrolyte)} - I \cdot R \tag{16}$$

The pH of the electrolyte saturated with CO_2 was 6.8. After the PEIS measurement, a cyclic voltammetry (CV) measurement with a scanning rate of 20 mV s^{-1} was performed in the potential range of -0.1 V to -0.5 V vs. RHE. The following CO_2RR was

performed by chronopotentiometry (CP) at -20 mA cm^{-2} for 100 minutes or at varying current densities for 55 minutes.

The gaseous products of the CO_2RR were analyzed every 15 minutes during the experiment by gas chromatography (GC) (Trace 1310, Thermo Scientific) with three parallel gas analysis channels. Two channels were each equipped with a 2 m × 1 mm Hayesep Q as pre-column and a 2 m × 1 mm column packed with 5 Å thick molecular sieves as main column as well as a thermal conductivity detector. The first channel quantified atmospheric gases as well as CO using helium as carrier gas, while the other channel analysed H_2 in the presence of argon as carrier gas. The third channel detected hydrocarbon products using two 30 m × 0.32 mm × 5 μm RTX-1 capillary columns as the pre-column and main column, respectively. Moreover, helium was utilized as the carrier gas, and a flame ionization detector was applied. Additionally, liquid samples (5 mL) were taken after 55 and 100 minutes and were examined offline either by ion exclusion chromatography (IEC) (S155 with S5300 sample injector, Sykam) for formate or by headspace gas chromatography (HS-GC) (Trace 1310 with TriPlus 300 Headspace autosampler, Thermo scientific) for the other liquid products. For the IEC, a solution containing 7 vol% acetonitrile and 0.70 mmol L^{-1} heptafluorobutyric acid was used as the eluent and a 2 mmol L^{-1} lithium hydroxide solution as the solution for the suppressor. Furthermore, the chromatograph was equipped with a 300 mm × 8 mm Sykro-Gel-Ex-450 SA-E01 column and a conductivity detector. For the HS-GC, a 30 m × 0.32 mm × 5 μm RTX-1 capillary column with helium as carrier gas and a flame ionization detector was employed. To perform the HS-GC analysis, 2 mL of the sample and 200 µL of a 5 mol L^{-1} potassium hydroxide solution were required. Potassium hydroxide was added to inhibit the release of CO_2 present in the samples due to the experiment, which would lead to an uneven dilution of the gas phase. The IEC and HS-GC results were verified by single ^{1}H-nuclear magnetic resonance (^{1}H-NMR) measurements with a water signal suppressing method (Avance 600 MHz, Bruker).[22]

3.3 Liquid-Phase Electrolyzer

3.3.1 Catalyst Synthesis

In the synthesis of the CuAg NPls for the liquid-phase electrolyzer, Ag NPls are again formed first, followed by the electroless Cu deposition. Here, however, the Ag NPls are grown in a single step in solution and not on the surface of Ag foil (see figure 15). To form the Ag NPls, 100 mL P1 and 100 mL P2 were poured together into a Schottky bottle and placed in an oven at 70 °C for four hours (see table 4). The solution was then filtered (1290, Satorius) and the filter cake was washed with water, yielding the Ag NPls. Subsequently, 25 mL of the Cu bath was added to the Büchner funnel and aspirated after around 1 min. The filter cake was rinsed again with water to finally obtain the CuAg NPls.

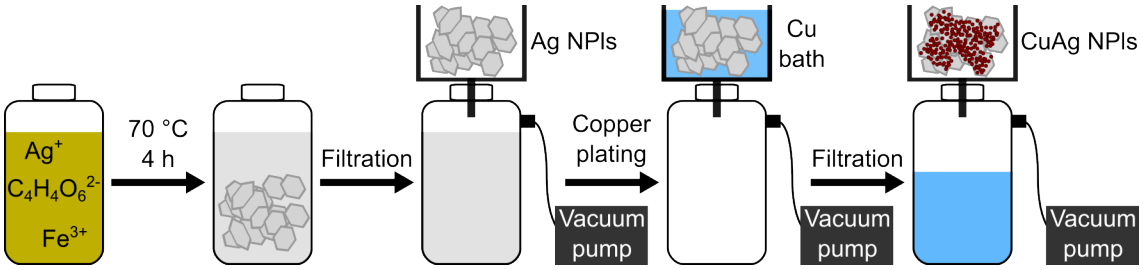

Figure 15: Schematic representation of the different steps for synthesizing the copper-silver nanoplates for the liquid-phase electrolyzer (Ag NPls: silver nanoplates, CuAg NPls: copper-silver nanoplates).

3.3.2 Electrode Preparation

A dual-layer GDL, namely Sigracet 28 BC, was utilized for all GDEs. It has a thickness of 235 μm and consists of a non-woven carbon paper with a microporous layer (MPL) that is 5 w% PTFE-treated.

Drop casting, an ink-based coating process, was applied as the manufacturing technique for the self-produced CuAg NPls (see section 2.3.3). For this, an ink consisting of CuAg NPls as electrocatalyst (catalyst loading = 1.4 mg cm^{-2} or 0.7 mg cm^{-2}), Nafion or Piperion as binder (m(binder)/m(castalyst)= 10%), and 1.35 mL of ethanol as solvent was prepared. For homogenization, the ink was placed in an ultrasonic bath (Elmasonic S, Elma) for 40 minutes. Meanwhile, a 3 cm × 5 cm piece of the GDL was attached to a glass plate with Kapton tape to form an area of 2.5 cm × 2.5 cm for the drop casting (see figure 16). The ink was then dropped onto the GDL in several layers with a glass pipette. After drying, the Kapton tape was removed and the final GDE was obtained. Using the same technique and parameters, also GDEs with the self-synthesized Ag NPls and commercial Cu NPs (20 - 50 nm) in a ratio of three to one were prepared.

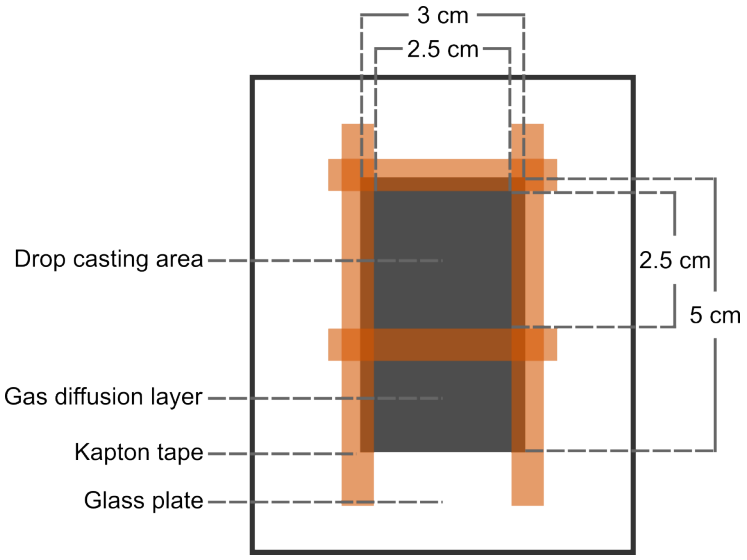

Figure 16: Scheme of the preparation of gas diffusion electrode with copper-silver nanoplates as electrocatalyst using drop casting as manufacturing technique.

As in the H-type electrolyzer, in addition to the CuAg NPls, commercial Cu NPs with two ranges of diameters (40 - 60 nm and 60 - 80 nm) were tested as electrocatalysts. The Cu NPs were again applied by spray coating, but only the ink with the higher catalyst loading (2 mg cm^{-2}) was employed. The spraying process was almost identical to that used for the spray coated electrodes for the H-type electrolyzer (see section 3.2.2). The only difference is that the ink was sprayed onto a 3 cm × 5 cm piece of GDL and not onto glassy carbon (see figure 17).

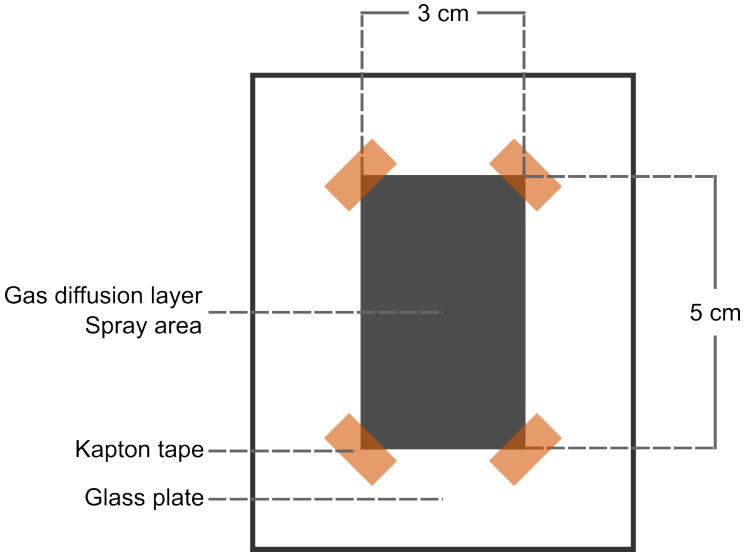

Figure 17: Scheme of the preparation of gas diffusion electrode with copper nanoparticles as electrocatalyst using spray coating as manufacturing technique.

3.3.3 CO_2 Reduction Reaction

As liquid-phase electrolyzer the static FlexCell with an additional anolyte compartment from Gaskatel was utilized (see figure 18). The active area of the WE was 3 cm^2 and the cell was filled with 1 M $KHCO_3$ (9.5 mL) and 1 M H_2SO_4 (30 mL) as catholyte and anolyte, respectively. Nafion 117 was employed as membrane, PtIr as CE, and a saturated Ag/AgCl electrode as RE. CO_2 (99.995 %) as feed gas was supplied to the cell on the gas side of the GDE at a flow rate of 20 $mL_n\,min^{-1}$ or 60 $mL_n\,min^{-1}$. Additionally, the catholyte was purged with a 10 $mL_n\,min^{-1}$ argon (99.9992 %) stream (sweep gas) to enable analysis of the gaseous products formed in the catholyte.

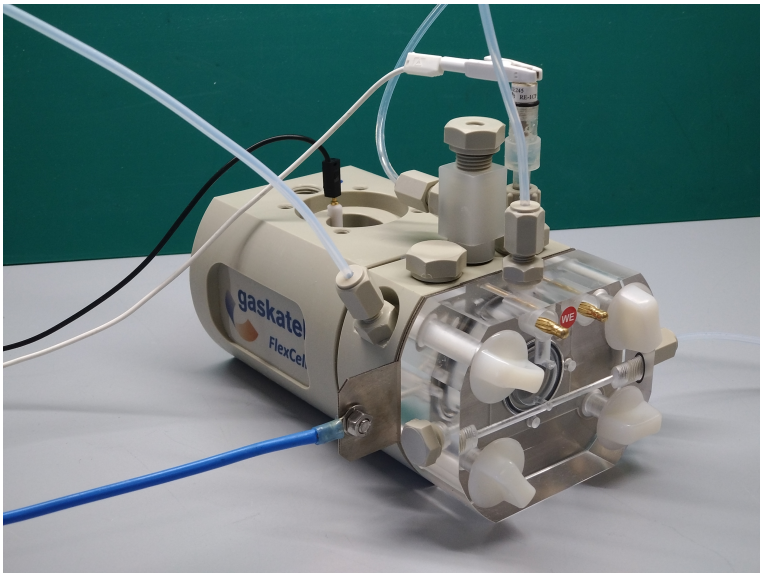

Figure 18: Photo of the static FlexCell from Gaskatel with inserted Ag/AgCl (sat.) reference electrode and a T-piece at the gas outlet of the catholyte compartment for taking liquid samples.

For the electrochemical measurements, a VSP-300 potentiostat from Biologic was again used, which was connected to an internal 30 V booster card. To determine the IR drop between RE and WE, a PEIS measurement was conducted as in the H-type electrolyzer experiments and the IR-corrected potential at the WE versus RHE was calculated using equation (16). The pH of the catholyte is assumed to be 7.8.[82] After the PEIS measurement, a CV measurement was performed with a scanning rate of 20 $mV\,s^{-1}$ in the potential range of -0.1 V to -1.1 V vs. RHE. The following CO_2RR was performed by CP at -100 $mA\,cm^{-2}$ or -300 $mA\,cm^{-2}$ for 100 minutes, unless otherwise stated. For single experiments, subsequently, the CV measurement performed prior to the CO_2RR was repeated.

The gaseous products formed during the CO_2RR were analyzed with the same GC as in the experiments with the H-type electrolyzer. However, the hydrocarbon channel was improved by using a new 30 m × 0.32 mm × 5 μm TG-bond alumina capillary

column and a 30 m × 0.32 mm × 5 μm Stabilwax as pre-column, which allow a shorter injection interval of 10 minutes instead of 15 minutes. In the liquid-phase electrolyzer, gaseous products can form both on the gas side and on the catholyte side, such that two gas streams had to be analyzed. Unfortunately, the GC used could not measure two gas streams simultaneously. By using a stream selector, however, it was possible to detect the gas streams alternately. For this purpose, the two gas streams were connected to a stream selector that can switch back an forth between two valve positions. In the first position, the gas from the gas side is directed to the GC and the gas from the catholyte side to its gas counter, while it is vice versa in the second position (see figure 19). The switching was performed every 10 minutes, thus each gas side was analyzed by the GC every 20 minutes. The first GC injection was conducted after 10 minutes from the gas side. A drum-type gas flow counter (TG05, Ritter) and a MilliGascounter (MGC-1 V3.4 PMMA, Ritter) were used to determine the volume flows at the gas outlets on the gas side and the catholyte side, respectively. The volume flows are required to calculate the Faradaic efficiency (FE) of the gaseous products (see equation (10) and equation (11)). In addition to quantifying the gaseous products, liquid samples (1 mL) were taken from the catholyte with a syringe via a T-piece at the gas outlet of the catholyte compartment (see figure 18), usually in the middle and at the end of the measurement time. After the experiment, the samples were analyzed again by IEC and HS-GC. The same device was used for the IEC as for the experiments in the H-type electrolyzer. In contrast, a new HS-GC device was used for laboratory organizational reasons, namely the TRACE 1610 with a TriPlus RSH SMART autosampler. It was equipped with the same column, the same carrier gas, and the same detector as the device used for the experiments with the H-type electrolyzer. However, due to a similiar but different injector this instrument required 4 mL instead of 2 mL of sample. As only 1 mL samples could be taken, the samples were diluted to 4 mL with a 1 mol L^{-1} $KHCO_3$ solution. Due to the higher catholyte concentration in the liquid-phase electrolyzer (1 mol L^{-1} instead of 0.1 mol L^{-1}), it was also necessary to prepare the calibration solutions with the same $KHCO_3$ matrix as the samples, as a matrix of this concentration has already an influence on the phase equilibrium between liquid and headspace (investigated by Albert Luft).

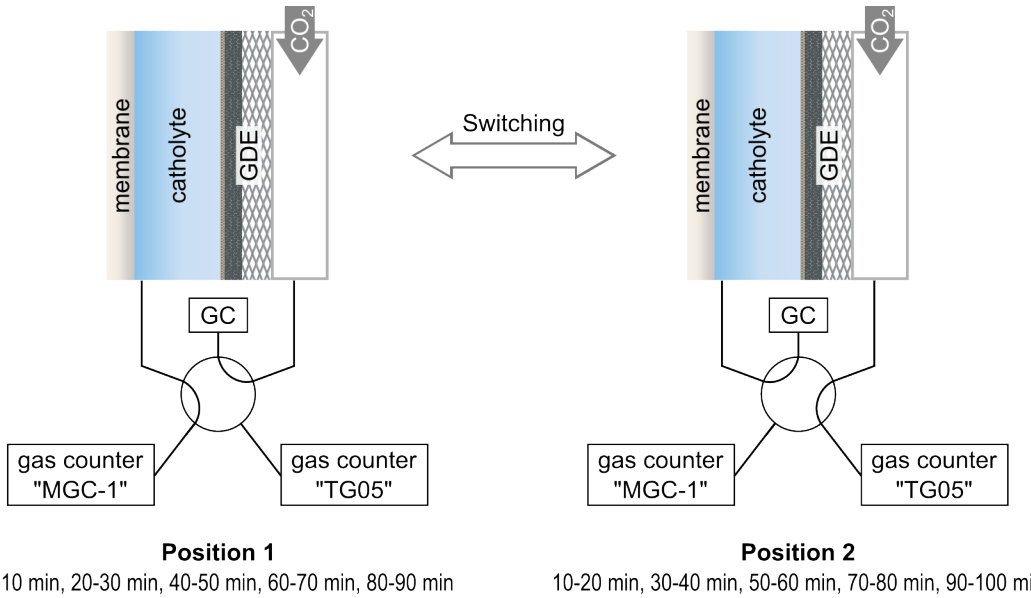

Figure 19: Schematic representation of the two stream selector positions (GC: gas chromatography). Position 1: the gas from the gas side is directed to the GC and the gas from the catholyte side to its gas counter (MGC-1); position 2: the gas from the catholyte side is directed to the GC and the gas from the gas side to its gas counter (TG05).

Two setup modifications have been carried out on the FlexCell, namely the pumping of the catholyte (flow mode) and the control of the gas/catholyte interface (pressure mode). In flow mode, the catholyte was recycled through the catholyte chamber with a peristaltic pump (Masterflex Ismatec) at a flow rate of 5 mL min^{-1}. A water-cooled catholyte reservoir of 100 mL was used. In this mode, the argon sweep gas (10 mL_n) was fed into the catholyte reservoir, and the liquid samples were collected from the reservoir with a syringe *via* a septum. For the pressure mode, a water column was added to the setup between gas side and its gas counter. By immersing the gas tube more or less deeply into the water column, the pressure on the gas side could be adjusted. The pressure on the catholyte side, on the other hand, was constant and was given by the counter pressure of the gas counter "MGC-1", which is around 8.5 mbar versus ambient pressure. A change in pressure on the gas side thus controls the gas/catholyte interface. Two sensors (FDAD3302A, Ahlborn) measured the pressures on the gas and catholyte side.

3.4 Catalyst Characterization

The descriptions of the different characterization methods are based on the publication "Bimetallic Copper-Silver Catalyst for the Electrochemical Reduction of CO_2 to Ethanol" published by Elisabeth Robens *et al.* 2023 in ACS Applied Energy Materials

and is supplemented with additional information.[54]

3.4.1 Scanning Electron Microscopy

Scanning electron microscopy (SEM) images of the catalysts were acquired using a Quanta FEG 650 instrument from FEI (Hillsboro, Oregon, USA). The samples were scanned at a distance of 10 mm with an accelerating voltage of 20 kV, and the secondary electrons were sensed by an Everhart-Thornley detector. For the cross-sectional image of the CuAg NPls grown on Ag foil, the sample was embedded in resin, cut transversely, and polished. To achieve better electrical conductivity, the resin-embedded catalyst was attached to the sample holder with copper tape. To obtain a cross-sectional image of the GDE, the GDE was cut with a scalpel and then attached vertically to the sample holder.

The energy-dispersive X-ray spectroscopy (EDX) measurements were performed using the same instrument as for SEM. For the analysis, an Octane Super detector or an Octane Elite detector from EDAX was applied using an acceleration voltage of 20 kV. The X-ray signals associated with the L-shells for Cu and Ag were used for analysis.

3.4.2 X-Ray Diffraction

The D4 Endeavour instrument from Bruker (Indiana, USA) with a Cu K-alpha source (1.5406 Å) was applied for X-ray diffraction (XRD) analysis on the CuAg NPls grown on Ag foil. Measurements were performed at 40 kV and 40 mA in a Bragg-Brentano-geometry between 10 ° and 130 ° with a step size of 0.01 ° and a counting time per step of 2 s.

For the XRD measurements on the GDE with Ag NPls as catalyst, the Empyrean device from Panalytical (Kassel, Deutschland) was used. The instrument was equipped with a Cu K-alpha source provided with a nickel filter to eliminate Cu K-beta radiation. The measurements were performed at 40 kV and 40 mA in a GI-XRD geometry (incidence angle = 0.5 °) between 15 ° and 90 ° with a step size of 0.04 °, and a counting time per step of 1.76 s. The PIXcel3D was utilized as detector.

3.4.3 Inductively Coupled Plasma Mass Spectrometry

To determine the total amount of Cu in the CuAg NPls grown on Ag foil, 0.5 cm^2 of the catalyst layer was first detached from the Ag foil in an ultrasonic bath. The detached catalyst was then dissolved with concentrated HNO_3. The Ag and Cu content was subsequently determined by inductively coupled plasma mass spectrometry (ICP-MS) (7900 ICP-MS, Agilent).

To investigate the altering of the catalyst, samples of the electrolyte were taken after 100 min of each CO_2RR experiment. The Cu content in the electrolyte was then

analyzed by ICP-MS (7900 ICP-MS, Agilent).

The ICP-MS measurements were conducted by the "Central Institute of Engineering, Electronics and Analytics" (ZEA 3) located at the Forschungszentrum Jülich.

3.4.4 X-Ray Photoelectron Spectroscopy

X-ray photoelectron spectroscopy (XPS) measurements of the CuAg NPls grown on Ag foil were carried out to analyze the near-surface composition. A Phi5000 VersaProbe II instrument (ULVAC-Phi Inc., USA) with a monochromatic Al K-alpha source (1.486 keV) was utilized for the XPS measurements. The analysis was performed in 0.8 eV steps, with each step lasting 100 ms. The Shirley background was used for the analysis.

The XPS measurements were conducted by the "Central Institute of Engineering, Electronics and Analytics" (ZEA 3) located at the Forschungszentrum Jülich.

4 Results and Discussion

As discussed in the theoretical background, it is worth to investigate ethanol as the target molecule for the CO_2RR (see section 2.2). Thus, the first aim of this thesis is to develop a suitable catalyst for that purpose. Pure Cu electrodes often exhibit insufficient selectivities for C_{2+} products (see section 2.1), which motivates the alloying approach utilized for the development of the catalyst in this doctoral thesis. To pursue this approach, a new bimetallic catalyst consisting of Cu and Ag, referred to as copper-silver nanoplates (CuAg NPls), is synthesized. The investigation of this catalyst is conducted using an H-type electrolyzer, a suitable cell design for catalyst development (see section 2.3.1). This test cell was previously employed in the master thesis with the topic "Preparation and Characterization of Modified Metal Surfaces as a Catalyst for the Electrochemical Reduction of Carbon Dioxide" by Elisabeth Robens 2020 at IEK-9 (now renamed IET-1) that preceded this doctoral thesis. However, before delving into the study of the CuAg NPls, optimization of this H-type electrolyzer is undertaken, concerning its cell setup and measuring method (see section 4.1). Subsequent to the cell optimization, the morphology, various compositions, and the activity of the CuAg NPls are discussed, and their catalytic performance in the CO_2RR is analyzed under different conditions (see section 4.2). Once suitable CuAg NPls for the CO_2RR to ethanol are developed, the second objective is to investigate their transfer into an industrially more relevant cell design utilizing a GDE. For this purpose, the FlexCell from Gaskatel is employed. As preliminary work, the performance of commercial copper nanoparticles (Cu NPs) in both the H-type electrolyzer and the FlexCell is compared to gauge the comparability of data obtained from these two cell designs (see section 4.3.1). The examination of the CuAg NPls in the FlexCell system begins with a necessary modification to the catalyst synthesis process. Subsequently, after the manufacturing of the GDE, the catalytic performance undergoes investigation and enhancement (see section 4.3.2). Additionally, experiments solely involving the silver nanoplates (Ag NPls) are conducted, providing inspiration for future work based on this thesis (see section 4.3.3).

4.1 Optimization of H-Type Electrolyzer

Before delving into the study of the CuAg NPls, optimization of the H-type electrolyzer is required to carry out the desired reaction. This particularly concerns its cell setup – including the Haber-Luggin capillary and the CO_2 gas supply – and the measuring method. In the H-type electrolyzer utilized in the master thesis that preceded this doctoral thesis, mounting the Haber-Luggin capillary closer than 5 mm to

the WE posed challenges, as gas bubbles could penetrate the capillary, obstructing the ionic conductivity between WE and RE. Thus, the smallest possible distance between capillary and WE was 5 mm. At this distance, between a Cu foil as WE and the capillary an ionic resistance of around 65 Ω is measured via impedance due to 0.1 M $KHCO_3$ electrolyte (see figure 20a). Given that the IR drop is directly proportional to this resistance (see equation (6)), lowering it would result in a smaller IR drop, thus ensuring a more reliable correction of the measured potential at the WE. An approach to minimize the ionic resistance between the WE and RE involves decreasing the distance between WE and capillary (see section 2.4). To achieve this, hydrophilic Nafion strips secured with Kapton tape are inserted into the capillary's tip, preventing gas bubbles from entering while preserving constant ionic conductivity. Due to this modification developed by Dr. Burkhard Hecker, mounting the capillary at a distance of less than 1 mm from the WE becomes feasible, thereby lowering the resistance to around 5 Ω (see figure 20b). This modification facilitates a more reliable correction of the measured potential at the WE, prompting the adoption of this new Haber-Luggin capillary design for all experiments performed with the H-type electrolyzer.

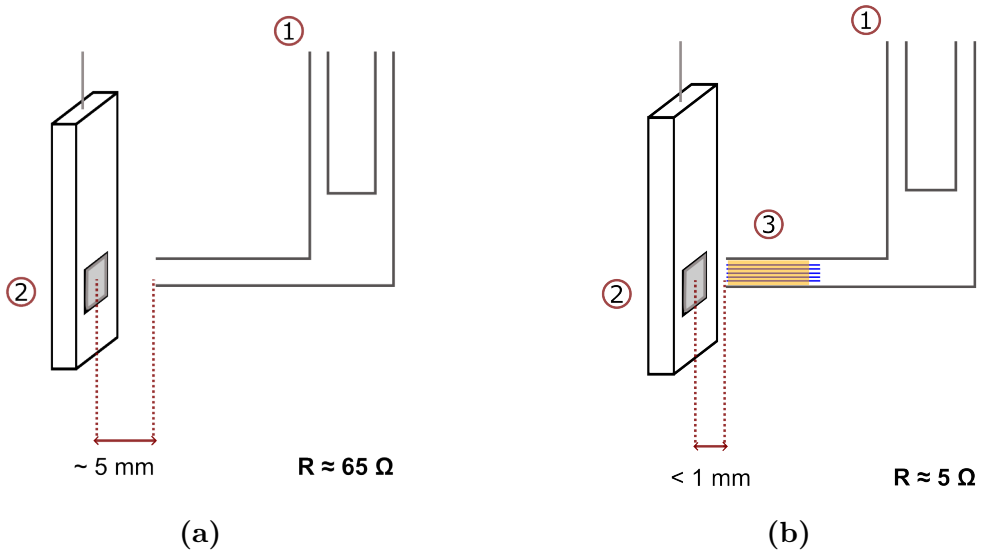

Figure 20: Schematic representation of the (a) old and (b) new design of the Haber-Luggin capillary: (1) reference electrode inserted with Haber-Luggin capillary, (2) working electrode, and (3) tip of the capillary filled with Nafion stripes (blue), secured with Kapton tape (orange).

A finding of the master thesis that preceded this doctoral thesis was the observed depletion of CO_2 at the cathode in the utilized cell setup. This resulted in an elevated evolution of H_2 and a decreased formation of CO_2RR products. In this master thesis, the CO_2 gas supply was mounted behind the cathode, resulting in a elongated diffusion path for the dissolved CO_2 to reach the cathode (see figure 21a). To address this issue, the CO_2 gas supply is now relocated in front of the cathode to shorten the diffusion

path for CO_2 (see figure 21b). To evaluate the impact of this modification, copper foil is once again employed as cathode material. Shifting the gas inlet position from behind of the cathode to in front it, results in a decrease in the Faradaic efficiency (FE) of H_2 from 66 % to 37 %, consequently promoting a higher formation of CO_2RR products (see figure 22). This adjustment is therefore implemented in all following experiments conducted with the H-type electrolyzer.

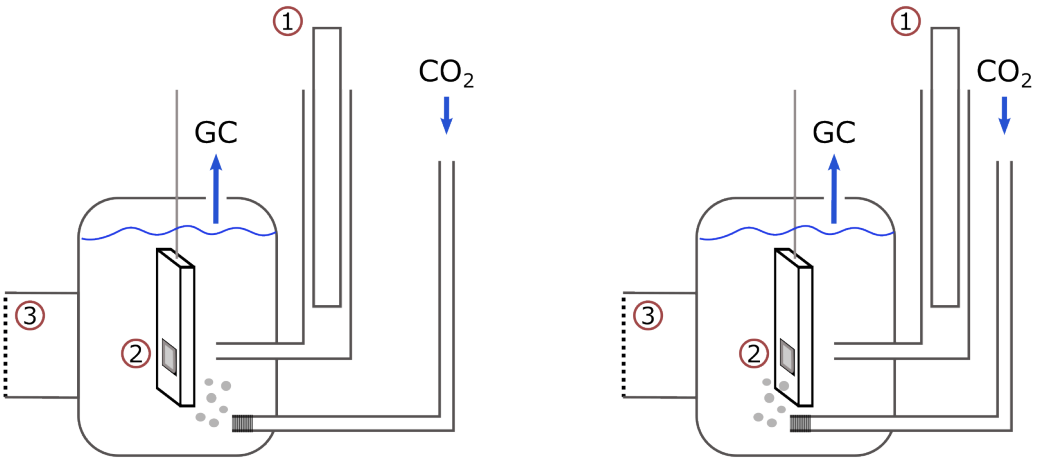

(a) **(b)**

Figure 21: Schematic illustration of the (a) old and (b) new design of the CO_2 gas supply in the cathode compartment of the H-type electrolyzer. In the old design, the gas supply is mounted behind the working electrode, whereas in the new design it is inserted in front of it. Note: For simplicity, the RE is drawn on the backside of the cathode; in reality, the RE points to the front side of the WE (compare figure 20).

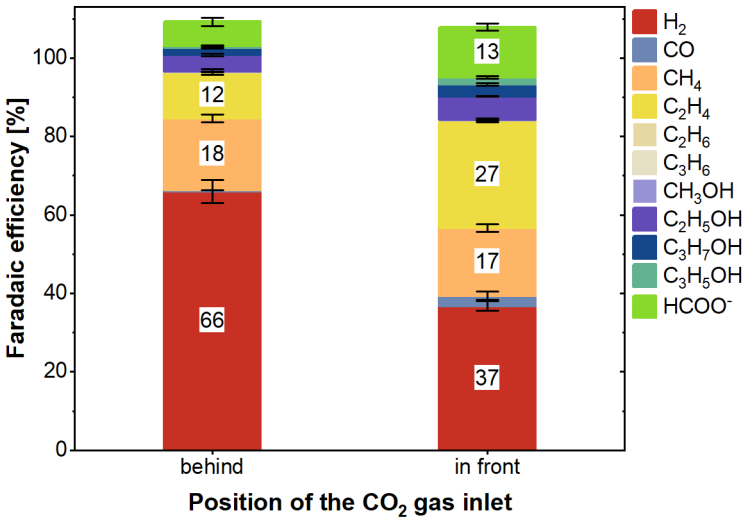

Figure 22: Influence of the positioning of the CO_2 gas inlet on the *FE*s measured using a Cu foil as WE. The measurements are performed at a constant potential of -1.0 V vs. RHE (IR-corrected), resulting in a current density of around -7 mA cm^{-2} for the experiment conducted with the gas inlet behind the WE and of around -8 mA cm^{-2} for the experiment with the gas inlet in front of the WE. The measurements are performed for 100 minutes using a 0.1 M $KHCO_3$ electrolyte and the data are averaged over two individual runs.

The new placement of the CO_2 gas inlet, however, necessitates a modification of the measuring method. In the master thesis, CO_2RR measurements were carried out under potential control while measuring the corresponding current (chronoamperometry (CA)). However, this approach can lead to incorrect results with the new setup, as there is a risk of a gas bubble getting trapped between the WE and the Haber-Luggin capillary due to the relocation of the CO_2 gas inlet in front of the WE (see figure 23 on the left). Under normal conditions – no gas bubble is trapped (see figure 23 on the right) – the applied potential leads to a constant current at the WE, in this case of around -14 mA (see figure 24a; white areas). However, if a gas bubble is trapped, the applied current changes (see figure 24a; gray areas). Due to the trapped gas bubble, a shift in the potential of the WE is detected, which prompts the potentiostat to readjust the applied current in order to counteract the change in potential and maintain a constant potential. Since the change in the measured potential is solely artificial, caused by the trapped gas bubble, the current readjustment is invalid and leads to an incorrect measurement.

To address this problem, the following CO_2RR experiments are performed under constant current (chronopotentiometry (CP)) instead of constant potential. Under this condition, the trapping of a gas bubble is detectable by an increase in overpotential and its release by a sharp return to the original value (see figure 24b; gray areas).

The primary difference between CP and CA measurement is that in constant current mode, the potentiostat does not make any adjustments to the current due to the trapped gas bubble, as the current is defined as constant. Consequently, there is no false improvement in the CP measurement. Nevertheless, it is important to note that any measured artificial fluctuations have to be excluded post-measurement in order to correctly determine the potential at the WE. In the following, all CO_2RR experiments in the H-type electrolyzer are conducted under constant current.

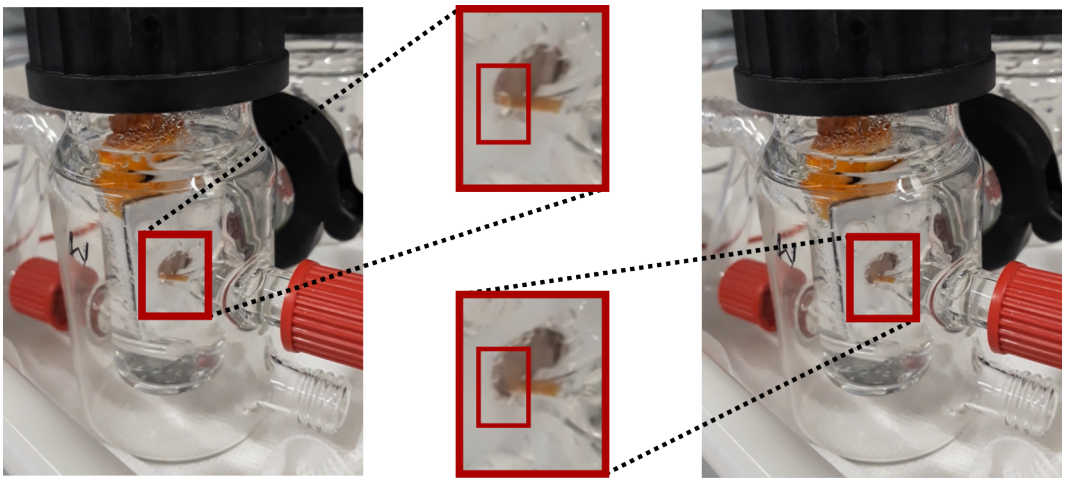

Figure 23: Photo of the cathode compartment of the H-type electrolyzer: (left) a gas bubble is trapped between WE and Haber-Luggin capillary, (right) no gas bubble is trapped. In addition, magnifications of the highlighted areas are shown in the middle. The measurement is performed at a constant potential of -1.0 V vs. RHE and in a 0.1 M $KHCO_3$ electrolyte.

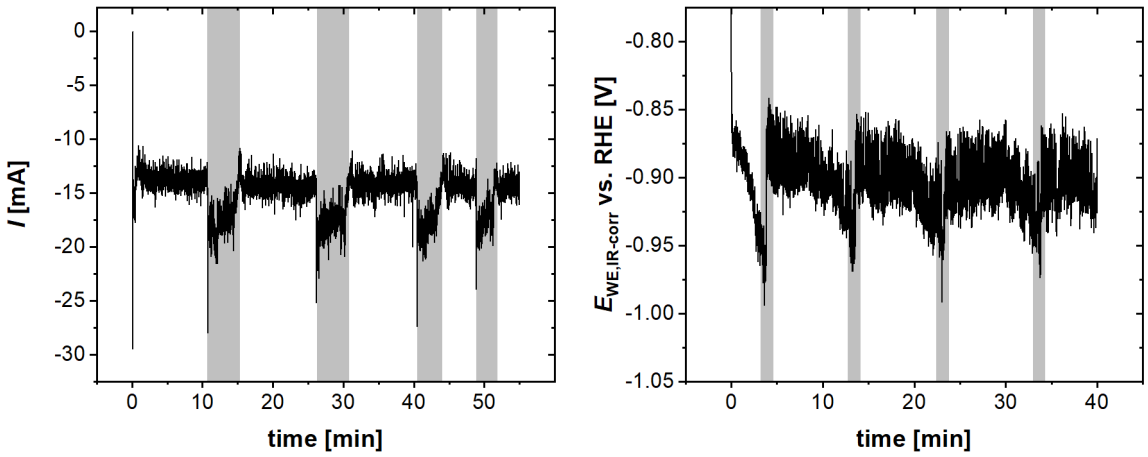

(a) (b)

Figure 24: Effect of a trapped gas bubble on the measured values: (a) measurement at a constant potential of -1.0 V vs. RHE, (b) measurement at a constant current of -10 mA. The gray areas mark in (a) the time interval in which a gas bubble is trapped between the WE and Haber-Luggin capillary and in (b) the time at which a gas bubble is released. Both measurements are conducted in a 0.1 M $KHCO_3$ electrolyte.

4.2 Investigation of CuAg NPls in H-Type Electrolyzer

This section is based on the publication "Bimetallic Copper-Silver Catalyst for the Electrochemical Reduction of CO_2 to Ethanol" published by Elisabeth Robens *et al.* 2023 in ACS Applied Energy Materials.[54]

As already mentioned, the first aim of this doctoral thesis is the development of a suitable catalyst for the CO_2RR to ethanol. In the following section, the morphology, composition, stability, and activity of the new self-synthesized CuAg NPls are discussed. Subsequently, its calytic performance in the CO_2RR is analysed under different conditions.

4.2.1 Catalyst Morphology, Composition, and Activity

For the new bimetallic Cu-Ag catalyst, a nanostructured material is chosen as the basis, namely Ag NPls, to synthesize a catalyst with high activity.[77–79] As basic material Ag and not Cu is selected, as nanostructured Cu is known to be structurally unstable under CO_2RR conditions.[83,84] Subsequently, Cu is electrolessly deposited on the Ag NPls, resulting in a shared Cu-Ag surface (see section 3.2.1). For information on the pure Ag NPls, the aforementioned master thesis preceding this doctoral thesis and the publication "Effects of Synthesized Silver Nanoplate Structures on the Electrochemical Reduction of CO_2" by Dr. Burkhard Hecker *et al.* published in the

Journal of the Electrochemical Society in 2023 are recommended.[79]

The morphology of the CuAg NPls is analyzed by taking SEM images of the top surface of the catalyst and the cross-section (see figure 25a-c). The images show that the catalyst consists of a porous catalyst film on Ag foil composed of silver plates with a nanoscale thickness forming a bead-like structure of one to two micrometers. The height of the catalyst layer can be determined to be 10 to 15 micrometers and the beads form branched chains. The location of Cu formed by electroless Cu deposition can be visualized by overlaying the SEM image (figure 25a) with a Cu EDX mapping. It can be seen that Cu depicted in red was deposited on the Ag NPls (see figure 25d).

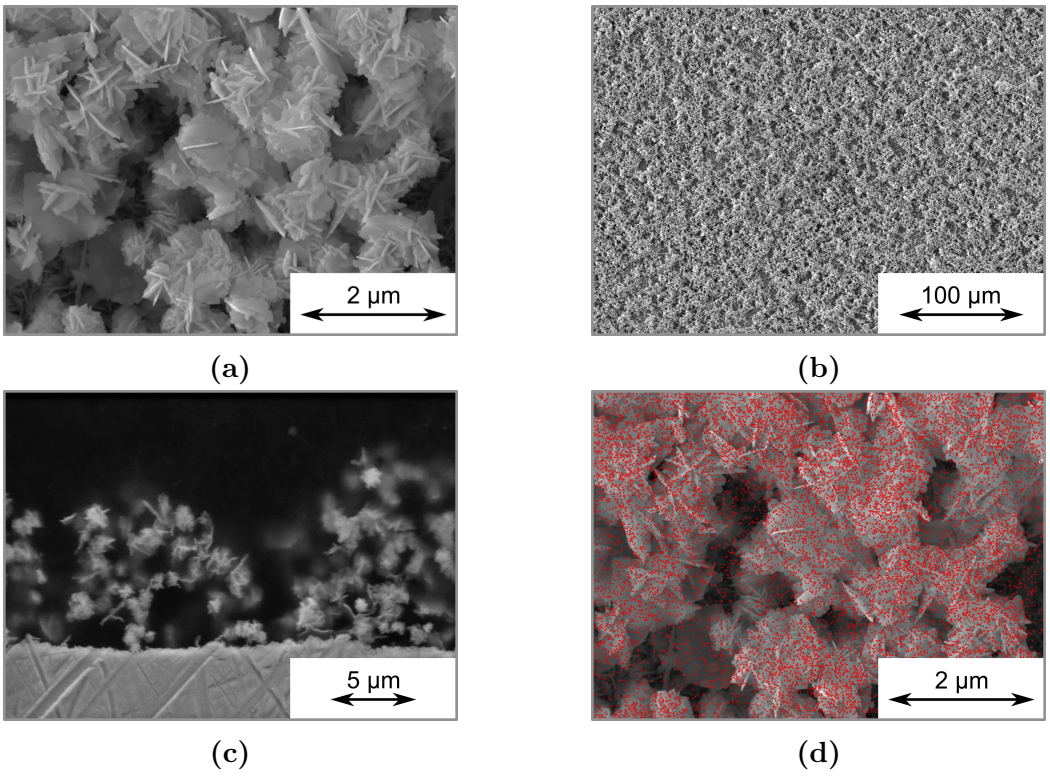

Figure 25: (a,b) SEM images of the top surface of CuAg NPls with 45 % near-surface Cu content and (c) a cross-section of the resin-embedded catalyst with 90 % near-surface Cu content. Additionally, SEM/EDX overlay of CuAg NPls with 45 % near-surface Cu content (d, Cu depicted in red).[54]

To determine the crystalline phase of the new bimetallic catalyst, an XRD pattern is measured (red line in figure 26). For comparison, also an XRD measurement for pure Ag NPls (blue line) is performed, and reference data from the ICS database[85] for Ag (black line) and Cu (green line) are shown. The detected peaks indicate that the Ag NPls and the deposited Cu have a polycrystalline structure. Moreover, the data show no shift in the Ag peaks between the pure Ag NPls pattern (blue line) and that with Cu (red line). Thus, with Cu deposition, no changes in the lattice parameters

of Ag are observed.

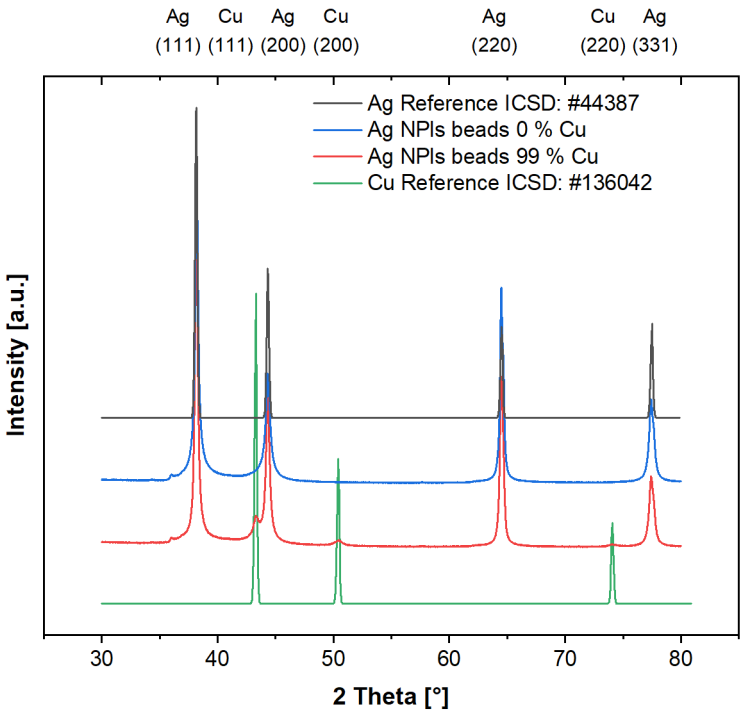

Figure 26: XRD patterns of Ag NPls and with Cu deposited Ag NPls. Additionally, XRD patterns from the ICS database[85] of Ag and Cu are shown. Cu content is determined by XPS. The corresponding element and surface orientation of each peak are indiacted above the diagram.[54]

In this doctoral thesis, CuAg NPls with several amounts of Cu on the surface are synthesized (see section 3.2.1). To assess the synthesis and the respective electrocatalytic CO_2RR performance, a systematic information about the near-surface Cu content as a function of the total Cu content has to be obtained. The Cu content in the entire catalyst layer is measured by detaching the catalyst layer from the silver foil as described in section 3.4.3 and subsequently analyzing the Cu content by ICP-MS. Since this is a destructive method, additional non-destructive EDX measurements are performed prior to the electrochemical experiments and the final ICP-MS analysis. Plotting the two different Cu contents against each other, a linear correlation is obtained, namely y = 1.81 x, where x and y correspond to total Cu content measured by ICP-MS and the Cu content measured by EDX, respectively (see figure 27a). This relation can be used as a calibration for a non-destructive determination of the total Cu content using the EDX data. The near-surface Cu content is obtained by XPS measurements (see section 3.4.4). The measured data are plotted versus the total Cu content calibrated from the EDX data (see figure 27b). The near-surface Cu content is higher than the average total Cu content. This is reasonable since Cu is only present on the surface of the catalyst due to the subsequent Cu deposition on the

Ag NPls. Moreover, the data show that bimetallic catalysts have been synthesized with a near-surface Cu content ranging from 21 % to 99 %. Since the surface of the catalyst is the key area of the catalytic reaction, the near-surface Cu content is used in the following to distinguish between the different catalyst samples.

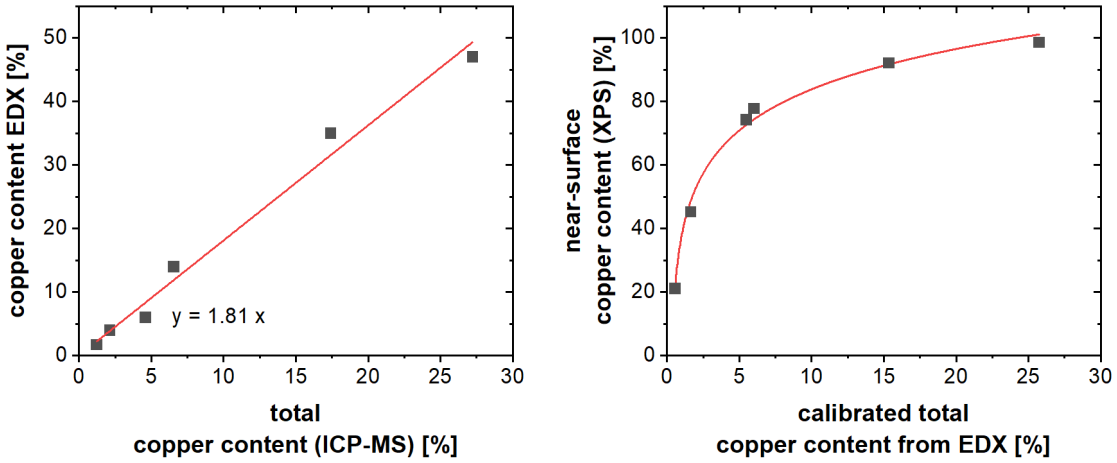

(a) (b)

Figure 27: (a) Linear correlation between Cu content measured by EDX and the total Cu content measured by ICP-MS. The red line represent the linear fit of the data. (b) Comparison of the total Cu content (calibrated from EDX) and the near-surface (measured by XPS) Cu content of several samples of the new bimetallic catalyst. The red line provides a guide-to-the eye for the reader.[54]

To investigate whether the Cu content maintains during the reaction, the electrolyte after each CO_2RR experiment is analyzed for its Cu content (see section 3.4.3). Irrespective of the Cu content of tested catalyst, the averaged amount of dissolved Cu is approximately 0.3 µg. Comparing this to the catalyst with the lowest Cu content, 7 % of the Cu is dissolved in the electrolyte during the reaction. In contrast, only 0.1 % of Cu is dissolved for the catalysts with the highest Cu content.

The activity of a catalyst is a key factor for its performance (see section 2.4). Thus, the activity of the bimetallic catalysts with different Cu content is investigated by measuring CV curves in the potential range from -0.1 V to -0.5 V vs. RHE with a scan rate of 20 mV s^{-1} and in a 0.1 M $KHCO_3$ electrolyte (see figure 28). The upper potential limit for these experiments is chosen to prevent oxidation of Cu, as this could alter the catalyst. To ensure reproducibility, the given data are averaged values of at least two samples with similar Cu content. From -0.1 V to -0.25 V vs. RHE, the curves of the different samples are quite similar, since in this potential range mainly capacitive current and barely CO_2RR or HER occurs. At more negative potentials, the reductive current density increases due to the starting CO_2RR and HER. With higher Cu content this effect is more pronounced. Possible reasons for higher current

densities are a larger electrochemical surface area (ECSA) or a higher activity of the material. Tentatively, the ECSA should be identical for all catalyst specimens since the basic structure, namely the Ag NPls, is the same for all catalysts. This is supported by similar double layer capacities ($4.4 \pm 0.8\,\mathrm{mF\,cm^{-2}}$, determined from CV curves) for the different samples. Therefore, the reason for the increased reductive current density with higher Cu content has to be an increased activity of the catalysts with larger Cu content. To support this hypothesis, CV curves are performed with a Ag and a Cu foil polished under the same conditions (P4000 ultra-fine polishing paper) and therefore with an approximately identical ECSA (inserted graph in figure 28). The curves show a significantly higher reductive current density for the Cu than for the Ag foil, which is consistent with the above hypothesis.

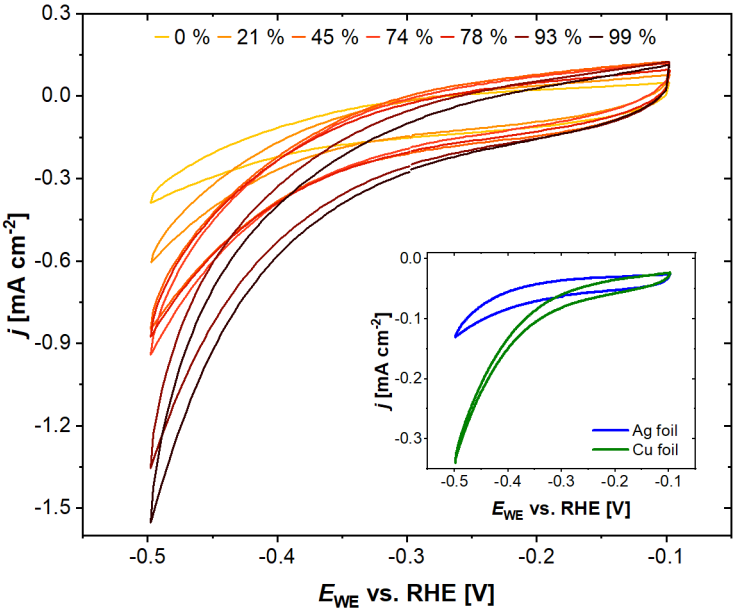

Figure 28: CV curves of the new bimetallic catalyst with different near-surface Cu contents (see legend, measured by XPS). The measurements are performed in a potential range from -0.1 V to -0.5 V vs. RHE with a scan rate of $20\,\mathrm{mV\,s^{-1}}$ and in a 0.1 M $KHCO_3$ electrolyte. To ensure reproducibility, the given data are averaged values of at least two samples with similar near-surface Cu content. The inset shows the CV curves for equally polished Ag and Cu foils as reference.[54]

4.2.2 Catalytic Performance in CO_2RR

After the characterization of the new catalyst, its catalytic performance in the CO_2RR is tested. For this purpose, the catalysts with different near-surface Cu contents ranging from 21 % to 99 % are measured at $-20\,\mathrm{mA\,cm^{-2}}$ for 100 min (see section 3.2.3). For simplicity, the near-surface Cu content measured by XPS will be referred to only as Cu content in the following. The gaseous and liquid samples taken show relatively

constant values over the experimental time of 100 minutes. Therefore, a steady reaction over time can be assumed. The shown data are average values of at least two individual measurements. The error bars are calculated standard deviations considering the individual runs. Moreover, the respective potential at the WE, $E_{\text{WE, IR-corr.}}$, is calculated using equation (16) and is indicated on the x-axis of figure 29. The decrease in the negative potential with increasing Cu content at constant current densities can be explained by the higher activity of the catalyst with higher Cu contents (see section 4.2.1). The influence of the potential on the performance of the catalyst is analyzed at the end of this section.

Figure 29 shows that, starting from the highest Cu content of 99 %, minimizing the Cu content down to 45 %, results in a better-performing catalyst with less competitive and parasitic reduction of water to H_2 (i.e. HER, see section 2.1). More specifically, the *FE* of H_2 is decreased from 62 % to 27 %. Lowering the Cu content even further does not show any additional improvements. The minimized H_2 evolution can be explained by the following two facts. Firstly, the amount and thus the surface area of Ag increases with decreasing Cu content. This also enhances the formation of CO since Ag surfaces mostly produce CO under these conditions (see figure 1). As a result, the CO coverage of the Cu surface is higher, leading to CO poisoning of the Cu surface for the HER and thus to an enlarged CO_2RR.[3,86] Secondly, Ag has a higher binding energy for the intermediate *H for the HER than Cu.[20,87] Thus, the binding of *H on Ag is less favored than on Cu, and with it, the formation of H_2. A minimized Cu content, therefore, lowers the HER. Furthermore, the data indicate that the ethanol formation, in contrast to the H_2 evolution, is increased to 23 % by decreasing the Cu content down to 45 %. Additionally, the ethanol-to-ethylene ratio is shifted from ethylene at higher Cu contents to ethanol at lower Cu contents. Consequently, using the catalyst containing 45 % Cu on its near-surface, the reaction can be tailored to the target molecule of this thesis, namely ethanol. The first objective of this thesis has thus been achieved. In addition, the reason of the favored formation of ethanol is discussed below.

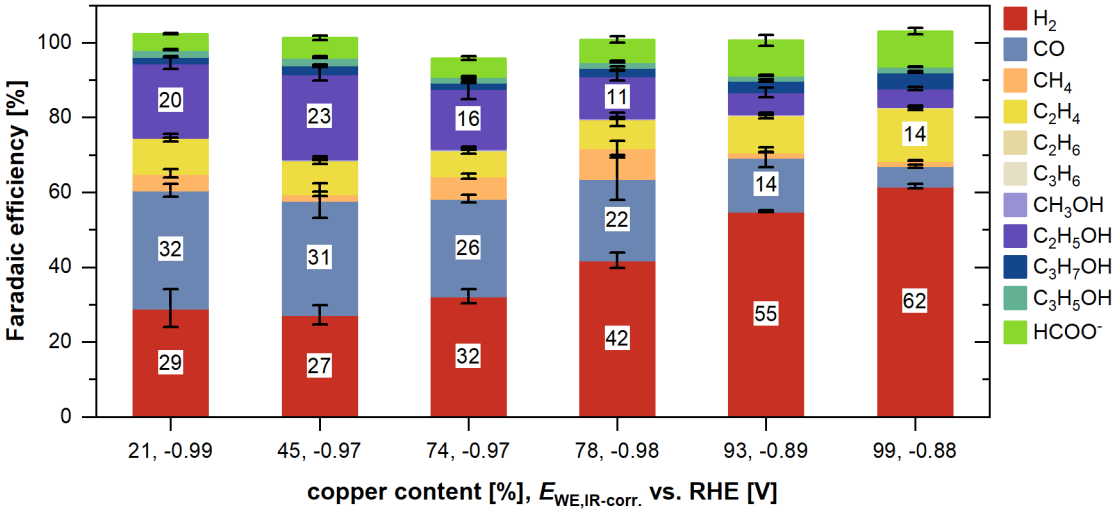

Figure 29: Faradaic efficiency as a function of the near-surface Cu content (measured by XPS). The experiments are performed at -20 mA cm^{-2} and for 100 minutes. The data are averaged over two to three individual measurements.[54]

If the ethanol-to-ethylene ratio is plotted versus the *FE* of CO, a systematic relation between the two quantities is observed (see figure 30), clearly indicating an optimum for ethanol formation over the competitive ethylene formation. At levels of formed CO above 20 %, the formation of ethanol starts being favored over the formation of ethylene, recognizable by a ratio of the *FE*s of ethanol and ethylene greater than one. However, at amounts of CO larger than 30 % and with decreasing Cu content (below Cu content = 21 %), the favoring of ethanol is not further increased. Expressed in numbers, the ethanol-to-ethylene ratio is increased from 0.4 at a FE(CO) of 5.4 % (Cu content = 99 %) to 2.6 at a FE(CO) of 30.5 % (Cu content = 45 %). This nicely supports the calculations presented in section 2.1, which show that an excess of *CO due to the high Ag content opens up an alternative reaction pathway that enables the selective formation of ethanol instead of ethylene (see figure 5).[42] These calculations have so far only been supported by experiments in which the ratio of the *FE*s of ethanol and ethylene could be increased to 1.1 by adding Ag to the Cu catalyst (see section 2.1), which represents only a slight preference for ethanol over ethylene. However, with the results obtained in this doctoral thesis, the calculations can be proven with experiments in which ethanol formation is clearly favored over the formation of ethylene in excess of CO.

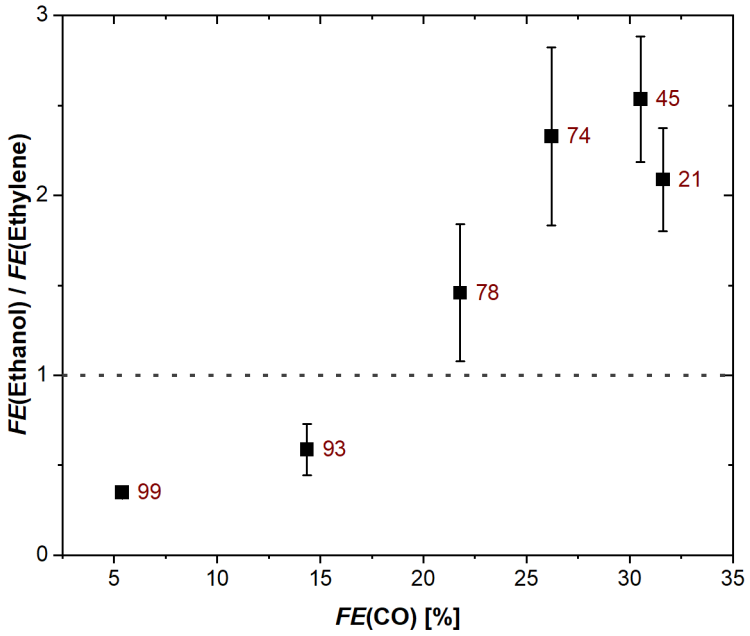

Figure 30: Correlation between the Faradaic efficiency of CO and the ethanol-to-ethylene ratio. The red numbers represent the copper content (measured by XPS) of the used catalyst. The error bars are calculated by Gaussian error propagation from the errors of the Faradaic efficiency of ethanol and ethylene. The dashed horizontal line marks the transition between the catalysts favoring ethylene (below) or ethanol (above) formation.[54]

To figure out if the catalyst performance could be further enhanced and to analyze the influence of the current density and the respective potential on the performance, the best-performing catalyst (45 % Cu) is tested at two additional current densities and corresponding potentials, namely -10 mA cm^{-2} (-0.88 V vs. RHE) and -30 mA cm^{-2} (-1.09 V vs. RHE) (see figure 31). These measurements are conducted for 55 min and the shown data are averages of three individual runs. At -10 mA cm^{-2}, the amount of CO is dramatically increased, while the formation of ethylene and ethanol is significantly decreased. For Cu catalysts, the formation of C_2 products would already be expected at this potential (see figure 3 and [88, 89]), as can also be observed for the CuAg NPls with 99 % Cu content (see figure 29). However, comparing the data with bimetallic Cu/Ag catalysts, this behavior is in line with the literature.[42,47] In contrast, a more negative current density and potential (-30 mA cm^{-2}, -1.09 V vs. RHE) results in higher H_2 and methane evolution, but lower CO formation. Simultaneously, the percentage of ethanol decreases slightly. This is consistent with the data on the product formation as a function of the overpotential discussed in section 2.1 and other data from literature.[22,42] Since the amount of H_2 should be minimal and that of ethanol maximal, -20 mA cm^{-2} and about -1.0 V vs. RHE appear to be a suitable current density and potential, respectively, for CO_2 reduction with the used bimetallic catalyst and cell setup.

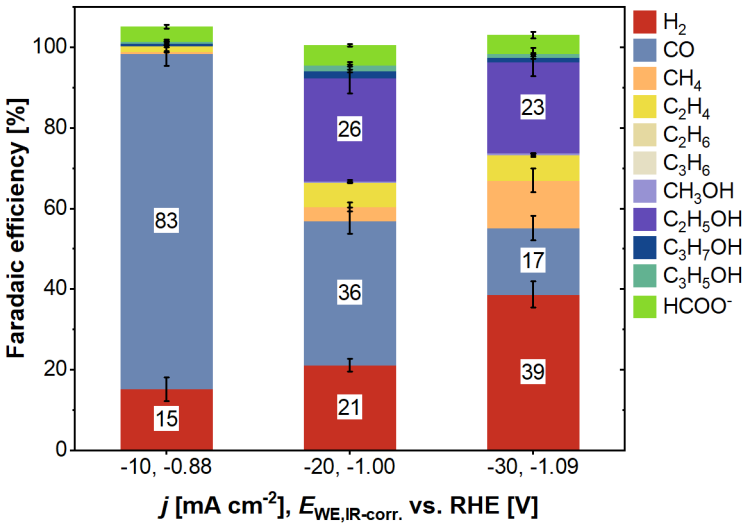

Figure 31: Faradaic efficiency of 45 % copper catalysts (measured by XPS) as a function of current density and potential at the working electrode. The measurements were performed for 55 minutes and the data are averaged over three individual runs.[54]

In summary, a newly designed bimetallic catalyst was synthesized, consisting of Ag NPls partially coated with Cu. By varying the duration of electroless Cu deposition, catalysts with different Cu contents were prepared. When determining their Cu content using different techniques, a linear relation between the Cu content measured by EDX and by ICP-MS was found. This relation enabled a non-destructive measurement of the Cu content in the entire catalyst layer. In addition, the activity of the catalyst was observed to rise with increasing near-surface Cu content. Furthermore, the influence of the Cu content on the performance of the catalyst in the CO_2RR was investigated. It was found that a Cu-to-Ag ratio of about 50:50 shows the most beneficial interplay of Cu and Ag, resulting in the highest ethanol formation, while concurrently suppressing the parasitic formation of H_2 and the competing ethylene evolution. The first objective of this thesis was thus achieved. Lastly, a comparison of three different current densities showed that -20 mA cm^{-2} and about -1.0 V vs. RHE are suitable conditions for the used catalyst and cell design.

4.3 Transfer of Catalyst to Gas Diffusion Electrode

Parts of this section are based on the publication "Power-to-Ethanol using Bimetallic Catalysts: Reactions Paths, Transfer to Gas Diffusion Electrode, and Future Perspectives" published by Elisabeth Gräfin von Westarp *et al.* 2024 to Electrochemical Science Advances.[12]

In the previous section, suitable CuAg NPls were developed for the CO_2RR to ethanol in an H-type electrolyzer. However, as already mentioned, for industrial use it is neces-

sary to conduct the CO_2RR in cell designs with GDEs. A GDE shortens the diffusion path of CO_2, which overcomes mass transport limitations and thus accelerates the reaction and enables higher current densities (see section 2.3.2). First, a simple, static liquid-phase electrolyzer (FlexCell from Gaskatel) is used as the cell design with a GDE. Here, the focus can be laid on the transfer from the solid electrode to a GDE, as there are less other parameters to consider, e.g. flow rate in flow cells. When transferring from a solid electrode in an H-type electrolyzer to a GDE in a static liquid-phase electrolyzer, various parameters must be taken into account. Firstly, the catalyst is required in larger quantities because GDEs are typically larger than electrodes in H-type electrolyzers, and the catalyst is often needed as a powder to deposit the catalyst on the GDL. Thus, the synthesis of the catalyst often needs to be modified. Secondly, if the catalyst is applied as a powder, the choice of binder, the catalyst loading, the binder loading, the choice of solvent, and the method of ink deposition are important for the preparation of the catalyst layer. Furthermore, the choice of the GDL itself is also crucial, as its composition and architecture can effect the mass transport within electrode and the overall performance of the electrode. Finally, the setting of the cell can also have an influence, e.g. the applied current density or the flow rate of the CO_2 gas supply.

4.3.1 Influence of the Cell Design on Commercial Cu NPs

Before investigating this transfer with the self-made CuAg NPls, the performance of two types of commercially available Cu NPs in the H-type electrolyzer and in the FlexCell is compared as preliminary work to get a first idea of how comparable the data obtained in these two cell design are. The first type of Cu NPs has a diameter range from 60 nm to 80 nm (Cu NPs “big”) and the second type from 40 nm to 60 nm (Cu NPs “small”).

4.3.1.1 Performance of Cu NPs in H-Type Electrolyzer

To evaluate the performance of the Cu NPs in the H-type electrolyzer, they are spray coated onto glassy carbon at a catalyst loading of $2\,mg\,cm^{-2}$ with Nafion as binder (see section 3.2.2). Nafion is chosen as binder due to its common use in GDEs according to the literature.[90–92] In the following, all graphs showing *FE*s are time-resolved and not averaged, as a steady reaction over time is often not observed. For the experiments in the H-type electrolyzer, the first injection after 10 minutes is not shown, as it did not produce reliable results. In the initial experiment, the Cu NPs “big” are tested at a current density of $-44\,mA\,cm^{-2}$ for 100 minutes (see figure 32a). Under these conditions, predominantly parasitic H_2 evolution occurs ($FE(H_2) > 70\,\%$) (see figure 32b). The main product of the CO_2RR is ethylene with a *FE* of about 13 %. The predominant formation of H_2 suggests that the applied current density of $-44\,mA\,cm^{-2}$ surpasses the limiting current density of the system, resulting in mass transport limitations of CO_2 (see section 2.1). Two potential solutions are proposed

to address this issue: either lowering the current density or decreasing the activity of the electrode. According to literature experiments, a suitable potential for the formation of C_{2+} products on Cu electrodes is -1.0 V vs. RHE (see figure 3).[22] Even when a current density of -44 mA cm^{-2} is applied to the WE, the resulting negative potential at the WE is below that of -1.0 V vs. RHE (see figure 32a). Therefore, lowering the current density is not feasible, as the desired potential could not be attained. If, on the other hand, the activity of the electrode is decreased, a lower current density is required to achieve the desired potential of -1.0 V vs. RHE, enabling that the required current density does not surpass the limiting current density. This decrease in activity can be accomplished by decreasing the catalyst loading. Consequently, the catalyst loading is adjusted from 2 mg cm^{-2} to 0.7 mg cm^{-2}.

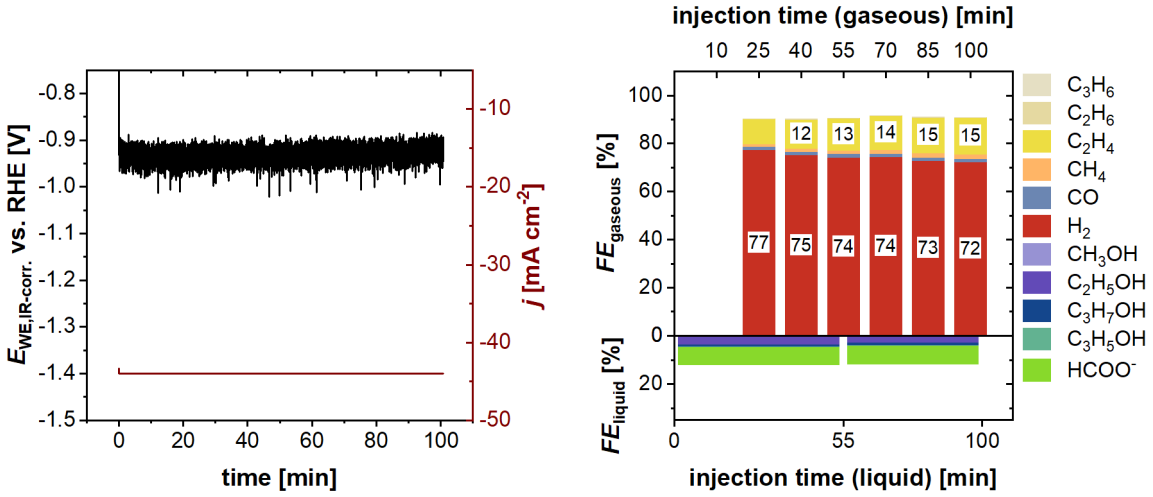

(a) **(b)**

Figure 32: CO_2RR at a constant current density of -44 mA cm^{-2} using Cu NPs "big" as catalyst with Nafion as binder and a catalyst loading of 2 mg cm^{-2} on glassy carbon: (a) plot of the applied current density and the resulting potential at the WE versus time, (b) graph with the calculated *FE*s time-resolved. The experiment is conducted in the H-type electrolyzer using a 0.1 M $KHCO_3$ electrolyte.

To assess whether the smaller catalyst loading indeed diminishes the activity of the electrode, CV curves of both electrodes are measured and compared within the potential range of -0.1 V to -1.1 V vs. RHE (without IR correction), employing a scan rate of 20 mV s^{-1} (see figure 33). It is evident that applying the same potential to the electrode with the smaller catalyst loading results in a lower negative current density (valid for $E_{WE,IR-corr.}$ vs. RHE $>$ |-0.5 V|). As the current density describes the activity (see equation (7) and section 2.4), this decrease also reflects a decline in activity. In addition to this primary result, two additional observations can be made: First, the lower potential limits shown in the graph deviate from those set in the measurement, as they are IR-corrected values. This deviation is greater for the

measurement with the higher catalyst loading. The IR drop describes the difference between the measured potential and the actual potential at the WE, caused by the resistance of the electrolyte (see section 2.4). This effect becomes more pronounced at higher current densities, as the IR drop increases directly with the current (see equation (6)). Consequently, the higher catalyst loading of $2\,\mathrm{mg\,cm^{-2}}$, which leads to larger negative current densities, results in greater deviations in the lower potential limit compared to the lower catalyst loading of $0.7\,\mathrm{mg\,cm^{-2}}$. Second, higher noise can be observed in the measured data of the CV curve at higher catalyst loading. The noise can be attributed to the formation of gaseous products that interfere with the measurement of the potential at the WE. Since product formation increases with the current density, more gaseous products that interfere with the measurement signal are generated at higher current densities. As the higher catalyst loading leads to higher current densities and therefore to more gaseous products, these measurement data are noisier than those from the measurement with the lower catalyst loading.

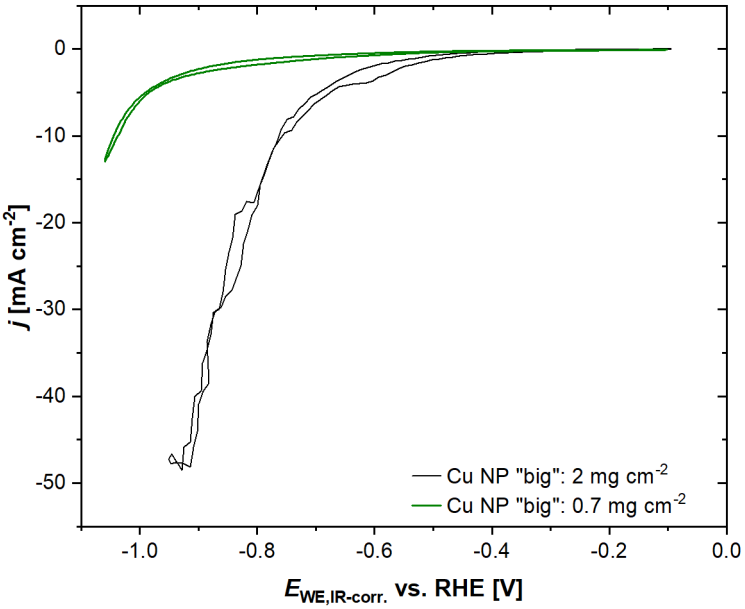

Figure 33: CV curves using the Cu NPs "big" as catalyst with Nafion as binder and different catalyst loadings on glassy carbon: $2\,\mathrm{mg\,cm^{-2}}$ is depicted in black and $0.7\,\mathrm{mg\,cm^{-2}}$ in green. The measurements are performed in a potential range from -0.1 V to -1.1 V vs. RHE prior the IR correction with a scan rate of $20\,\mathrm{mV\,s^{-1}}$. The experiments are conducted in the H-type electrolyzer using a 0.1 M $KHCO_3$ electrolyte.

In order to attain the desired potential of -1.0 V vs. RHE, a current density of $-10\,\mathrm{mA\,cm^{-2}}$ is applied to the WE with the smaller catalyst loading, considering the CV data. Throughout the measurement time, the negative potential rises to -1.1 V vs. RHE (see figure 37a). With the lower catalyst loading and current density, the *FE* of H_2 is mitigated to around 40 % (see figure 34b). However, over the course of

the experiment, the *FE* of H_2 nearly doubles to around 80 %. At the same time, the *FE* of the CO_2RR products declines. This deterioration in the performance of the Cu NPs "big" during the measurement time indicates aging of the electrode. Further analysis focuses on the individual *FE*s of the CO_2RR products. Methane emerges as the predominant gaseous CO_2RR product, with an initial *FE* of 20 %, declining to 5 % by the end of the experiment. Ethylene follows with a *FE* decreasing from 8 % to 3 %. In contrast, CO is generated with a *FE* of less than 2 %. The main liquid product, formate, exhibits an initial *FE* of 16 %, decreasing to 11 % at the end of the measurement, followed by methanol and ethanol.

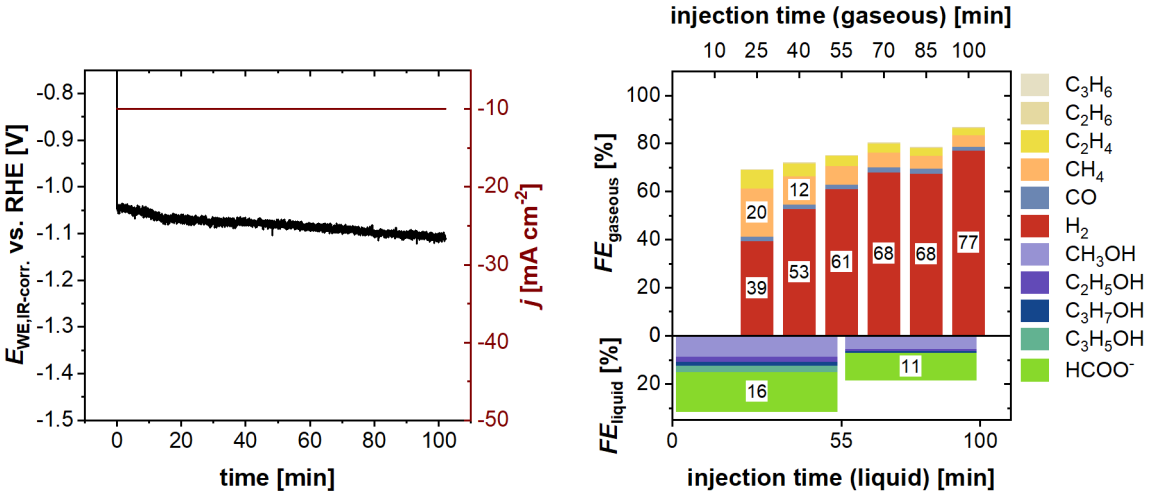

Figure 34: CO_2RR at a constant current density of -10 mA cm^{-2} using Cu NPs "big" as catalyst with Nafion as binder and a decreased catalyst loading of 0.7 mg cm^{-2} on glassy carbon: (a) plot of the applied current density and the resulting potential at the WE versus time, (b) graph with the calculated *FE*s time-resolved. The experiment is conducted in the H-type electrolyzer using a 0.1 M $KHCO_3$ electrolyte.

As a second commercial catalyst, the Cu NPs "small" with the same catalyst loading (0.7 mg cm^{-2}) and the same binder (Nafion) as used for the Cu NPs "big" are tested in the H-type electrolyzer. Prior to the CO_2RR, another CV measurement is carried out (see figure 35). Comparing these data shown in blue with those of the Cu NPs "big" depicted in green, it is evident that applying the same potential to the Cu NPs "small" leads to a higher negative current density (valid for $E_{\mathrm{WE,IR\text{-}corr.}}$ vs. RHE > |-0.5 V|). This can be attributed to the different diameters of the two Cu NP types. Both electrodes were produced with the same catalyst loading, ensuring that the catalyst volume is consistent for both electrodes. However, due to the smaller diameter of the Cu NPs "small", the ratio of surface area to volume is higher compared to the Cu NPs "big". Consequently, the electrode with the Cu NPs "small" exhibits a larger total catalyst surface area. Since the surface of the catalyst is the key area of the cat-

alytic reaction, the Cu NPs "small" demonstrate higher activity. Therefore, the same applied potential leads to a higher negative current density for the Cu NPs "small" or vice versa, the same applied current density would result in a lower overpotential.

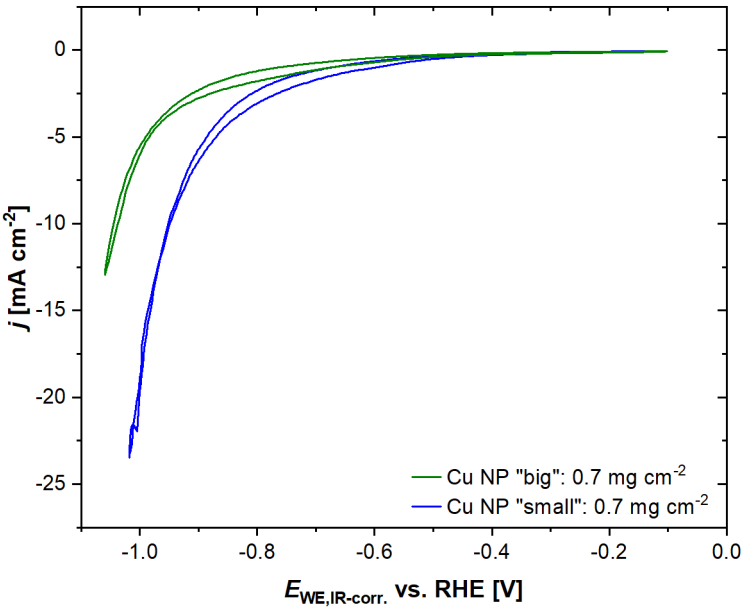

Figure 35: CV curves using two different types of Cu NPs as catalyst with Nafion as binder and a catalyst loading of 0.7 mg cm^{-2} on glassy carbon: Cu NPs "big" are depicted in green and Cu NPs "small" in blue. The measurements are performed in a potential range from -0.1 V to -1.1 V vs. RHE prior to the IR correction with a scan rate of 20 mV s^{-1}. The experiments are conducted in the H-type electrolyzer using a 0.1 M $KHCO_3$ electrolyte.

When applying the same current density of -10 mA cm^{-2} to the electrode with the Cu NPs "small", there is a lower overpotential at the WE (see figure 36a), as was to be expected from the CV curves. Furthermore, the *FE* of H_2 decreases to 36 %, while the *FE* of CO slightly increases to 3 % (see figure 36b). Notably, ethylene becomes more favored over methane compared to the Cu NPs "big". Additionally, the formation of methanol is no longer detectable for the Cu NPs "small", and the *FE* of formate increases to 23 %. These differences stem from the lower overpotential observed at the WE when using the Cu NPs "small" under the same current density conditions (compare with figure 3). However, the most significant distinction in the performance of the two types of Cu NP lies in their durability. The performance of the Cu NPs "small" remains comparatively stable, whereas for the Cu NPs "big", the *FE* of H_2 almost doubles over the measurement time. This is further reflected in the smaller increase in negative potential observed over time for the Cu NPs "small" (compare figure 34a and figure 36a).

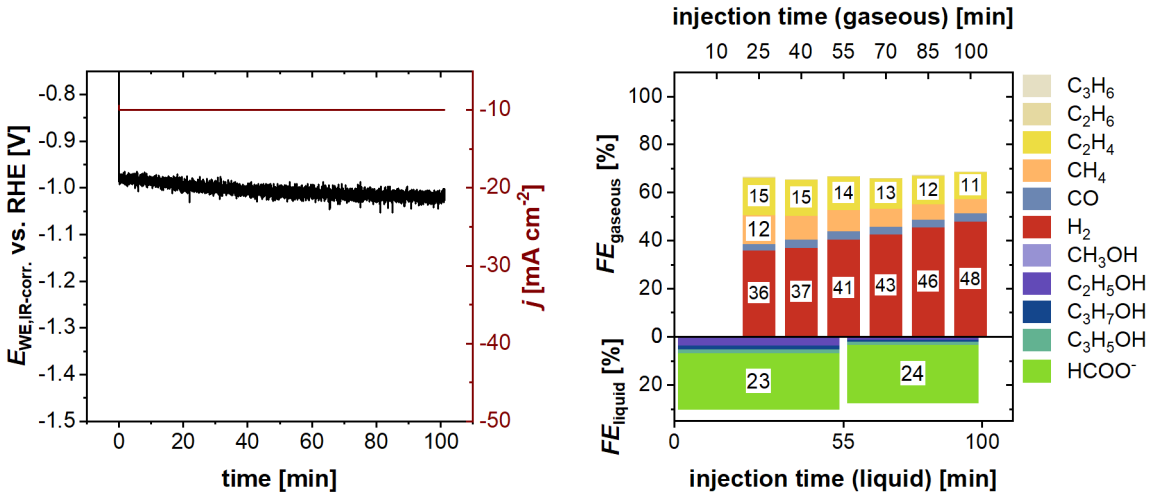

(a) (b)

Figure 36: CO_2RR at a constant current density of -10 mA cm^{-2} using Cu NPs "small" as catalyst with Nafion as binder and a catalyst loading of 0.7 mg cm^{-2} on glassy carbon: (a) plot of the applied current density and the resulting potential at the WE, (b) graph with the calculated *FE*s time-resolved. The experiment is conducted in the H-type electrolyzer using a 0.1 M $KHCO_3$ electrolyte.

For a more comprehensive comparison, the Cu NPs "small" are additionally tested under similar potential conditions as the Cu NPs "big". Based on the data obtained from the CV measurement (see figure 35), a current density of -20 mA cm^{-2} is chosen (see figure 37a). Although the applied potential is now comparable for both electrodes, the *FE* of H_2 slightly decreases to 33 %, while significantly increases for ethylene to 18 %. Moreover, the *FE*s of the liquid products also experiences an increase to some extent. Only the *FE*s of methane and CO remain unchanged. Under the new potential conditions, the Cu NPs "small" also demonstrate a deterioration in performance over time. However, the *FE* of H_2 only increases to 56 %.

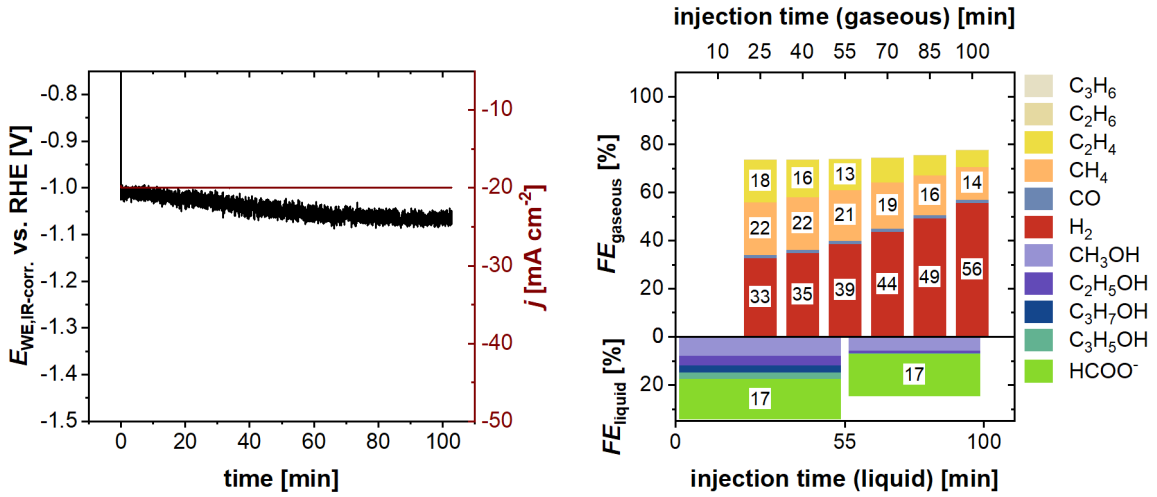

(a) (b)

Figure 37: CO_2RR at a constant current density of -20 mA cm^{-2} using Cu NPs "small" as catalyst with Nafion as binder and a catalyst loading of 0.7 mg cm^{-2} on glassy carbon: (a) plot of the applied current density and the resulting potential at the WE, (b) graph with the calculated *FE*s time-resolved. The experiment is conducted in the H-type electrolyzer using a 0.1 M $KHCO_3$ electrolyte.

To summarize, it can be concluded that the activity of a copper-based electrode tested in an H-type electrolyzer should not be excessively high. Otherwise, the potential required for the formation of C_{2+} products cannot be provided before reaching the limiting current density of the system, resulting in increased H_2 production. When comparing the two tested types of Cu NPs, it can be observed that the Cu NPs "small" exhibit greater activity than the Cu NPs "big", resulting in a lower overpotential at the WE under the same applied current density. This difference in overpotential explains the deviations in the *FE*s of the CO_2RR products observed at identical current densities. In addition, at -10 mA cm^{-2}, a strong deterioration in performance is evident for the Cu NPs "big", while the performance of the Cu NPs "small" remains relatively stable. Nonetheless, when subjected to the same overpotential as the Cu NPs "big", a decline over time in performance is also discernible for the Cu NPs "small", albeit less pronounced. Moreover, concerning the *FE*s, it can be summarized that the Cu NPs "big" show inferior performance in CO_2RR than the Cu NPs "small" under comparable potential conditions.

The next step is to prepare GDEs with the same two Cu NP types and testing them in the static liquid-phase electrolyzer "FlexCell". Subsequently, the obtained data will be compared with the results obtained from the H-type electrolyzer.

4.3.1.2 Performance of Cu NPs in Static Liquid-Phase Electrolyzer

For the preparation of the GDEs, the higher catalyst loading of 2 mg cm^{-2} is used, as the implementation of a GDE overcomes the mass transport limitations of CO_2 by shortening the diffusion path (see section 2.3.2). In addition, a certain catalyst loading is necessary to prevent the GDL from participating in the reaction (see section 4.3.2.2). Prior to conducting the CO_2RR experiments, CV measurements are performed of both Cu NP types (see figure 38). The CV curve of the Cu NPs "small" again displays higher negative values for the current densities than that of the Cu NPs "big" when the same potential is applied (valid for $E_{\text{WE,IR-corr.}}$ vs. RHE > |-0.4 V|). However, this difference is far less pronounced than in the H-type electrolyzer, resulting in only a slightly higher activity of the electrode with the Cu NPs "small" compared to the electrode with the Cu NPs "big".

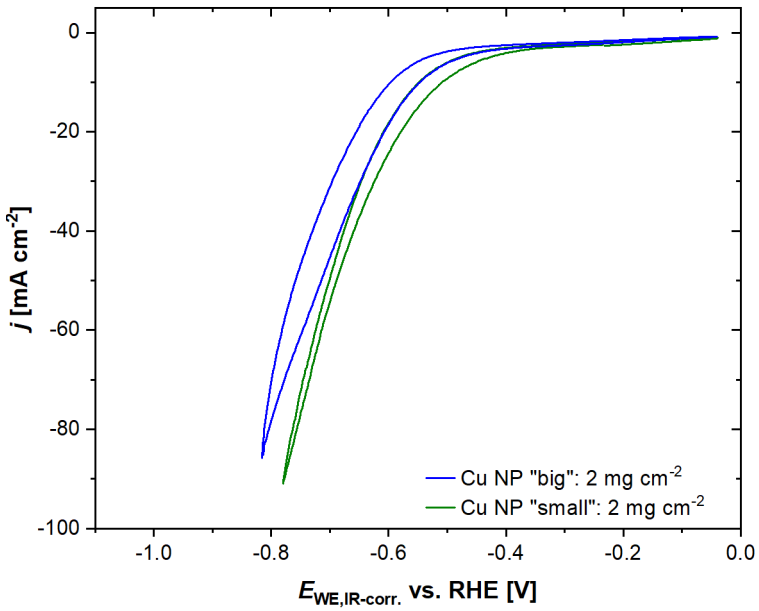

Figure 38: CV curves using two different types of Cu NPs as catalyst with Nafion as binder and a catalyst loading of 2 mg cm^{-2} on a GDL: Cu NPs "big" are depicted in green and Cu NPs "small" in blue. The measurements are performed in a potential range from -0.1 V to -1.1 V vs. RHE prior to the IR correction with a scan rate of 20 mV s^{-1}. The experiments are conducted in the static liquid-phase electrolyzer "FlexCell" using a 1 M $KHCO_3$ catholyte.

Both Cu NP types are tested at a current of -300 mA, which corresponds to a current density of around -100 mA cm^{-2} considering the geometric surface of the WE, which is 3 cm^2. At the start of both measurements, the resulting potential is approximately the same for both electrodes, namely around -0.85 V vs. RHE, which is due to their similar activities (see figure 39a and figure 39c). Because of limitations in the cell setup,

a higher negative current density cannot be applied to achieve a more negative potential, as the catholyte is not circulated and would therefore overheat with increased current input. The data shows a stable potential for the Cu NPs "small" throughout the measurement time. In contrast, the negative potential for the Cu NPs "big" significantly increases to around -1.05 V vs RHE. Based on the knowledge gained from the H-type electrolyzer experiments, it indicates that the performance of the Cu NPs "small" remains stable, while that of the Cu NPs "big" deteriorates. To validate this, the *FE*s from the measurements are considered next. Before delving into the data, a brief note on the structure of the graph is necessary. The appearance of the graph differs from those in which the data from the H-type electrolyzer experiments are presented. This is because, in the FlexCell, gaseous products can be released at two locations within the cell: on the gas side and on the catholyte side. As the two gas streams cannot be analyzed simultaneously, they are detected alternately instead (see section 3.3.3). This allows each stream to be analyzed only every 20 minutes. Now, regarding the data: Initially, the *FE* of the parasitically formed H_2 is around 20 % for the Cu NPs "big", which is lower than the 35 % for the Cu NPs "small". Concurrently, the *FE*s of the CO_2RR products CO and ethylene are smaller for the Cu NPs "small" ($FE = 16$ % respectively $FE = 7$ %) than for the Cu NPs "big" ($FE = 25$ % respectively $FE = 15$ %). In contrast, the *FE*s of the liquid products are comparable for both Cu NP types. In addition, neither type of the Cu NPs forms significant quantities of methane or methanol under these conditions, likely due to the insufficiently negative potential applied to the WEs. The data from the start of the measurement thus indicate a better CO_2RR performance for the Cu NPs "big" than for the Cu NPs "small". However, over time, the performance of the Cu NPs "small" slightly improves, while the performance of the Cu NPs "big" deteriorates drastically, as predicted from the measured potential. More precisely, the *FE* of H_2 for the Cu NPs "big" is tripled over the measurement time. Furthermore, it can be observed that the gaseous products for the Cu NPs "small" are released almost exclusively on the gas side, while for the Cu NPs "big" H_2 with a *FE* of around 10 % is detected in the catholyte towards the end of the measurement.

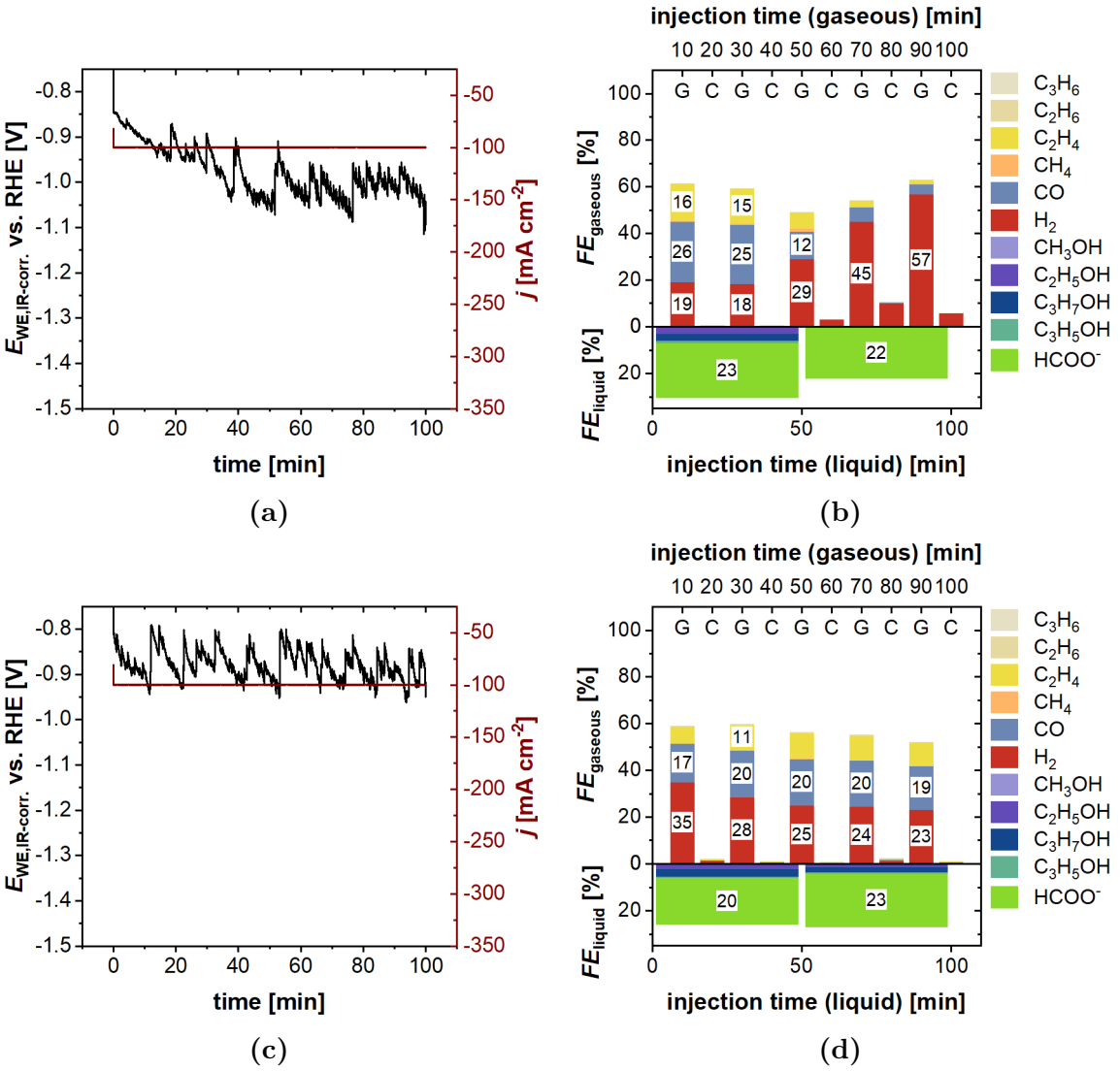

Figure 39: CO_2RRs at a constant current density of -100 mA cm^{-2} using two types of Cu NPs as catalyst with Nafion as binder and a catalyst loading of 2 mg cm^{-2} on a GDL: (a,c) plot of the applied current density and the resulting potential at the WE using the Cu NPs "big" in (a) and the Cu NPs "small" in (c); (b,d) graph with the calculated *FE*s time resolved using the Cu NPs "big" in (b) and the Cu NPs "small" in (d) (G: gas side, C: catholyte side). The experiments are conducted in the static liquid-phase electrolyzer "FlexCell" using a 1 M $KHCO_3$ catholyte.

Finally, the data obtained from both the H-type electrolyzer and the static liquid-phase electrolyzer "FlexCell" are compared to evaluate the transferability of results between the two systems. Several distinctions are apparent: Firstly, the difference in activity between the "big" and "small" Cu NPs, evident in the H-type electrolyzer, is substantially diminished in the FlexCell system. This indicates a different involvement

of the catalyst in the reduction reaction within the two cell systems. In addition, the occurrence of parasitic H_2 formation is less pronounced in the GDE setup, likely attributed to improved CO_2 accessibility to the catalyst. However, the most notable difference lies in the product formation of the CO_2RR. Methane and methanol, significant products of the CO_2RR in the H-type electrolyzer, are barely detectable in FlexCell experiments. Conversely, CO formation significantly increases in the FlexCell setup. Given that product formation using Cu catalysts is highly dependent on the potential at the WE, it is important to note that the overpotential at the WE was significantly higher in the H-type electrolyzer experiments compared to those using the FlexCell. Considering this, the observed differences in the product formation are align with literature data[22], and are most likely not solely attributed to the use of different cell setups, but also to the different potentials. These measurements consequently show that it is essential to know the respective potential at the WE when comparing data from different cell systems to be able to state whether the differences in product formation are due to the systems themselves or to possible different potentials. Beside this, the instability of the Cu NPs "big" observed in the H-type electrolyzer is also found in the FlexCell system, which make this a transferable results between the two systems.

4.3.2 Investigation of CuAg NPls in FlexCell

After using commercial Cu NPs to gain an initial impression of how comparable the data obtained in the H-type electrolyzer and the FlexCell are, the transfer of the self-made CuAg NPls to a GDE is investigated below. For this purpose, the catalyst synthesis is first modified and a GDE produced. Subsequently, its performance in the CO_2RR is investigated and improved. Finally, experiments solely with Ag NPls are discussed as a source of inspiration for future work based on this thesis.

4.3.2.1 Modification of Synthesis and Manufacturing of GDE

In order to use the CuAg NPls for a GDE, it is first necessary to modify their synthesis. One reason for this is that the geometric surface area of the FlexCell is more than six times larger than that of the H-type electrolyzer, so that larger quantities of the catalyst are required. In addition, the catalyst for the H-type electrolyzer was grown on Ag foil, which is not suitable for the preparation of a GDE. To produce the GDE, the CuAg NPls are needed as a powder. To fulfill these two requirements, the catalyst is synthesized in solution (see section 3.3.1). By changing the volume of the synthesis solutions, different amounts of the catalyst can be obtained. In this work, volumes of 100 mL were used for the synthesis, so that around 30 GDEs can be prepared with the same catalyst powder. Furthermore, the Ag NPls are grown for 4 hours in the oven to achieve a reaction yield of around 80 %.

To confirm that the synthesis modification did not change the appearance of the CuAg NPls, SEM images of the catalyst from both synthesis methods are compared

(see figure 40a-b). The SEM images confirm that the catalyst grown in solution has a similar appearance as the catalyst grown on Ag foil. Consequently, the catalyst powder is suitable for the next step, namely the production of a GDE. For this, the Sigracet 28 BC, known from the literature,[93–95] is used as GDL and Nafion as the binder, similar to the procedure with the commercial Cu NPs. Furthermore, a catalyst loading of 1.4 mg cm^{-2} and a binder loading of 10 %, based on the weight of the catalyst, are applied (see section 3.3.2). In figure 40c, a cross-section image of the prepared GDE is shown. The first two layers, from the bottom up, are the macroporous and microporous layers of the GDL. The catalyst layer, consisting of the CuAg NPls, is visible on top. Thus, it can be concluded that the manufacturing part of a GDE using the CuAg NPls as catalyst was successful.

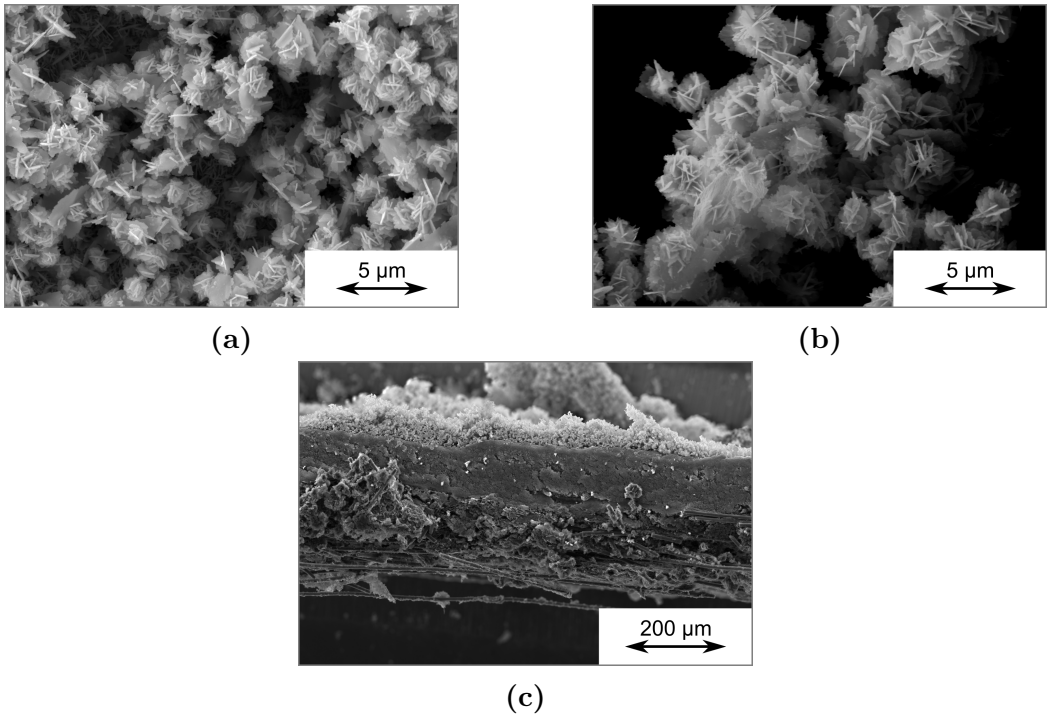

Figure 40: SEM images of the CuAg NPls (a) grown on Ag foil and (b) grown in solution. Additionally, a cross-section image of a GDE prepared with the CuAg NPls grown in solution is shown in (c).

4.3.2.2 Catalytic Performance in CO_2RR

Following the successful manufacturing of a GDE using the CuAg NPls as catalyst (Cu content[EDX] ≈ 5 %), its performance is tested in the CO_2RR at a current density of -100 mA cm^{-2}. The only products formed by this GDE are H_2 (FE = 25 - 50 %), CO (FE = 64 - 38 %), and a small amount of formate (FE = 7 - 4 %) (see figure 41a). These are typical products for a Ag catalyst.[13] However, despite the presence of Cu in the catalyst, its properties are not detectable. A possible explanation for this observation is that Nafion corrodes the Cu deposited on the Ag NPls due to its acidity.

Since the deposited Cu is not present as a bulk phase – the Cu phase cannot even be seen with high resolution transmission electron microscopy – the Cu properties have almost completely vanished due to the Nafion. To test this hypothesis, a GDE is prepared in which the deposited Cu is replaced by adding commercial Cu NPs (diameter range = 20 - 50 nm). With the Cu NPs, more Cu is present in the catalyst layer, which should prevent the complete corrosion of Cu by Nafion and thereby enabling Cu properties to be detectable.

Using the modified GDE, as before, only H_2, CO, and formate are produced (see figure 41b). However, the *FE* of the produced formate is drastically increased from less than 10 % to more than 20 %. Since the Ag structure is the same in both experiments, the increased *FE* of formate is likely caused by the Cu NPs, confirming the above mentioned hypothesis. This can also be supported by the fact that in the study on the pure Ag NPls, the *FE* for formate was always less than 20 %.[79]

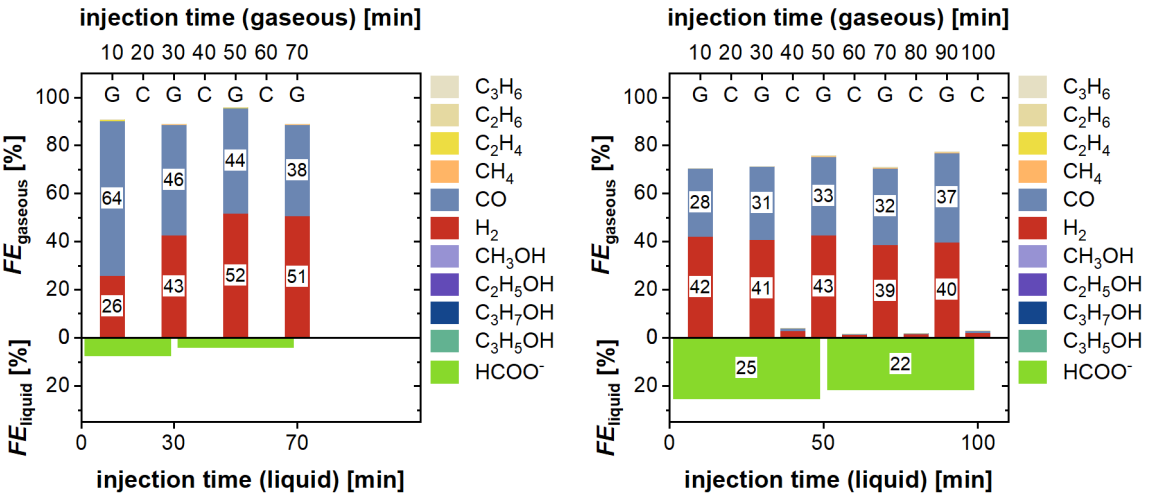

(a) **(b)**

Figure 41: CO_2RRs using (a) CuAg NPls as catalyst with Nafion as binder and a catalyst loading of 1.4 mg cm^{-2} on a GDL [12] and (b) Ag NPls added with commercial Cu NPs as catalyst with Nafion as binder and a catalyst loading of 1.4 mg cm^{-2} on a GDL. The experiments are conducted at a constant current density of -100 mA cm^{-2} in the static liquid-phase electrolyzer "FlexCell", using a 1 M $KHCO_3$ catholyte and a CO_2 gas flow of 20 mL_n min^{-1}. Note: The experiment in (a) is only performed for 70 minutes and the liquid samples are taken after 30 and 70 minutes.

It can therefore be stated that the properties of Cu can be activated by replacing the deposited Cu with commercial Cu NPs. However, formate is not the target molecule for the CO_2RR on Cu-based electrodes, as it can be produced much more selectively with catalysts like Sn or Bi (see figure 1). This raises the question of why only formate is produced and how this can be changed. As indicated in the literature, the formation

of formate requires a lower overpotential at the WE compared to other products like ethylene and ethanol (see figure 3). Thus, a possible explanation for the exclusive production of formate is that the applied overpotential is not high enough to form other products in significant amounts. This hypothesis is supported by the data from the CP measurement (see figure 42a), which shows that the potential at the WE ranges only between -0.8 V and -0.9 V during the measurement. To produce other products besides formate, thus, the overpotential needs to be increased as already observed in the H-type electrolyzer experiments (see figure 31). This can be achieved through two approaches: decreasing the activity of the electrode or increasing the current density. The first approach involves lowering the catalyst loading from 1.4 mg cm^{-2} to 0.7 mg cm^{-2}. As can be seen in the CV curves, with the lower catalyst loading, applying the same potential results in a lower negative current density (valid for $E_{\mathrm{WE,IR\text{-}corr.}}$ vs. RHE > |-0.5 V|), which corresponds to the desired lower activity (see figure 42b).

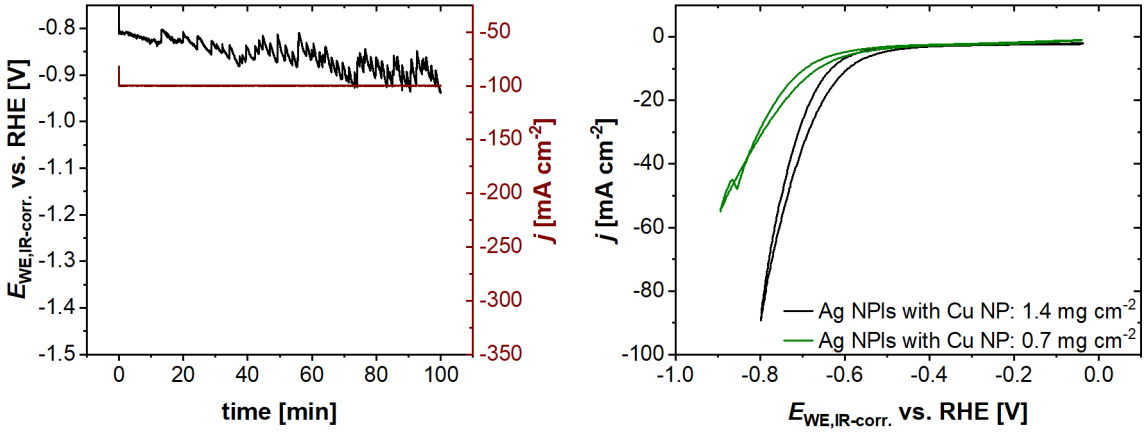

Figure 42: (a) Plot of the applied current density (-100 mA cm^{-2}) and the resulting potential at the WE using Ag NPls added with commercial Cu NPs as catalyst with Nafion as binder and a catalyst loading of 1.4 mg cm^{-2} on a GDL. (b) CV curves using the Ag NPls added with commercial Cu NPs as catalyst with Nafion as binder and two different catalyst loadings on a GDL: 1.4 mg cm^{-2} is depicted in black and 0.7 mg cm^{-2} in green. The experiments are conducted in the static liquid-phase electrolyzer "Flex-Cell" using a 1 M $KHCO_3$ catholyte and a CO_2 gas flow of 20 mL_n min^{-1}.

As was to be expected from the CV curves, the measurement with the smaller catalyst loading starts as intended with a more negative potential, namely -1.0 V, when applying the same current density of -100 mA cm^{-2} (see figure 43a). However, the negative potential decreases during the measurement time to around -0.9 V. Furthermore, the noise in the measured potential is much more pronounced than in the previous measurements. An explanation for this can be found in the calculated *FE*s (see figure 43b): Around 50 % of the *FE* is related to H_2 formed on the catholyte side. H_2

released to the catholyte creates gas bubbles between WE and the RE, which cause the stronger noise in the measured potential.

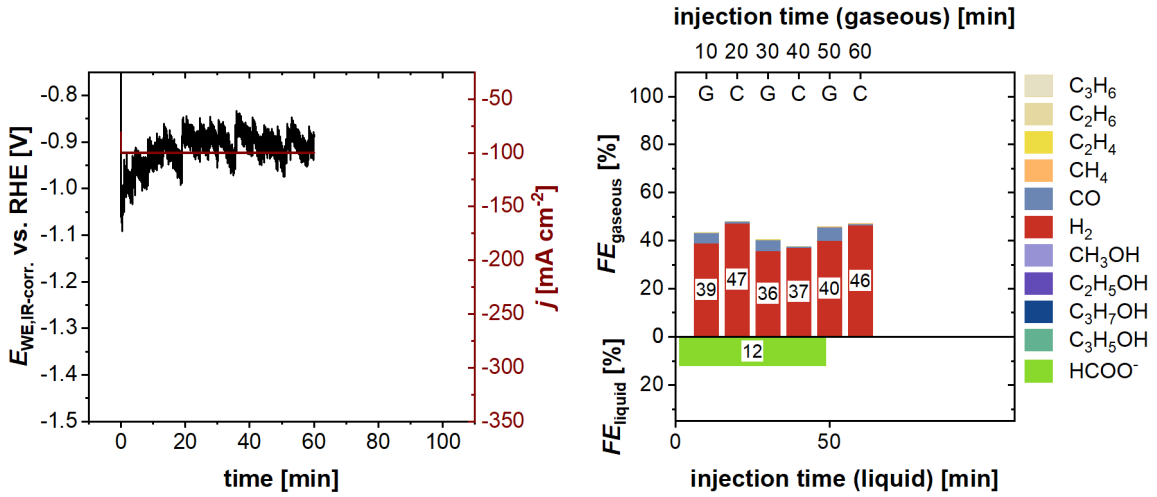

(a) (b)

Figure 43: CO_2RR at a constant current density of -100 mA cm^{-2} using Ag NPls added with commercial Cu NPs as catalyst with Nafion as binder and a catalyst loading of 0.7 mg cm^{-2} on a GDL: (a) plot of the applied current density and the resulting potential at the WE, (b) graph with the calculated *FE*s time-resolved. The experiment is conducted in the static liquid-phase electrolyzer "FlexCell" using a 1 M $KHCO_3$ catholyte and a CO_2 gas flow of 20 mL$_n$ min^{-1}. Note: The experiment ends already after 60 minutes. Still, for better visual comparison with other experiments, the same axis excerpt is shown.

Beyond that, when using the GDE with the lower catalyst loading, hardly any CO_2RR takes place – only CO and formate are produced with a total *FE* of around 15 % – but mainly the parasitic H_2 evolution occurs (*FE* = 85 %) (see figure 43b). A possible explanation for this could be that due to the lower catalyst loading, the reaction mainly takes place at the microporous layer of the GDL and not at the catalyst layer. In order to verify this hypothesis, it is tested whether similar results in terms of *FE* and potential are achieved when using a pure GDL as GDE at the same current density as for the GDE with the lower catalyst loading (see figure 44). In fact, the pure GDL produces almost exclusively H_2 – the only other product is formate with a *FE* of around 1 % – and the resulting potential is the same for both experiments. The only difference is that with the pure GDL, significantly less noise is visible in the measured potential, which is related to the fact that no gaseous products are formed on the catholyte side. The experiment with the GDL thus confirms the above-mentioned hypothesis that when using the GDE with the lower catalyst loading, the reaction mainly takes place at the microporous layer of the GDL and only to a small extent at the catalyst layer. It must therefore be concluded that the approach of diminishing

the activity of the GDE by lowering the catalyst loading in order to achieve a higher overpotential is not possible in this case. Thus, the second approach is tested below.

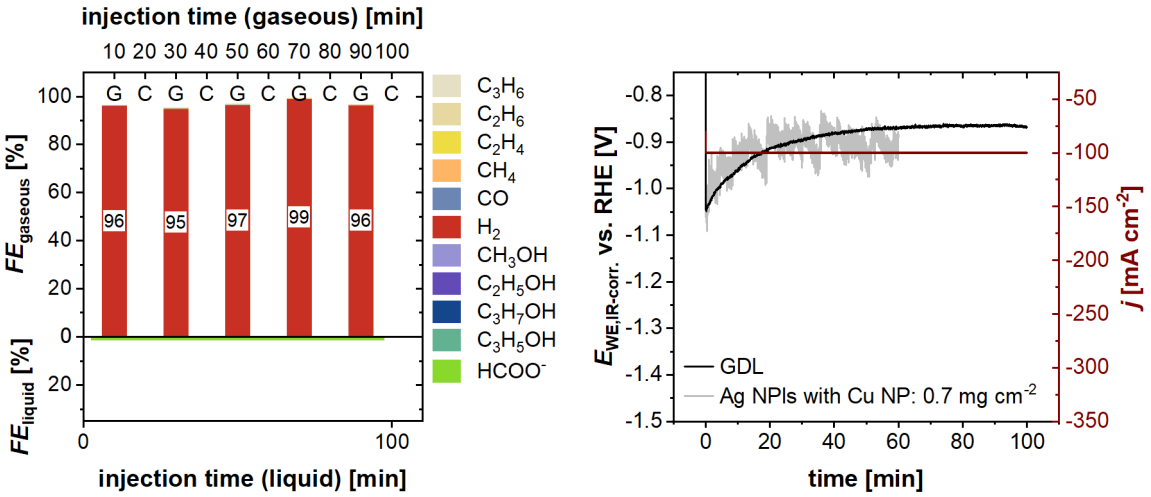

(a) (b)

Figure 44: CO_2RR at a constant current density of -100 mA cm^{-2} using solely a GDL as GDE: (a) graph with the calculated *FE*s time-resolved, (b) plot of the applied current density and the resulting potential at the WE. For easier comparison, the resulting potential of the measurement of figure 43 is also shown. The experiment is conducted in the in the static liquid-phase electrolyzer "FlexCell" using a 1 M $KHCO_3$ catholyte and a CO_2 gas flow of 20 mL$_n$ min^{-1}.

The second approach is to increase the current density in order to achieve a higher overpotential. The simplest way to accomplish this is by increasing the applied current. However, as previously mentioned in section 4.3.1.2, this is not feasible with the used FlexCell, since the catholyte in the cell is not circulated and would heat up due to the higher current input. To address this issue, the static FlexCell is modified into a flow cell. Here, a peristaltic pump and a water-cooled catholyte reservoir with a capacity of 100 mL are used to invoke circulations of the catholyte (see section 3.3.3). This modification allows the dissipation of the additional heat generated by the increased current input. Consequently, it is possible to conduct the CO_2RR experiment at a current density three times higher, namely at -300 mA cm^{-2} (see figure 45a). The increased current density, as intended, leads to a higher negative potential of around -1.1 V vs. RHE at the WE. At these conditions, the measured potential exhibits a noise of around 400 mV, which is even greater than in figure 43a. The noise is again caused by gas bubbles resulting from the evolution of gaseous products in the catholyte (see figure 45b). The amplification of the noise at -300 mA cm^{-2} can be explained by the fact that the same *FE* at a higher current density corresponds to a larger amount of gaseous products released in the catholyte, which leads to more gas bubbles and noise.

Looking at the *FE*s (figure 45b), it can be seen that the primary product is again the parasitic H_2 with an initial *FE* of around 65 % and almost 100 % by the end of the measurement. The most dominant CO_2RR products formed at the beginning of the measurement are CO with a *FE* of around 13 % and formate with a *FE* of 11 %. In addition, ethylene, ethanol, and propanol are formed, each with a *FE* of 1 to 2 %. Although these amounts are small, they demonstrate that a higher overpotential enables the formation of CO_2RR products other than CO and formate. However, it remains unclear why such a large amount of H_2 is formed. An observation during the measurement provides a clue: after 60 minutes, the catholyte can be seen penetrating through the GDE into the gas chamber of the cell, indicating flooding of the GDE. This flooding blocks the pathways for CO_2 to reach the catalyst layer, causing the reduction of water (H_2O) to H_2. Simultaneously, the pathways for the gaseous products to return to the gas side are also blocked by the flooding, explaining why most gaseous products are released on the catholyte side. However, dominant H_2 formation occurs even before minute 60, indicating that there is already a shortage of CO_2 at the catalyst layer in the first half of the measurement. To address this issue, the CO_2 gas supply will be increased from 20 $mL_n\,min^{-1}$ to 60 $mL_n\,min^{-1}$ for the next experiment to enhance CO_2 accessibility at the catalyst layer. All other parameters will remain constant.

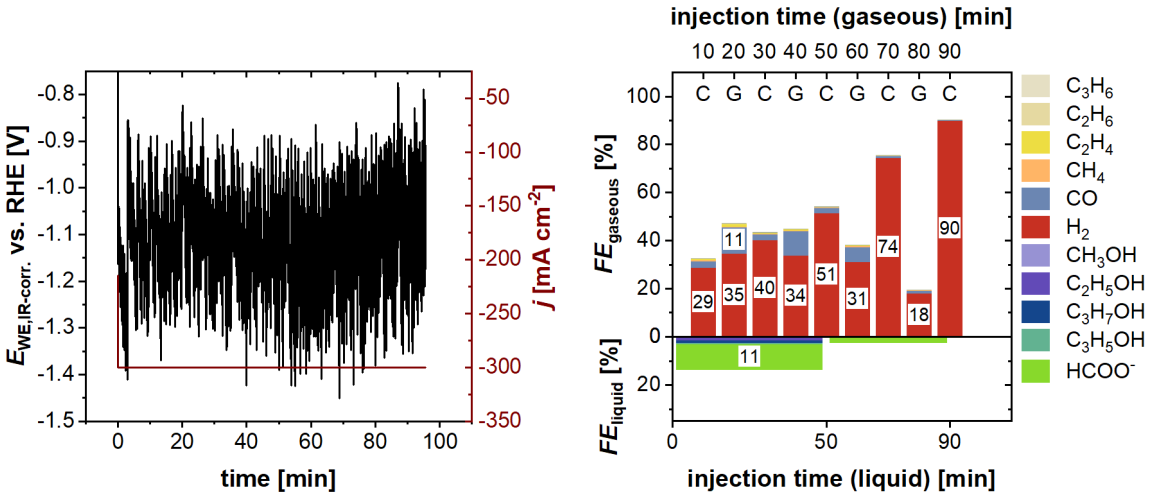

Figure 45: CO_2RR at a constant current density of -300 mA cm^{-2} using Ag NPls added with commercial Cu NPs as catalyst with Nafion as binder and a catalyst loading of 1.4 mg cm^{-2} on a GDL: (a) plot of the applied current density and the resulting potential at the WE, (b) graph with the calculated *FE*s time-resolved. The experiment is conducted in the liquid-phase electrolyzer "FlexCell", which is modified to a flow cell, using a 1 M $KHCO_3$ catholyte and a CO_2 gas flow of 20 $mL_n\,min^{-1}$. Note: The experiment ends already after 90 minutes and the gas injections are started on the catholyte side instead of the gas side.

Indeed, increasing the CO_2 gas supply substantially diminishes the release of gaseous products in the catholyte, indicating unimpeded pathways for the gaseous products to exit to the gas side of the cell (see figure 46). Additionally, the *FE* of H_2 starts at approximately 45 % at the beginning of the measurement and increases to around 55 % by the end, a significant improvement compared to the previous measurement with 20 $mL_n\,min^{-1}$ CO_2 gas supply. Concurrently, the *FE* of CO rises to around 30 %, while the *FE* of formate increases to 25 %. Furthermore, the *FE* of ethylene increases in the course of the measurement to around 5 %. Moreover, in the second half of the measurement, the *FE* of formate diminishes, accompanied by a notable increase in the cumulative *FE*s of alcohols, surpassing 6 %.

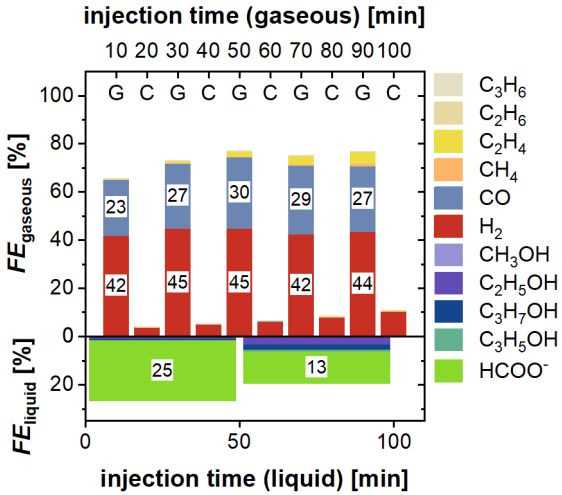

Figure 46: Time-resolved *FE*s of a CO_2RR with a constant current density of -300 $mA\,cm^{-2}$ using Ag NPls added with commercial Cu NPs as catalyst with Nafion as binder and a catalyst loading of 1.4 $mg\,cm^{-2}$ on a GDL. The experiment is conducted in the in the liquid-phase electrolyzer "Flex-Cell", which is modified to a flow cell, using a 1 M $KHCO_3$ catholyte and a CO_2 gas flow of 60 $mL_n\,min^{-1}$.

Summarizing the shown results presented in figure 41 to 46: Testing the CuAg NPls within a GDE at -100 $mA\,cm^{-2}$ showed the exclusive occurrence of products associated with the Ag component of the catalyst and no contributions from the Cu component was present. It was postulated that the acidity of Nafion, capable of corroding the deposited Cu, prevents the presence of Cu properties. To substantiate this, the deposited Cu was substituted with commercial Cu NPs to maximize the presence of Cu, with the idea that the Cu would then no longer be fully corroded by Nafion. In fact, this modification activated the Cu properties of the bimetallic catalyst. However, the initial attempt yielded solely formate production on the Cu parts of the catalyst and no other products such as ethylene, ethanol or propanol. This issue was addressed by applying a higher overpotential at the WE. For this, two approaches were pursued: diminishing electrode activity via decreasing the catalyst loading and increasing the

current density by applying a higher current. The former proved to be unsuitable, as the decreased catalyst loading primarily led to the formation of H_2 within the microporous layer of the GDL. Contrary, increasing the current showed the desired effect of forming ethylene, ethanol, and propanol. Nonetheless, the question still remains whether it is also possible to activate the Cu properties of the CuAg NPls without substituting the deposited Cu with commercial Cu NPs, which is considered below.

The investigation above provides empirical support for the previously mentioned hypothesis that the absence of observable Cu properties when using the CuAg NPls is due to the acidity of Nafion. To address this issue, a less acidic binder, namely Piperion, is tested in the next experiment at the same current density of -100 mA cm^{-2}. As desired, activation of the Cu properties in the CuAg NPls is achieved by using Piperion as binder, evidenced by the formation of ethylene ($FE = 4\,\%$), ethanol ($FE = 3\,\%$), and other alcohols (cumulative $FE = 3\,\%$) at the beginning of the measurement, along with diminished CO formation ($FE = 50\,\%$; sum of gas and catholyte side) (see figure 47a). However, it has to be noted that the formation of the alcohols ceases over the course of the measurement time.

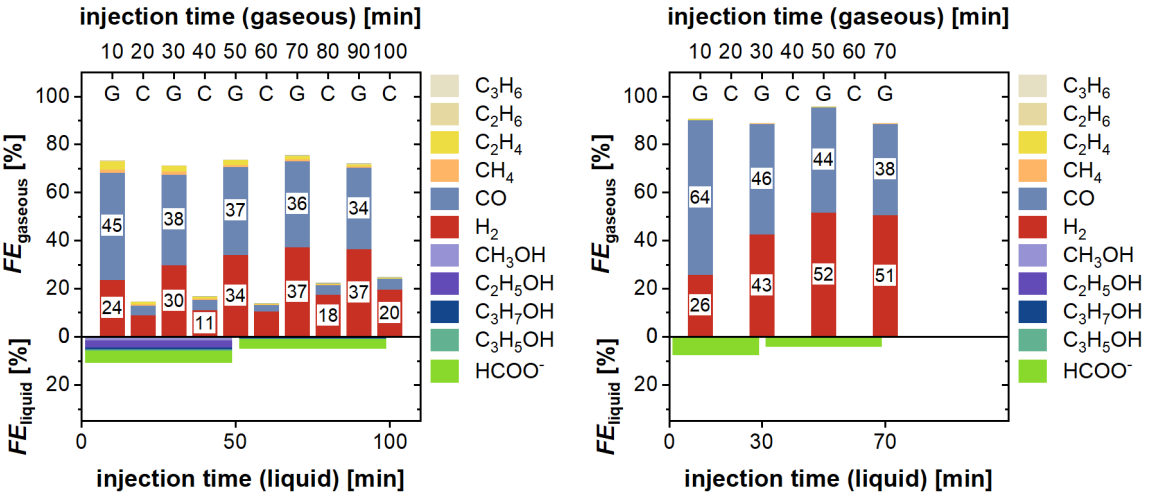

Figure 47: Time-resolved *FE*s of CO_2RRs with a constant current density of -100 mA cm^{-2} using CuAg NPls as catalyst with two different binders and a catalyst loading of 1.4 mg cm^{-2} on a GDL: (a) with Piperion as binder [12], (b) for easier comparison, the graph with Nafion as binder is shown again (compare figure 41a) [12]. The experiments are conducted in the static liquid-phase electrolyzer "FlexCell" using a 1 M $KHCO_3$ catholyte and a CO_2 gas flow of 20 mL_n min^{-1}.

Prior to delving deeper into the question of why the formation of alcohols is absent in the second half of the measurement time, two other points need to be discussed first: the flow rate of the CO_2 gas supply and the use of a new catalyst powder.

The experiment with the Ag NPls combined with commercial Cu NP at an increased CO_2 gas flow of 60 mL_n min^{-1} showed a more consistent measurement of the CO_2 gas flow using the drum-type flow counter. This can be explained by the fact that the previously used flow rate of 20 mL_n min^{-1} is close to the minimum flow rate threshold of this device, which is 17 mL min^{-1}. Therefore, it would be advantageous to use the higher CO_2 gas flow in all subsequent experiments. However, it must first be ensured that the higher CO_2 gas flow has no effect on the results obtained. To verify this, the experiment using the CuAg NPls with Piperion as binder is repeated with a CO_2 gas flow of 60 mL_n min^{-1} instead of 20 mL_n min^{-1} at the same current density of -100 mA cm^{-2}. No discernible change is observed in the acquired data (see figure 48a), allowing all subsequent experiments to be conducted with the heightened CO_2 gas flow of 60 mL_n min^{-1}. Secondly, a new CuAg NPls powder needs to be synthesized as the previously utilized powder has been depleted. Taken SEM images verify that the new CuAg NPls have the same morphology. To further ensure comparability with the previous catalyst powder, the last experiment is repeated with the new catalyst powder and the results are compared (see figure 48b). The obtained data show similar performance for both catalyst powders, allowing the new powder to be used in the following experiments.

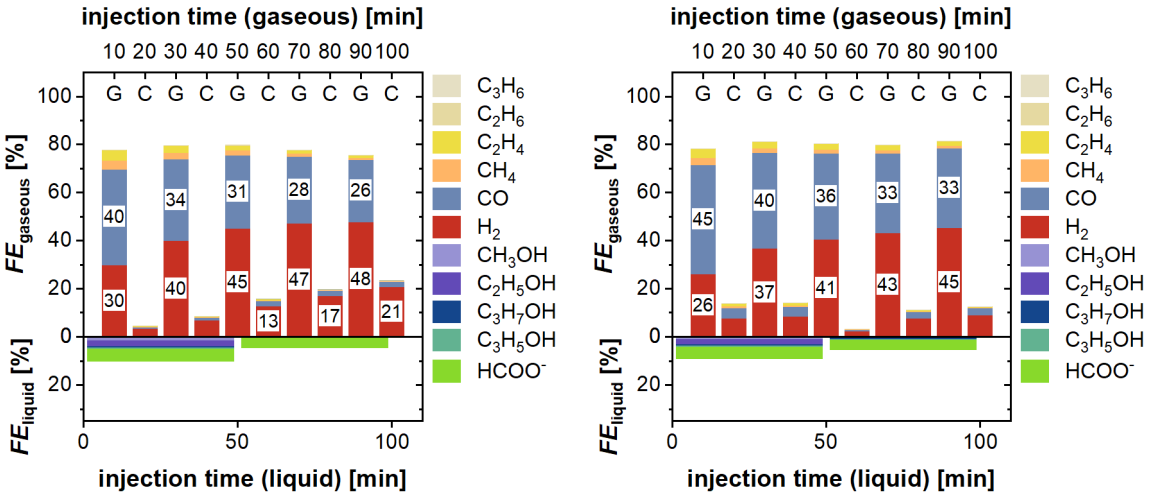

Figure 48: Time-resolved *FE*s of CO_2RRs with a constant current density of -100 mA cm^{-2} using CuAg NPls as catalyst with Piperion as binder and a catalyst loading of 1.4 mg cm^{-2} on a GDL: (a) using an increased CO_2 gas flow of 60 mL_n min^{-1}, (b) using a new CuAg NPls powder with a CO_2 gas flow of 60 mL_n min^{-1}. The experiments are conducted in the static liquid-phase electrolyzer "FlexCell" using a 1 M $KHCO_3$ catholyte.

In the following, the open question regarding the absence of alcohol formation during the second half of the measurement period using CuAg NPls with Piperion at -100 mA cm^{-2} is discussed. A plausible explanation for this phenomenon is that the

further production of the alcohols is hindered due to the sluggish mass transport on the catholyte side of the GDE. To empirically validate this hypothesis, the experimental setup is once again modified from a static cell to a flow cell configuration (see section 3.3.3). This adjustment is based on the assumption that the catholyte circulation enhances the mass transport at the GDE, thereby promoting further alcohol formation. An additional advantage of this modification is the larger catholyte volume in the "flow mode", which enables more frequent liquid sampling and thus a finer temporal resolution of the *FE*s of the liquid products. More precisely, the liquid sampling is conducted after 20, 40, 60, 80, and 100 minutes. When comparing the data sets obtained with and without circulation of the catholyte, the *FE*s of the gaseous products are considered first. Here, an increase in the *FE* of CO is measured, while that of H_2 decreases. However, these differences are only marginal. Considering the *FE*s pertaining to the liquid products, a constant alcohol formation can be observed throughout the entire measurement period, which supports the hypothesis proposed. In addition, it is apparent that the first measured *FE*s for both methanol and ethanol are almost doubled compared to those derived from the static measurement. It is assumed that, initially, the *FE* of both experimental setups is alike. In the course of the experiment, however, it appears that in the static setup, the *FE*s of the alcohols constantly decrease due to their accumulation in the catholyte in vicinity of the catalyst layer. In contrast to that, the modified setup, which involves permanent flow of the catholyte, leads to constant *FE*s with respect to the formation of alcohols. Given that the first measurement point of the static experiment is conducted only after 50 minutes, the derived value does not represent the initial value. Instead, it is an averaged value of the initial 50 minutes of experimental time, thus already including the decrease in *FE* over time. As a consequence, the value is smaller than the initial one of the flow experiment.

To summarize, the use of a less acidic binder, namely Piperion, instead of Nafion activates the Cu properties of the CuAg NPls. In the second half of the measurement, however, the formation of the alcohols ceases. This is attributed to the accumulation of alcohols in the catholyte near the catalyst layer due to the sluggish mass transport at the GDE. It is overcome by changing the experimental setup from a static to a flow cell configuration in which the catholyte is circulated.

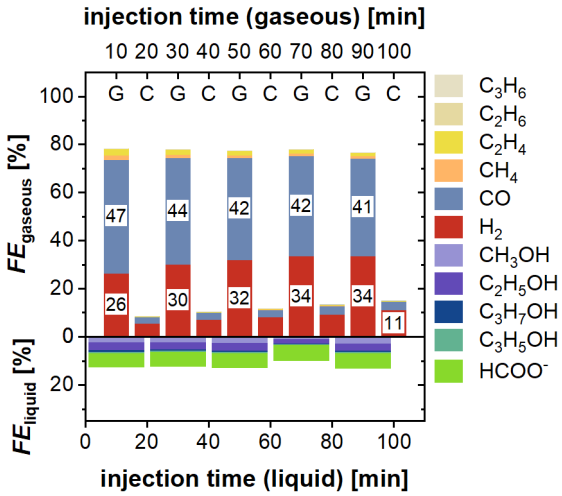

Figure 49: Time-resolved *FE*s of a CO_2RR with a constant current density of -100 mA cm^{-2} using CuAg NPls as catalyst with Piperion as binder and a catalyst loading of 1.4 mg cm^{-2} on a GDL. The experiment is conducted in the liquid-phase electrolyzer "FlexCell", which is modified to a flow cell, using a 1 M $KHCO_3$ catholyte and a CO_2 gas flow of 60 mL$_n$ min^{-1}.

4.3.3 Investigation of Pure Ag NPls – Inspiration for Future Experiments

In addition to the experiments involving CuAg NPls and Ag NPls combined with commercial Cu NPs, experiments solely with Ag NPls are conducted. These experiments are intended to serve as sources of inspiration for future research based on this thesis and not as a completed study. Although the pure Ag NPls do not contain Cu, which could be corroded by Nafion, Piperion is still utilized as binder to maintain consistent conditions. For further comparability, a current density of -100 mA cm^{-2} and a CO_2 flow rate of 60 mL$_n$ min^{-1} is applied once again. As for a pure Ag catalyst only gaseous products are expected to be the primary products – namely CO from the CO_2RR and H_2 from the water reduction – there is no need to use optimized conditions for the formation of liquid products. As a consequence, the experiments are conducted in the more simple static cell setup. Furthermore, no liquid samples are taken.

As anticipated, the main products of the pure Ag NPls are H_2 and CO (see figure 50a). However, the *FE* of H_2 is 2.4 times higher initially and even 7.6 times higher at the end of the measurement compared to that of CO. Such a poor performance of the Ag NPls was not to be expected on the basis of their investigation using an H-type electrolyser.[79] Additionally, it can be observed that approximately half of the *FE* is attributed to the formation of mainly H_2 on the catholyte side. This indicates a lack of CO_2 at the catalyst layer. In previous measurements, an increase in the CO_2 gas flow was found to be effective in decreasing the lack of CO_2. However, since the

current experiment already utilizes an elevated CO_2 gas flow of $60\,mL_n\,min^{-1}$, an alternative approach is pursued: modifying the cell setup into the "pressure mode" (see section 3.3.3). In this mode, initially, a pressure of around 8.5 mbar above ambient pressure is applied to both the catholyte and gas side of the cell. To find the "bubble point" of the system, the pressure on the catholyte side is kept constant, while the pressure on the gas side is gradually increased. The "bubble point" is reached when the CO_2 gas penetrates into the catholyte and causes gas bubbles (see section 2.3.2). This can be identified by a decrease in the gas flow on the gas side, as parts of the CO_2 gas penetrate into the catholyte. The penetrating gas can then be detected by an increased gas flow on the catholyte side. Once this point is reached, the pressure on the gas side is slightly decreased until the gas flows on both the catholyte and gas side return to their initial values. Due to this procedure, the gas/catholyte interface should be situated within the catalyst layer so that the CO_2 gas can easily penetrate into the catalyst layer but without penetrating into the catholyte.

At the beginning of the measurement, the *FE* of gaseous products on the catholyte side can actually be suppressed to less than 20 % (see figure 50b). However, this does not improve the *FE* of CO, which remains at less than 30 %. This suggests that the issue lies not solely in the insufficient accessibility of CO_2 at the catalyst layer, but also in the catalyst layer's inactivity towards the CO_2RR. Additionally, it should be noted that as the measurement progresses, around 50 % of the *FE* is once again attributed to the formation of mainly H_2 on the catholyte side.

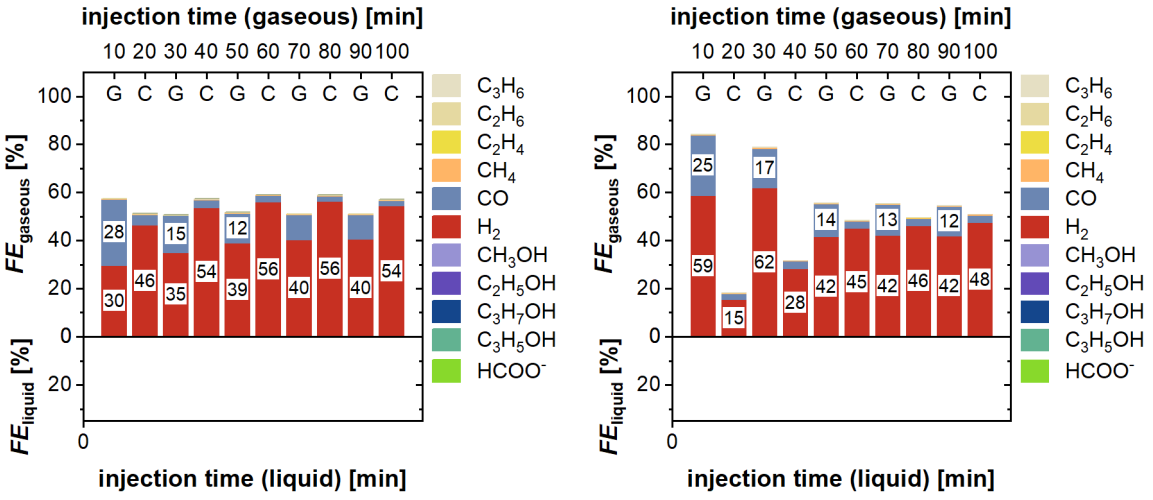

Figure 50: Time-resolved *FE*s of CO_2RRs with a constant current density of -100 mA cm^{-2} using solely the Ag NPls as catalyst with Piperion as binder and a catalyst loading of 1.4 mg cm^{-2} on a GDL: (a) performed in the unmodified static liquid-phase electrolyzer "FlexCell" (b) using the static liquid-phase electrolyzer "FlexCell" modified to the "pressure mode". The experiments are conducted using a 1 M $KHCO_3$ catholyte and a CO_2 gas flow of 60 mL$_n$ min^{-1}. Note: No liquid samples are taken.

In an attempt to activate the catalyst layer for the CO_2RR, a high current is applied to the WE for 5 seconds prior to the CO_2RR. This is conducted first without using the "pressure mode". Initially, a reductive current of -950 mA is tested, but no improvements are observed. Subsequently, using a new electrode, an oxidative current of +950 mA is applied to the WE. This successfully increases the *FE* of CO to approximately 50 % throughout the entire measurement time, indicating enhanced activity of the catalyst layer for the CO_2RR (see figure 51a). However, 40 % of the *FE* still originates from the catholyte side, suggesting insufficient CO_2 availability at the catalyst layer. Hence, it can be assumed that improving the CO_2 accessibility by applying the "pressure mode" could further enhance CO formation. Consequently, both the "pressure mode" and the oxidative current pulse are combined to address both the insufficient accessibility and the inactivity simultaneously. Through this, gaseous product formation on the catholyte side is effectively suppressed to below 5 % (see figure 51b). Additionally, the *FE* of CO is increased to 70 % and concurrently the *FE* of H_2 is decreased to around 30 %.

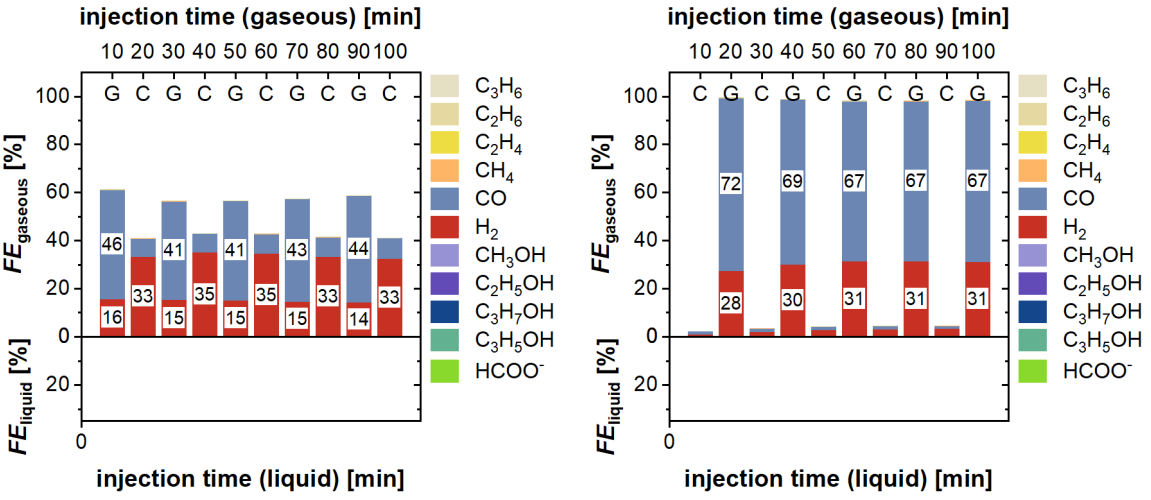

Figure 51: Time-resolved *FE*s of CO_2RRs with a constant current density of -100 mA cm^{-2} using solely the Ag NPls as catalyst with Piperion as binder and a catalyst loading of 1.4 mg cm^{-2} on a GDL: (a) performed with a current pulse of +950 mA prior to the CO_2RR and in the unmodified static liquid-phase electrolyzer "FlexCell" (b) in addtion to (a) the cell is modified to the "pressure mode". The experiments are conducted using a 1 M $KHCO_3$ catholyte and a CO_2 gas flow of 60 mL$_n$ min^{-1}. Note: No liquid samples are taken and the gas injections are started in (b) on the catholyte side instead of the gas side.

These data raise two key questions. First, what occurs during the activation process? And second, why is there an activation required for the Ag NPls in the FlexCell system but not in the H-type electrolyzer? Although these questions cannot be fully answered within the scope of this work, ideas for possible explanations and remaining open questions will be provided as a starting point for further investigations.

Regarding the first question about what occurs during the activation: After the GDE is removed from the cell system at the end of the measurement, it is observed that the catalyst layer has discolored. To investigate whether this discoloration is due to a change in morphology or composition, SEM images are taken and XRD measurements are performed on both GDEs with and without current pulse after the CO_2RR. The comparison of the SEM images clearly shows that the current pulse leads to a change in the morphology of the Ag NPls, specifically resulting in a finer structure on the surface of the Ag NPls (see figure 52). This is also reflected by a higher activity of the GDE with current pulse compared to without current pulse measured after the CO_2RR (see figure 52a). In addition, the comparison of the XRD data shows that the composition did not change, as there are no discernible differences between the Ag peaks of the GDE with or without the current pulse (see figure 52b). However, the reflexes assigned to the GDL differ between the GDEs with and without current

pulse, suggesting that the crystalline structure of the GDL is changed by the current pulse.

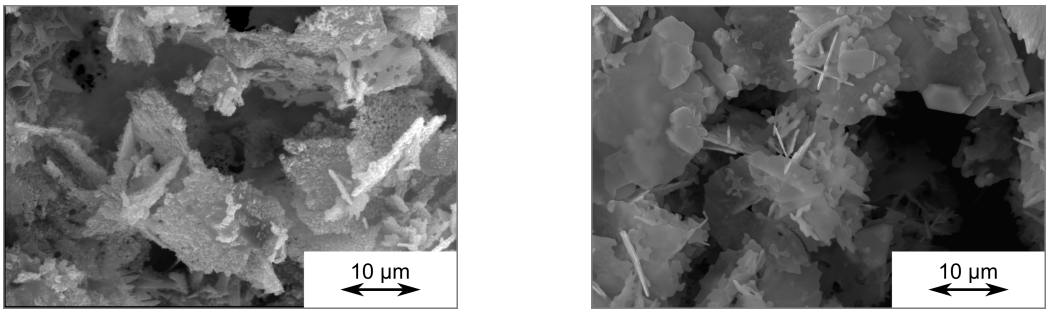

(a) (b)

Figure 52: Top view SEM images of GDEs prepared with Ag NPls as catalyst and Piperion as binder taken after the CO_2RR: (a) with an applied current pulse of +950 mA for 5 s prior to the CO_2RR (b) without a current pulse.

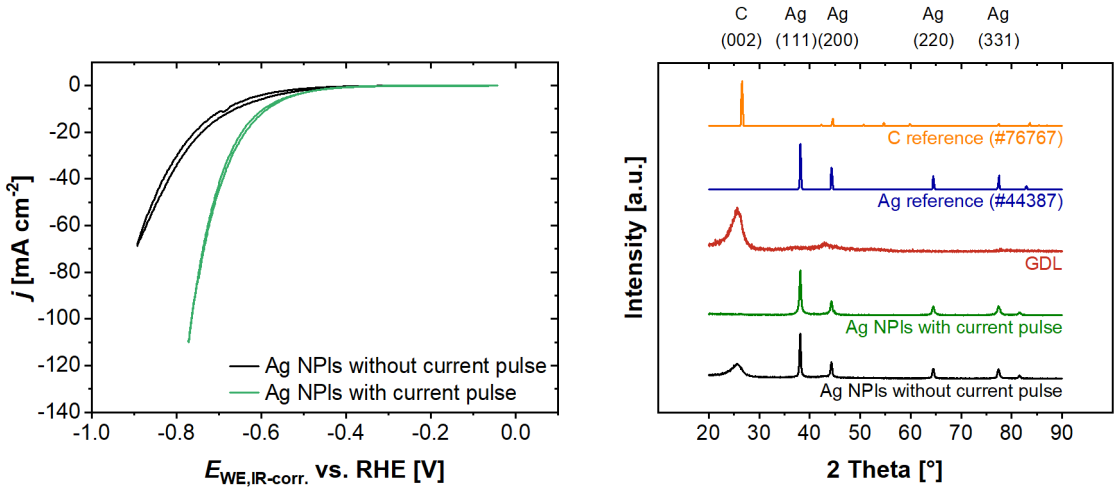

(a) (b)

Figure 53: (a) CV curves and (b) XRD patterns of GDEs using Ag NPls as catalyst with Piperion as binder and a catalyst loading of 1.4 mg cm^{-2}: Data from measurements without an applied current pulse of +950 mA for 5 s prior to the CO_2RR are depicted in black and with in green. The data are acquired after the CO_2RR. In (b), additional XRD patterns of a GDL as well as a Ag and carbon (C) reference pattern from the ICS database are shown.[85]

Regarding the second question, why there is an activation required for the Ag NPls in the FlexCell system but not in the H-type electrolyzer: A possible explanation lies in the different types of electrodes. When using a GDE, the catalyst layer, unlike

the solid electrode in the H-type electrolyzer, has to compete with the activity of the microporous layer (MPL), which has a large surface area. If the activity of the catalyst layer is not sufficiently high compared to the activity of the MPL, the CO_2RR at the catalyst layer occurs only to a small extent, while primarily the water reduction at the MPL takes place, recognizable by a high H_2 evolution. Such a high H_2 evolution of more than 70 % is measured using the original Ag NPls in the FlexCell system. However, when applying the current pulse, the *FE* of H_2 decreases to 50 % or even 30 % if the "pressure mode" is additionally employed (see figure 51). The SEM images and CV curves of the Ag NPls show that their activity is increased by the current pulse. This observation indicates that the original Ag NPls are not sufficiently active compared to the MPL, necessitating the activation of the Ag NPls in the FlexCell system. Since no MPL is present in the electrode used in the H-type electrolyzer, this is not an issue for these experiments, and no activation is needed there.

Interestingly though, both the addition of commercial Cu NPs as well as partial coating with elementary Cu also suppressed the formation of H_2 in the FlexCell experiments, even though no electric pulse was applied in these experiments. This could be explained by the fact that Cu is more active than Ag (see figure 28). As a result, the activity of the catalyst is intrinsically higher, enabling it to compete with the activity of the MPL without the need for activation.

In addition to the different types of electrodes, there are two other differences within the catalyst layer between the one in the H-type electrolyzer and the FlexCell system, which could also account for the measured deviations in the two cell systems. First, unlike in the FlexCell system, the catalyst layer in the H-type electrolyzer does not contain any binder, as the Ag NPls are grown on Ag foil. Secondly, the Ag NPls used in the two cell systems are not exactly the same, since the synthesis had to be modified to enable the incorporation of the Ag NPls into a GDE.

Even though the Ag NPls with Cu show a lower formation of the parasitic H_2 compared to the Ag NPls without activation, it would still be interesting to know if the performance of the CuAg NPls could be improved by using activated Ag NPls. The issue here is that a positive current pulse applied on the CuAg NPls would oxidize the deposited Cu, leaving only the activated Ag NPls without any Cu properties.

As stated at the beginning of this chapter, the investigations of the pure Ag NPls do not represent a completed study. Nevertheless, the following interesting findings can be summarized: When using the pure Ag NPls as catalyst in a GDE, a poor performance was observed, indicated by a *FE* of H_2 higher than 70 %. To understand and improve the performance, it was essential to measure the gas streams from the gas side and the catholyte side independently. This allowed for the observation that around 50 % of electrolysis products were released on the catholyte side, indicating a blockage for gas transfer within the GDL. Thus, also the CO_2 transfer to the catalyst layer was hindered, resulting in insufficient accessibility of CO_2 at the catalyst layer.

Therefore, when a high release of H_2 on the catholyte side is measured, it should be considered that the gas-catholyte interface is not within the catalyst layer and requires readjustment. To achieve this, the "pressure mode" described above can be applied, which enables control of the position of the gas-catholyte interface. Furthermore, it was found that the Ag NPls incorporated in a GDE were not sufficiently active for the CO_2RR. By applying a positive current pulse of 950 mA, the performance was significantly improved. Together with the use of the "pressure mode", a constant *FE* for CO of around 70 % was achieved.

5 Conclusion

In this thesis, the electrochemical CO_2 reduction reaction (CO_2RR) to the value-added product ethanol was investigated ("Power-to-ethanol"). Ethanol was chosen as target molecule, since it can act as pioneer product to enable the near-term feasibility of CO_2RRs.

The first aim of this thesis was to develop a suitable catalyst for the described purpose. As pure Cu electrodes often exhibit insufficient selectivities for C_{2+} products, the alloying approach was utilized for the development of this catalyst. To pursue this approach, a new bimetallic catalyst was synthesized, consisting of silver nanoplates (Ag NPls) partially coated with Cu, referred to as copper-silver nanoplates (CuAg NPls). By varying the duration of the electroless Cu deposition, catalysts with different Cu contents were prepared. A linear relation between their Cu contents measured by EDX and by ICP-MS was found. This relation enabled a non-destructive measurement of the Cu content in the entire catalyst layer. In addition, XPS measurements were conducted to determine the catalytically relevant near-surface copper content.

The electrochemical investigations of this catalyst were conducted using an H-type electrolyzer, a suitable cell design for catalyst development. It was observed that the activity of the catalyst rises with increasing near-surface Cu content. Furthermore, the influence of the Cu content on the performance of the catalyst in the CO_2RR was investigated. It was found that a near-surface Cu-to-Ag ratio of about 50:50 shows the most beneficial interplay of Cu and Ag, resulting in the highest ethanol formation. Concurrently, the parasitic formation of H_2 and the competing ethylene evolution were suppressed. The first objective of this thesis was thus achieved. Afterwards, a comparison of different current densities showed that -20 $mA\,cm^{-2}$ and about -1.0 V vs. RHE are suitable conditions for the developed catalyst and cell design.

The second aim of this thesis was to investigate the transfer of this catalyst into an industrially more relevant cell design utilizing a gas diffusion electrode (GDE). A GDE shortens the diffusion path of CO_2, which overcomes mass transport limitations and thus accelerates the reaction and enables higher current densities. For this purpose, the FlexCell from Gaskatel was employed.

As preliminary work, the performance of two types of commercial copper nanoparticles (Cu NPs) in both the H-type electrolyzer and the FlexCell was compared to gauge the comparability of the data obtained from these two cell designs. Several

distinctions were apparent: Firstly, the difference in activity between the "big" and "small" Cu NPs, evident in the H-type electrolyzer, was substantially diminished in the FlexCell system. This indicated a different involvement of the catalyst in the reduction reaction within the two cell systems. In addition, the occurrence of parasitic H_2 formation was less pronounced in the GDE setup, likely attributed to improved CO_2 accessibility to the catalyst. However, the most notable difference lied in the product formation of the CO_2RR. Methane and methanol, significant products of the CO_2RR in the H-type electrolyzer, were barely detectable in the FlexCell experiments. Conversely, CO formation was significantly increased in the FlexCell setup. This observation could be attributed to the different potentials at the working electrode (WE) in the two cell systems. These measurements consequently showed that it is essential to know the respective potential at the WE when comparing data from different cell systems. This knowledge is necessary to be able to state whether the differences in product formation are due to the systems themselves or to possible different potentials. Beside this, an instability in the performance of the Cu NPs "big" was observed in both electrolysis cells, making this a transferable result between the two systems. As a conclusion, it can be stated that the data obtained in the two cell designs are comparable with regard to the Faradaic efficiency (FE) if the different potentials at the WE in the two cells are taken into account.

To investigate the transfer of the CuAg NPls into the FlexCell system, a modification of the catalyst synthesis was required, because the catalyst was needed in larger quantities and as powder. To fulfill these two requirements, the catalyst was synthesized in solution. Testing the GDE prepared with the CuAg NPls at -100 $mA\,cm^{-2}$ in the FlexCell system showed the exclusive occurrence of products associated with the Ag component of the catalyst. In contrast to expectation, no contributions from the Cu component was present. It was postulated that the acidity of Nafion, capable of corroding the deposited Cu, suppresses the Cu properties. To substantiate this, the deposited Cu was substituted with commercial Cu NPs to maximize the presence of Cu and to prevent corrosion of the entire Cu fraction by Nafion. In fact, this modification activated the Cu properties of the bimetallic catalyst. However, the initial attempt yielded solely formate production on the Cu parts of the catalyst and no other prducts such as ethylene, ethanol or propanol. This issue was addressed by applying a higher overpotential at the WE. For this, two approaches were pursued: diminishing electrode activity via decreasing the catalyst loading and increasing the current density by applying a higher current. The former proved to be unsuitable, as the decreased catalyst loading primarily led to the formation of H_2 within the microporous layer of the GDL. Contrary, increasing the current showed the desired effect of forming ethylene, ethanol, and propanol.

Beyond that, it was also accomplished to activate the Cu properties of the CuAg NPls without substituting the deposited Cu with commercial Cu NPs. For this, a less acidic binder than Nafion was used, namely Piperion. In the second half of the measurement, however, the formation of the alcohols ceased. This could be attributed to the

accumulation of alcohols in the catholyte near the catalyst layer due to the sluggish mass transport at the GDE. By changing the experimental setup from a static cell to a flow cell configuration in which the catholyte was circulated, the alcohol formation could be maintained throughout the entire measurement period.

Still, it is evident that the performance of the CuAg NPls achieved in the H-type electrolyzer could not yet be fully replicated in the FlexCell system. When comparing the results from the two cell systems, it has to be considered that, in addition to the different types of electrodes, there are two further differences in the catalyst layer. Firstly, the CuAg NPls are not exactly the same, as the synthesis had to be modified. Secondly, as the catalyst was grown on Ag foil for the experiments in the H-type electrolyzer, no binder was necessary. However, as seen in the previously mentioned experiments, the binder has a huge influence on the performance of the catalyst. Thus, the comparability of the data obtained in the H-type electrolyzer and in the FlexCell system is much more difficult for the CuAg NPls than for the commercial Cu NPs, for which the catalyst and the binder were exactly the same in both cell systems.

This significant difference in performance using the two cell systems was also observed when investigating the pure Ag NPls as catalyst in a GDE. Here, a *FE* of H_2 higher than 70 % was measured, which was not expected based on the investigation using an H-type electrolyzer. However, by applying a positive current pulse of 950 mA, the performance was significantly improved. The same approach cannot be applied to the CuAg NPls, as the deposited Cu would be oxidized, and only the activated Ag NPls without any Cu properties would remain.

Additionally, another interesting observation was made through these measurements. It was found that around 50 % of the electrolysis products were released on the catholyte side. This was attributed to the blockage for gas transfer within the GDL, which also hinders the CO_2 transfer to the catalyst layer, resulting in insufficient accessibility of CO_2 at the catalyst layer. Therefore, when a high release of H_2 on the catholyte side is measured, it should be considered that the gas-catholyte interface is not within the catalyst layer and requires readjustment. To achieve this, the "pressure-mode" described in this thesis can be applied, which enables control of the position of the gas-catholyte interface. Combining both, the current pulse and the "pressure-mode", a *FE* of CO of around 70 % was achieved.

In brief, using an H-type electrolyzer, a new bimetallic catalyst for the CO_2RR to ethanol was discovered, which suppresses the parasitic H_2 formation and the competitive ethylene evolution. Subsequently, its transfer into an industrially more relevant cell design employing a GDE was investigated. Here, several modifications were applied to activate the catalytic Cu properties of the catalyst and to study different transfer challenges. Thus, suitable optimizations for the CO_2RR to ethanol were found for the most important parameters. Moreover, interesting solutions for fur-

ther investigations were found, such as the activation through a current pulse or the "pressure-mode".

Bibliography

[1] Intergovernmental Panel on Climate Change, "Climate Change 2023: Synthesis Report", **2023**.

[2] S. J. Davis, N. S. Lewis, M. Shaner, S. Aggarwal, D. Arent, I. L. Azevedo, S. M. Benson, T. Bradley, J. Brouwer, Y. M. Chiang, C. T. Clack, A. Cohen, S. Doig, J. Edmonds, P. Fennell, C. B. Field, B. Hannegan, B. M. Hodge, M. I. Hoffert, E. Ingersoll, P. Jaramillo, K. S. Lackner, K. J. Mach, M. Mastrandrea, J. Ogden, P. F. Peterson, D. L. Sanchez, D. Sperling, J. Stagner, J. E. Trancik, C. J. Yang, K. Caldeira, "Net-zero emissions energy systems", *Science (80-.).* **2018**, *360*, DOI 10.1126/science.aas9793.

[3] S. Nitopi, E. Bertheussen, S. B. Scott, X. Liu, A. K. Engstfeld, S. Horch, B. Seger, I. E. Stephens, K. Chan, C. Hahn, J. K. Nørskov, T. F. Jaramillo, I. Chorkendorff, "Progress and Perspectives of Electrochemical CO2 Reduction on Copper in Aqueous Electrolyte", *Chem. Rev.* **2019**, *119*, 7610–7672.

[4] J. Zhang, C. D. Sewell, H. Huang, Z. Lin, "Closing the Anthropogenic Chemical Carbon Cycle toward a Sustainable Future via CO2 Valorization", *Adv. Energy Mater.* **2021**, *11*, 1–38.

[5] K. Müller, L. Mokrushina, W. Arlt, "Thermodynamic constraints for the utilization of CO2", *Chemie-Ingenieur-Technik* **2014**, *86*, 497–503.

[6] Z. Jiang, T. Xiao, V. L. Kuznetsov, P. P. Edwards, "Turning carbon dioxide into fuel", *Philos. Trans. R. Soc. A Math. Phys. Eng. Sci.* **2010**, *368*, 3343–3364.

[7] R. G. Grim, Z. Huang, M. T. Guarnieri, J. R. Ferrell, L. Tao, J. A. Schaidle, "Transforming the carbon economy: Challenges and opportunities in the convergence of low-cost electricity and reductive CO2 utilization", *Energy Environ. Sci.* **2020**, *13*, 472–494.

[8] J. Rosen, G. S. Hutchings, Q. Lu, S. Rivera, Y. Zhou, D. G. Vlachos, F. Jiao, "Mechanistic Insights into the Electrochemical Reduction of CO2 to CO on Nanostructured Ag Surfaces", *ACS Catal.* **2015**, *5*, 4293–4299.

[9] M. R. Dubois, D. L. Dubois, "Development of molecular electrocatalysts for CO2 reduction and H2 production/oxidation", *Acc. Chem. Res.* **2009**, *42*, 1974–1982.

[10] E. E. Benson, C. P. Kubiak, A. J. Sathrum, J. M. Smieja, "Electrocatalytic and homogeneous approaches to conversion of CO2 to liquid fuels", *Chem. Soc. Rev.* **2009**, *38*, 89–99.

[11] F. Schüth, R.-A. Eichel, "Energiespeicher für die Zukunft", *Phys. J.* **2014**, *13*, 31–36.

[12] E. Gräfin von Westarp, B. Hecker, H. Tempel, R.-A. Eichel, "Power-to-Ethanol Using Bimetallic Catalysts: Reaction Paths, Transfer to Gas Diffusion Electrode, and Future Perspectives", *Electrochem. Sci. Adv.* **2024**, 1–7.

[13] Y. Hori, H. H. I. Wakebe, T. Tsukamoto, O. Koga, "Electrocatalytic Process of CO Selectivity in Electrochemical Reduction of Co2 at Metal Electrodes in Aqueous Media", *Electrochim. Acta* **1994**, *39*, 1833–1839.

[14] S. Komatsu, T. Zanagihara, Y. Hiraga, M. Tanaka, A. Kunugi, "Electrochemical Reduction of CO2 at Sb and Bi Electrodes in KHCO3 Solutions", *Denki Kagaku oyobi Kogyo Butsuri Kagaku* **1995**, *63*, 217–224.

[15] A. Goyal, G. Marcandalli, V. A. Mints, M. T. Koper, "Competition between CO2Reduction and Hydrogen Evolution on a Gold Electrode under Well-Defined Mass Transport Conditions", *J. Am. Chem. Soc.* **2020**, *142*, 4154–4161.

[16] T. Jaster, A. Gawel, D. Siegmund, J. Holzmann, H. Lohmann, E. Klemm, U. P. Apfel, "Electrochemical CO2 reduction toward multicarbon alcohols - The microscopic world of catalysts & process conditions", *iScience* **2022**, *25*, 104010.

[17] N. Martic, C. Reller, C. Macauley, M. Lo, A. M. Reichert, T. Reichbauer, K.-m. Vetter, B. Schmid, D. Mclaughlin, P. Leidinger, D. Reinisch, C. Vogl, K. J. J. Mayrhofer, "Ag2Cu2O3 – a catalyst template material for selective electroreduction of CO to C2+ products", *Energy Environ. Sci.* **2020**, DOI `10.1039/d0ee01100b`.

[18] H. Chen, C. Ding, C. Kang, J. Zeng, Y. Li, Y. Li, Y. Li, C. Li, J. He, "The design of alternative anodic reactions paired with electrochemical CO2 reduction", *Green Chem.* **2023**, *25*, 5320–5337.

[19] S. Wang, T. Kou, S. E. Baker, E. B. Duoss, Y. Li, " Electrochemical Reduction of CO 2 to Alcohols: Current Understanding, Progress, and Challenges ", *Adv. Energy Sustain. Res.* **2022**, *3*, 2100131.

[20] A. Bagger, W. Ju, A. S. Varela, P. Strasser, J. Rossmeisl, "Electrochemical CO2 Reduction: A Classification Problem", *ChemPhysChem* **2017**, *18*, 3266–3273.

[21] A. A. Peterson, J. K. Nørskov, "Activity descriptors for CO 2 electroreduction to methane on transition-metal catalysts", *J. Phys. Chem. Lett.* **2012**, *3*, 251–258.

[22] K. P. Kuhl, E. R. Cave, D. N. Abram, T. F. Jaramillo, "New insights into the electrochemical reduction of carbon dioxide on metallic copper surfaces", *Energy Environ. Sci.* **2012**, *5*, 7050–7059.

[23] H. Zhang, W. A. Goddard, Q. Lu, M. J. Cheng, "The importance of grand-canonical quantum mechanical methods to describe the effect of electrode potential on the stability of intermediates involved in both electrochemical CO2 reduction and hydrogen evolution", *Phys. Chem. Chem. Phys.* **2018**, *20*, 2549–2557.

[24] J. Hou, X. Chang, J. Li, B. Xu, Q. Lu, "Correlating CO Coverage and CO Electroreduction on Cu via High-Pressure in Situ Spectroscopic and Reactivity Investigations", *J. Am. Chem. Soc.* **2022**, *144*, 22202–22211.

[25] D. Ren, J. Fong, B. S. Yeo, "The effects of currents and potentials on the selectivities of copper toward carbon dioxide electroreduction", *Nat. Commun.* **2018**, *9*, DOI 10.1038/s41467-018-03286-w.

[26] Y. Zong, P. Chakthranont, J. Suntivich, "Temperature Effect of CO2 Reduction Electrocatalysis on Copper: Potential Dependency of Activation Energy", *J. Electrochem. Energy Convers. Storage* **2020**, *17*, 1–7.

[27] R. Kortlever, J. Shen, K. J. P. Schouten, F. Calle-Vallejo, M. T. Koper, "Catalysts and Reaction Pathways for the Electrochemical Reduction of Carbon Dioxide", *J. Phys. Chem. Lett.* **2015**, *6*, 4073–4082.

[28] T. T. Hoang, S. Verma, S. Ma, T. T. Fister, J. Timoshenko, A. I. Frenkel, P. J. Kenis, A. A. Gewirth, "Nanoporous Copper-Silver Alloys by Additive-Controlled Electrodeposition for the Selective Electroreduction of CO2 to Ethylene and Ethanol", *J. Am. Chem. Soc.* **2018**, *140*, 5791–5797.

[29] Y. Lum, J. W. Ager, "Sequential catalysis controls selectivity in electrochemical CO_2 reduction on Cu", *Energy Environ. Sci.* **2018**, *11*, DOI 0.1039/c8ee01501e.

[30] T. T. Zhuang, Y. Pang, Z. Q. Liang, Z. Wang, Y. Li, C. S. Tan, J. Li, C. T. Dinh, P. De Luna, P. L. Hsieh, T. Burdyny, H. H. Li, M. Liu, Y. Wang, F. Li, A. Proppe, A. Johnston, D. H. Nam, Z. Y. Wu, Y. R. Zheng, A. H. Ip, H. Tan, L. J. Chen, S. H. Yu, S. O. Kelley, D. Sinton, E. H. Sargent, "Copper nanocavities confine intermediates for efficient electrosynthesis of C3 alcohol fuels from carbon monoxide", *Nat. Catal.* **2018**, *1*, 946–951.

[31] C. Reller, R. Krause, E. Volkova, B. Schmid, S. Neubauer, A. Rucki, M. Schuster, G. Schmid, "Selective Electroreduction of CO2 toward Ethylene on Nano Dendritic Copper Catalysts at High Current Density", *Adv. Energy Mater.* **2017**, *7*, 1–8.

[32] A. Verdaguer-Casadevall, C. W. Li, T. P. Johansson, S. B. Scott, J. T. McKeown, M. Kumar, I. E. Stephens, M. W. Kanan, I. Chorkendorff, "Probing the Active Surface Sites for CO Reduction on Oxide-Derived Copper Electrocatalysts", *J. Am. Chem. Soc.* **2015**, *137*, 9808–9811.

[33] D. Ren, N. T. Wong, A. D. Handoko, Y. Huang, B. S. Yeo, "Mechanistic Insights into the Enhanced Activity and Stability of Agglomerated Cu Nanocrystals for the Electrochemical Reduction of Carbon Dioxide to n-Propanol", *J. Phys. Chem. Lett.* **2016**, *7*, 20–24.

[34] A. Murata, Y. Hori, Product selectivity affected by cationic species in electrochemical reduction of CO2 and CO at a Cu electrode, **1991**.

[35] M. R. Singh, Y. Kwon, Y. Lum, J. W. Ager, A. T. Bell, "Hydrolysis of Electrolyte Cations Enhances the Electrochemical Reduction of CO2 over Ag and Cu", *J. Am. Chem. Soc.* **2016**, *138*, 13006–13012.

[36] M. G. Kibria, J. P. Edwards, C. M. Gabardo, C. T. Dinh, A. Seifitokaldani, D. Sinton, E. H. Sargent, "Electrochemical CO2 Reduction into Chemical Feedstocks: From Mechanistic Electrocatalysis Models to System Design", *Adv. Mater.* **2019**, *31*, 1–24.

[37] D. M. Weekes, D. A. Salvatore, A. Reyes, A. Huang, C. P. Berlinguette, "Electrolytic CO2 Reduction in a Flow Cell", *Acc. Chem. Res.* **2018**, *51*, 910–918.

[38] Y. Hori, R. Takahashi, Y. Yoshinami, A. Murata, "Electrochemical reduction of CO at a copper electrode", *J. Phys. Chem. B* **1997**, *101*, 7075–7081.

[39] A. A. Peterson, F. Abild-Pedersen, F. Studt, J. Rossmeisl, J. K. Nørskov, "How copper catalyzes the electroreduction of carbon dioxide into hydrocarbon fuels", *Energy Environ. Sci.* **2010**, *3*, 1311–1315.

[40] A. J. Garza, A. T. Bell, M. Head-Gordon, "Mechanism of CO2 Reduction at Copper Surfaces: Pathways to C2 Products", *ACS Catal.* **2018**, *8*, 1490–1499.

[41] N. S. Romero Cuellar, C. Scherer, B. Kaçkar, W. Eisenreich, C. Huber, K. Wiesner-Fleischer, M. Fleischer, O. Hinrichsen, "Two-step electrochemical reduction of CO2 towards multi-carbon products at high current densities", *J. CO2 Util.* **2020**, *36*, 263–275.

[42] L. R. L. Ting, O. Piqué, S. Y. Lim, M. Tanhaei, F. Calle-Vallejo, B. S. Yeo, "Enhancing CO2 Electroreduction to Ethanol on Copper-Silver Composites by Opening an Alternative Catalytic Pathway", *ACS Catal.* **2020**, *10*, 4059–4069.

[43] D. Choukroun, L. Pacquets, C. Li, S. Hoekx, S. Arnouts, K. Baert, T. Hauffman, S. Bals, T. Breugelmans, "Mapping Composition-Selectivity Relationships of Supported Sub-10 nm Cu-Ag Nanocrystals for High-Rate CO2Electroreduction", *ACS Nano* **2021**, *15*, 14858–14872.

[44] J. Huang, M. Mensi, E. Oveisi, V. Mantella, R. Buonsanti, "Structural Sensitivities in Bimetallic Catalysts for Electrochemical CO2 Reduction Revealed by Ag-Cu Nanodimers", *J. Am. Chem. Soc.* **2019**, *141*, 2490–2499.

[45] P. Wang, H. Yang, C. Tang, Y. Wu, Y. Zheng, T. Cheng, K. Davey, X. Huang, S. Z. Qiao, "Boosting electrocatalytic CO2–to–ethanol production via asymmetric C–C coupling", *Nat. Commun.* **2022**, *13*, 1–11.

[46] H. Tang, Y. Liu, Y. Zhou, Y. Qian, B. L. Lin, "Boosting the Electroreduction of CO2 to Ethanol via the Synergistic Effect of Cu-Ag Bimetallic Catalysts", *ACS Appl. Energy Mater.* **2022**, *5*, 14045–14052.

[47] S. Lee, G. Park, J. Lee, "Importance of Ag-Cu Biphasic Boundaries for Selective Electrochemical Reduction of CO2 to Ethanol", *ACS Catal.* **2017**, *7*, 8594–8604.

[48] Z. Huang, R. G. Grim, J. A. Schaidle, L. Tao, "The economic outlook for converting CO2and electrons to molecules", *Energy Environ. Sci.* **2021**, *14*, 3664–3678.

[49] J. Li, R. Zhao, Y. Xu, X. Wu, S. R. Bean, D. Wang, "Fuel ethanol production from starchy grain and other crops: An overview on feedstocks, affecting factors, and technical advances", *Renew. Energy* **2022**, *188*, 223–239.

[50] A. S. Duden, P. A. Verweij, A. P. Faaij, D. Baisero, C. Rondinini, F. van der Hilst, "Biodiversity impacts of increased ethanol production in Brazil", *Land* **2020**, *9*, DOI 10.3390/land9010012.

[51] J. Baras, S. Gacesa, D. Pejin, "Ethanol is a strategic raw material", *Hem. Ind.* **2002**, *56*, 89–104.

[52] C. Ampelli, F. Tavella, D. Giusi, A. M. Ronsisvalle, S. Perathoner, G. Centi, "Electrode and cell design for CO2 reduction: A viewpoint", *Catal. Today* **2023**, *421*, 114217.

[53] S. Hernandez-Aldave, E. Andreoli, "Fundamentals of gas diffusion electrodes and electrolysers for carbon dioxide utilisation: Challenges and opportunities", *Catalysts* **2020**, *10*, 1–34.

[54] E. Robens, B. Hecker, H. Kungl, H. Tempel, R. A. Eichel, "Bimetallic Copper-Silver Catalysts for the Electrochemical Reduction of CO2 to Ethanol", *ACS Appl. Energy Mater.* **2023**, *6*, 7571–7577.

[55] W. Lai, Y. Qiao, Y. Wang, H. Huang, "Stability Issues in Electrochemical CO2 Reduction: Recent Advances in Fundamental Understanding and Design Strategies", *Adv. Mater.* **2023**, *2306288*, 1–28.

[56] L. M. Baumgartner, C. I. Koopman, A. Forner-Cuenca, D. A. Vermaas, "When Flooding Is Not Catastrophic-Woven Gas Diffusion Electrodes Enable Stable CO2Electrolysis", *ACS Appl. Energy Mater.* **2022**, *5*, 15125–15135.

[57] J. B. Vennekötter, T. Scheuermann, R. Sengpiel, M. Wessling, "The electrolyte matters: Stable systems for high rate electrochemical CO2 reduction", *J. CO2 Util.* **2019**, *32*, 202–213.

[58] R. K. Miao, Y. Xu, A. Ozden, A. Robb, C. P. O'Brien, C. M. Gabardo, G. Lee, J. P. Edwards, J. E. Huang, M. Fan, X. Wang, S. Liu, Y. Yan, E. H. Sargent, D. Sinton, "Electroosmotic flow steers neutral products and enables concentrated ethanol electroproduction from CO2", *Joule* **2021**, *5*, 2742–2753.

[59] J. B. Vennekoetter, R. Sengpiel, M. Wessling, "Beyond the catalyst: How electrode and reactor design determine the product spectrum during electrochemical CO2 reduction", *Chem. Eng. J.* **2019**, *364*, 89–101.

[60] S. Park, B. N. Popov, "Effect of a GDL based on carbon paper or carbon cloth on PEM fuel cell performance", *Fuel* **2011**, *90*, 436–440.

[61] S. Park, J. W. Lee, B. N. Popov, "A review of gas diffusion layer in PEM fuel cells: Materials and designs", *Int. J. Hydrogen Energy* **2012**, *37*, 5850–5865.

[62] H. Rabiee, L. Ge, X. Zhang, S. Hu, M. Li, Z. Yuan, "Gas diffusion electrodes (GDEs) for electrochemical reduction of carbon dioxide, carbon monoxide, and dinitrogen to value-added products: A review", *Energy Environ. Sci.* **2021**, *14*, 1959–2008.

[63] Y. C. Tan, K. B. Lee, H. Song, J. Oh, "Modulating Local CO2 Concentration as a General Strategy for Enhancing C-C Coupling in CO2 Electroreduction", *Joule* **2020**, *4*, 1104–1120.

[64] V. M. Schmidt, *Elektrochemische Verfahrenstechnik: Grundlagen, Reaktionstechnik, Prozessoptimierung*, John Wiley & Sons, **2012**.

[65] P. Kurzweil, *Das Vieweg Einheiten-Lexikon: Formeln und Begriffe aus Physik, Chemie und Technik*, Springer-Verlag, **2013**.

[66] W. Ma, X. He, W. Wang, S. Xie, Q. Zhang, Y. Wang, " Electrocatalytic reduction of CO 2 and CO to multi-carbon compounds over Cu-based catalysts ", *Chem. Soc. Rev.* **2021**, DOI 10.1039/d1cs00535a.

[67] B. Endrődi, A. Samu, E. Kecsenovity, T. Halmágyi, D. Sebők, C. Janáky, "Operando cathode activation with alkali metal cations for high current density operation of water-fed zero-gap carbon dioxide electrolysers", *Nat. Energy* **2021**, *6*, 439–448.

[68] S. Liu, H. Tao, L. Zeng, Q. Liu, Z. Xu, Q. Liu, J. L. Luo, "Shape-Dependent Electrocatalytic Reduction of CO2 to CO on Triangular Silver Nanoplates", *J. Am. Chem. Soc.* **2017**, *139*, 2160–2163.

[69] C. Kim, H. S. Jeon, T. Eom, M. S. Jee, H. Kim, C. M. Friend, B. K. Min, Y. J. Hwang, "Achieving Selective and Efficient Electrocatalytic Activity for CO2 Reduction Using Immobilized Silver Nanoparticles", *J. Am. Chem. Soc.* **2015**, *137*, 13844–13850.

[70] X. Peng, S. G. Karakalos, W. E. Mustain, "Preferentially Oriented Ag Nanocrystals with Extremely High Activity and Faradaic Efficiency for CO2 Electrochemical Reduction to CO", *ACS Appl. Mater. Interfaces* **2018**, *10*, 1734–1742.

[71] A. Bard, G. Inzelt, F. Scholz, *Electrochemical Dictionary*, Springer Berlin Heidelberg, **2012**.

[72] J. P. Jones, G. K. Prakash, G. A. Olah, Electrochemical CO2 Reduction: Recent Advances and Current Trends, **2014**.

[73] R. Neugebauer, *Ressourceneffizienz: Schlüsseltechnologien für Wirtschaft & Gesellschaft*, Springer, **2016**.

[74] R. Kas, R. Kortlever, A. Milbrat, M. T. Koper, G. Mul, J. Baltrusaitis, "Electrochemical CO2 reduction on Cu2O-derived copper nanoparticles: Controlling the catalytic selectivity of hydrocarbons", *Phys. Chem. Chem. Phys.* **2014**, *16*, 12194–12201.

[75] R. Scott, C. Lukehart, *Applications of Physical Methods to Inorganic and Bioinorganic Chemistry*, Wiley, **2007**.

[76] R. Huggins, *Advanced Batteries: Materials Science Aspects*, Springer US, **2008**.

[77] F. Muench, R. Popovitz-Biro, T. Bendikov, Y. Feldman, B. Hecker, M. Oezaslan, I. Rubinstein, A. Vaskevich, "Nucleation-Controlled Solution Deposition of Silver Nanoplate Architectures for Facile Derivatization and Catalytic Applications", *Adv. Mater.* **2018**, *30*, 1–6.

[78] F. Muench, A. Vaskevich, R. Popovitz-Biro, T. Bendikov, Y. Feldman, I. Rubinstein, "Expanding the boundaries of metal deposition: High aspect ratio silver nanoplatelets created by merging nanobelts", *Electrochim. Acta* **2018**, *264*, 233–243.

[79] B. Hecker, E. Robens, H. E. Valencia, A. Windmüller, F. Muench, M. Meledina, H. Tempel, H. Kungl, J. Mayer, R.-A. Eichel, " Effects of Synthesized Silver Nanoplate Structures on the Electrochemical Reduction of CO 2 ", *J. Electrochem. Soc.* **2023**, *170*, 096505.

[80] C. L. Lee, C. C. Syu, "Ag nanoparticle as a new activator for catalyzing electroless copper bath with 2,2'-bipyridyl", *Electrochim. Acta* **2011**, *56*, 8880–8883.

[81] C.-H. Chen, H.-L. Yang, H.-R. Chen, C.-L. Lee, "Activity on Electrochemical Surface Area: Silver Nanoplates as New Catalysts for Electroless Copper Deposition", *J. Electrochem. Soc.* **2012**, *159*, D507–D511.

[82] N. Gupta, M. Gattrell, B. MacDougall, "Calculation for the cathode surface concentrations in the electrochemical reduction of CO2 in KHCO3 solutions", *J. Appl. Electrochem.* **2006**, *36*, 161–172.

[83] A. Herzog, A. Bergmann, H. S. Jeon, J. Timoshenko, S. Kühl, C. Rettenmaier, M. Lopez Luna, F. T. Haase, B. Roldan Cuenya, "Operando Investigation of Ag-Decorated Cu2O Nanocube Catalysts with Enhanced CO2 Electroreduction toward Liquid Products", *Angew. Chemie - Int. Ed.* **2021**, *60*, 7426–7435.

[84] P. Grosse, D. Gao, F. Scholten, I. Sinev, H. Mistry, B. Roldan Cuenya, "Dynamic Changes in the Structure, Chemical State and Catalytic Selectivity of Cu Nanocubes during CO2 Electroreduction: Size and Support Effects", *Angew. Chemie - Int. Ed.* **2018**, *57*, 6192–6197.

[85] D. Zagorac, H. Muller, S. Ruehl, J. Zagorac, S. Rehme, "Recent developments in the Inorganic Crystal Structure Database: Theoretical crystal structure data and related features", *J. Appl. Crystallogr.* **2019**, *52*, 918–925.

[86] H. Ooka, M. C. Figueiredo, M. T. Koper, "Competition between Hydrogen Evolution and Carbon Dioxide Reduction on Copper Electrodes in Mildly Acidic Media", *Langmuir* **2017**, *33*, 9307–9313.

[87] E. Santos, K. Pötting, A. Lundin, P. Quaino, W. Schmickler, "Hydrogen evolution on single-crystal copper and silver: A theoretical study", *ChemPhysChem* **2010**, *11*, 1491–1495.

[88] A. D. Handoko, C. W. Ong, Y. Huang, Z. G. Lee, L. Lin, G. B. Panetti, B. S. Yeo, "Mechanistic insights into the selective electroreduction of carbon dioxide to ethylene on Cu2O-derived copper catalysts", *J. Phys. Chem. C* **2016**, *120*, 20058–20067.

[89] A. Dutta, M. Rahaman, N. C. Luedi, M. Mohos, P. Broekmann, "Morphology Matters: Tuning the Product Distribution of CO2 Electroreduction on Oxide-Derived Cu Foam Catalysts", *ACS Catal.* **2016**, *6*, 3804–3814.

[90] M. Chang, W. Ren, W. Ni, S. Lee, X. Hu, "Ionomers Modify the Selectivity of Cu-Catalyzed Electrochemical CO2 Reduction", *ChemSusChem* **2022**, *202201687*, DOI 10.1002/cssc.202201687.

[91] M. Ma, B. J. Trześniewski, J. Xie, W. A. Smith, "Selective and Efficient Reduction of Carbon Dioxide to Carbon Monoxide on Oxide-Derived Nanostructured Silver Electrocatalysts", *Angew. Chemie - Int. Ed.* **2016**, *55*, 9748–9752.

[92] G. L. De Gregorio, T. Burdyny, A. Loiudice, P. Iyengar, W. A. Smith, R. Buonsanti, "Facet-Dependent Selectivity of Cu Catalysts in Electrochemical CO2 Reduction at Commercially Viable Current Densities", *ACS Catal.* **2020**, *10*, 4854–4862.

[93] Z. Z. Niu, L. P. Chi, R. Liu, Z. Chen, M. R. Gao, "Rigorous assessment of CO2electroreduction products in a flow cell", *Energy Environ. Sci.* **2021**, *14*, 4169–4176.

[94] L. Xue, X. Wu, Y. Liu, B. Xu, X. Wang, S. Dai, P. Liu, H. Yang, "Hydrophobic 1-octadecanethiol functionalized copper catalyst promotes robust high-current CO2 gas-diffusion electrolysis", *Nano Res.* **2022**, *15*, 1393–1398.

[95] H. Shi, L. Luo, C. Li, Y. Li, T. Zhang, Z. Liu, J. Cui, L. Gu, L. Zhang, Y. Hu, H. Li, C. Li, "Stabilizing Cu+ Species in Cu2O/CuO Catalyst via Carbon Intermediate Confinement for Selective CO2RR", *Adv. Funct. Mater.* **2024**, *34*, 1–7.

A List of Abbreviations and Symbols

Abbreviations

^{1}H-NMR	^{1}H-nuclear magnetic resonance
Ag NPls	silver nanoplates
CA	chronoamperometry
CCS	"carbon capture and storage"
CCU	"carbon capture and utilization"
CE	counter electrode
CEM	cation exchange membrane
CO_2RR	CO_2 reduction reaction
CP	chronopotentiometry
CuAg NPls	copper-silver nanoplates
CV	cyclic voltammetry
Cu NP	copper nanoparticle
ECSA	electrochemical surface area
EDTA	ethylenediaminetetraacetic acid
EDX	energy-dispersive X-ray spectroscopy
FE	Faradaic efficiency
GC	gas chromatography
GDE	gas diffusion electrode
GDL	gas diffusion layer
HER	hydrogen evolution reaction
HS-GC	headspace gas chromatography
ICP-MS	inductively coupled plasma mass spectrometry
IEC	ion exclusion chromatography
IR drop	voltage drop
MEA	membrane electrode assembly
MPL	microporous layer

OER	oxygen evolution reaction
P1	plating solution 1
P2	plating solution 2
PEIS	potentio electrochemical impedance spectroscopy
PTFE	polytetrafluoroethylene
RE	reference electrode
RHE	reversible hydrogen electrode
S1	seeding solution 1
S2	seeding solution 2
SEM	scanning electron microscopy
SHE	standard hydrogen electrode
WE	working electrode
XPS	X-ray photoelectron spectroscopy
XRD	X-ray diffraction

Element and Molecule Abbreviations

Ag	silver
Au	gold
Bi	bismuth
C	carbon
CO	carbon monoxide
CO_2	carbon dioxide
Cu	copper
Fe	iron
H_2	hydrogen
H_2O	water
H_2SO_4	sulfuric acid
$KHCO_3$	potassium bicarbonate
MEK	methyl ethyl ketone
Ni	nickel
O_2	oxygen
Pb	lead
Pt	platinum

Sn	tin
Ti	titanium
Zn	zinc

Symbols

Formula symbol	Unit	Name
A_{ECSA}	[$\mathrm{cm^2}$]	Electrochemical surface area
A_{geo}	[$\mathrm{cm^2}$]	Geometric surface area
E	[V]	Potential
E°	[V]	Standard electrode potential
E_{IR}	[V]	IR corrected potential
E_{p}	[V]	Measured potential with the potentiostat
E_{TD}	[V]	Thermodynamic potential
F	[$\mathrm{C\,mol^{-1}}$]	Faraday constant ($\mathrm{F} = 96485.309\,\mathrm{C\,mol^{-1}}$)
FE	[%]	Faradaic efficiency
I	[mA]	Current
j	[$\mathrm{mA\,cm^{-2}}$]	Current density
j_{ECSA}	[$\mathrm{mA\,cm^{-2}}$]	Current density with regard to the electrochemical surface area
j_{geo}	[$\mathrm{mA\,cm^{-2}}$]	Current density with regard to the geometric surface area
k	[-]	Required amount of H_2O for CO_2RR
n	[mol]	Amount of substance
$\dot{n}$	[$\mathrm{mol\,s^{-1}}$]	Formation rate
pH	[-]	pH-value
Q	[C]	Charge
R_{I}	[Ω]	Resistance between WE and RE
$\dot{V}$	[$\mathrm{L\,s^{-1}}$]	Volume flow
V_{m}	[$\mathrm{L\,mol^{-1}}$]	Molar gas volume
y	[-]	Required amount of OH^- for CO_2RR
x	[-]	Required amount of CO_2 for CO_2RR
z	[-]	Number of transferred electrons
η	[V]	Overpotential
ϕ	[-]	Volume fraction

B List of Figures

1 Schematic diagram of CO_2 electrolysis showing the reactants and formed products on the anode and cathode sides. The influence of pure metal electrocatalysts on the product formation is also illustrated. 4

2 Computed binding energies of adsorbed CO and H on different metal catalysts. The metals that form H_2, CO, or formate are depicted in red, blue, and yellow, respectively. In turquoise, Cu is marked as material forming products beyond CO. The black lines represent the boundaries between adsorbed and non-adsorbed H or CO.[20] Clearance was granted via the licence number 5811940310401. 5

3 Product formation of the CO_2 reduction reaction (CO_2RR) at a Cu electrode as a function of the applied potential.[22] The products are divided into major, intermediate, and minor products depending on their current efficiency. Clearance was granted via the licence ID 1495778-1. 8

4 The four key steps of one proposed reaction mechanism for the formation of ethanol and ethylene on Cu electrodes (SDI: selectivity-determining intermediate).[27] 9

5 The three key steps of the CO_2 reduction reaction to ethanol in abundance of *CO (1: shown for x = 2).[42] 10

6 Possible business case for the CO_2 reduction reaction with ethanol as target product (FOAK: first-of-a-kind). 11

7 Schematic illustration of an H-type electrolyzer for the electrochemical reduction of CO_2: (a) based on the real shape of the cell (RE: reference electrode, WE: working electrode, CE: counter electrode; note: For simplicity, the RE is drawn on the backside of the cathode; in reality, the RE points to the front side of the WE.)[54] and (b) more schematic and thus easier to compare with the other cell schemes shown below.[12] Note: For figure (b), graphical support was provided by Sebastian Lehmann. 13

8 Schematic illustration of a liquid-phase electrolyzer (GDE: gas diffusion electrode).[12] Note: Graphical support was provided by Sebastian Lehmann. 14

9 Sketches of influence of the cation crossover in an electrolyzer using a cation exchange membrane: (a) $KHCO_3$ is used as catholyte and anolyte, (b) $KHCO_3$ is used as catholyte and H_2SO_4 as anolyte (C: cathode, CEM: cation exchange membrane, A: anode). Graphic inspired by [57]. 16

10 Schematic illustration of a gas-phase electrolyzer (GDE: gas diffusion electrode).[12] Note: Graphical support was provided by Sebastian Lehmann. 17
11 Schematic illustration of a gas diffusion electrode, consisting of a catalyst layer applied on a dual-layer gas diffusion layer with a macro- and microporous layer. The diffusion pathways for the reactant CO_2 and the products are are also shown.[12] Note: Graphical support was provided by Sebastian Lehmann. 18

12 Scheme of the synthesis of copper-silver nanoplates used in the H-type electrolyzer: first, silver nanoplates are formed in a two-step synthesis followed by electroless copper deposition.[54] 24
13 Scheme of the electrode preparation with copper nanoparticles as electrocatalyst and glassy carbon as substrate using spray coating as manufacturing technique. 25
14 Photo of the custom-made H-type electrolyzer, in whose cathode compartment the self-made sample holder and the reference electrode are inserted. Note: The cathode compartment is on the left-hand side, as otherwise it would not be possible to show the reference electrode in the photo. 26
15 Schematic representation of the different steps for synthesizing the copper-silver nanoplates for the liquid-phase electrolyzer (Ag NPls: silver nanoplates, CuAg NPls: copper-silver nanoplates). 28
16 Scheme of the preparation of gas diffusion electrode with copper-silver nanoplates as electrocatalyst using drop casting as manufacturing technique. 29
17 Scheme of the preparation of gas diffusion electrode with copper nanoparticles as electrocatalyst using spray coating as manufacturing technique. 29
18 Photo of the static FlexCell from Gaskatel with inserted Ag/AgCl (sat.) reference electrode and a T-piece at the gas outlet of the catholyte compartment for taking liquid samples. 30
19 Schematic representation of the two stream selector positions (GC: gas chromatography). Position 1: the gas from the gas side is directed to the GC and the gas from the catholyte side to its gas counter (MGC-1); position 2: the gas from the catholyte side is directed to the GC and the gas from the gas side to its gas counter (TG05). 32

20 Schematic representation of the (a) old and (b) new design of the Haber-Luggin capillary: (1) reference electrode inserted with Haber-Luggin capillary, (2) working electrode, and (3) tip of the capillary filled with Nafion stripes (blue), secured with Kapton tape (orange). . . 36

21 Schematic illustration of the (a) old and (b) new design of the CO_2 gas supply in the cathode compartment of the H-type electrolyzer. In the old design, the gas supply is mounted behind the working electrode, whereas in the new design it is inserted in front of it. Note: For simplicity, the RE is drawn on the backside of the cathode; in reality, the RE points to the front side of the WE (compare figure 20). 37
22 Influence of the positioning of the CO_2 gas inlet on the *FE*s measured using a Cu foil as WE. The measurements are performed at a constant potential of -1.0 V vs. RHE (IR-corrected), resulting in a current density of around -7 mA cm^{-2} for the experiment conducted with the gas inlet behind the WE and of around -8 mA cm^{-2} for the experiment with the gas inlet in front of the WE. The measurements are performed for 100 minutes using a 0.1 M $KHCO_3$ electrolyte and the data are averaged over two individual runs. 38
23 Photo of the cathode compartment of the H-type electrolyzer: (left) a gas bubble is trapped between WE and Haber-Luggin capillary, (right) no gas bubble is trapped. In addition, magnifications of the highlighted areas are shown in the middle. The measurement is performed at a constant potential of -1.0 V vs. RHE and in a 0.1 M $KHCO_3$ electrolyte. 39
24 Effect of a trapped gas bubble on the measured values: (a) measurement at a constant potential of -1.0 V vs. RHE, (b) measurement at a constant current of -10 mA. The gray areas mark in (a) the time interval in which a gas bubble is trapped between the WE and Haber-Luggin capillary and in (b) the time at which a gas bubble is released. Both measurements are conducted in a 0.1 M $KHCO_3$ electrolyte. 40
25 (a,b) SEM images of the top surface of CuAg NPls with 45 % near-surface Cu content and (c) a cross-section of the resin-embedded catalyst with 90 % near-surface Cu content. Additionally, SEM/EDX overlay of CuAg NPls with 45 % near-surface Cu content (d, Cu depicted in red).[54] 41
26 XRD patterns of Ag NPls and with Cu deposited Ag NPls. Additionally, XRD patterns from the ICS database[85] of Ag and Cu are shown. Cu content is determined by XPS. The corresponding element and surface orientation of each peak are indiacted above the diagram.[54] . . . 42
27 (a) Linear correlation between Cu content measured by EDX and the total Cu content measured by ICP-MS. The red line represent the linear fit of the data. (b) Comparison of the total Cu content (calibrated from EDX) and the near-surface (measured by XPS) Cu content of several samples of the new bimetallic catalyst. The red line provides a guide-to-the eye for the reader.[54] 43

28 CV curves of the new bimetallic catalyst with different near-surface Cu contents (see legend, measured by XPS). The measurements are performed in a potential range from -0.1 V to -0.5 V vs. RHE with a scan rate of 20 mV s^{-1} and in a 0.1 M $KHCO_3$ electrolyte. To ensure reproducibility, the given data are averaged values of at least two samples with similar near-surface Cu content. The inset shows the CV curves for equally polished Ag and Cu foils as reference.[54] 44
29 Faradaic efficiency as a function of the near-surface Cu content (measured by XPS). The experiments are performed at -20 mA cm^{-2} and for 100 minutes. The data are averaged over two to three individual measurements.[54] 46
30 Correlation between the Faradaic efficiency of CO and the ethanol-to-ethylene ratio. The red numbers represent the copper content (measured by XPS) of the used catalyst. The error bars are calculated by Gaussian error propagation from the errors of the Faradaic efficiency of ethanol and ethylene. The dashed horizontal line marks the transition between the catalysts favoring ethylene (below) or ethanol (above) formation.[54] 47
31 Faradaic efficiency of 45 % copper catalysts (measured by XPS) as a function of current density and potential at the working electrode. The measurements were performed for 55 minutes and the data are averaged over three individual runs.[54] 48
32 CO_2RR at a constant current density of -44 mA cm^{-2} using Cu NPs "big" as catalyst with Nafion as binder and a catalyst loading of 2 mg cm^{-2} on glassy carbon: (a) plot of the applied current density and the resulting potential at the WE versus time, (b) graph with the calculated *FE*s time-resolved. The experiment is conducted in the H-type electrolyzer using a 0.1 M $KHCO_3$ electrolyte. 50
33 CV curves using the Cu NPs "big" as catalyst with Nafion as binder and different catalyst loadings on glassy carbon: 2 mg cm^{-2} is depicted in black and 0.7 mg cm^{-2} in green. The measurements are performed in a potential range from -0.1 V to -1.1 V vs. RHE prior the IR correction with a scan rate of 20 mV s^{-1}. The experiments are conducted in the H-type electrolyzer using a 0.1 M $KHCO_3$ electrolyte. 51
34 CO_2RR at a constant current density of -10 mA cm^{-2} using Cu NPs "big" as catalyst with Nafion as binder and a decreased catalyst loading of 0.7 mg cm^{-2} on glassy carbon: (a) plot of the applied current density and the resulting potential at the WE versus time, (b) graph with the calculated *FE*s time-resolved. The experiment is conducted in the H-type electrolyzer using a 0.1 M $KHCO_3$ electrolyte. 52

35 CV curves using two different types of Cu NPs as catalyst with Nafion as binder and a catalyst loading of 0.7 mg cm^{-2} on glassy carbon: Cu NPs "big" are depicted in green and Cu NPs "small" in blue. The measurements are performed in a potential range from -0.1 V to -1.1 V vs. RHE prior to the IR correction with a scan rate of 20 mV s^{-1}. The experiments are conducted in the H-type electrolyzer using a 0.1 M $KHCO_3$ electrolyte. 53
36 CO_2RR at a constant current density of -10 mA cm^{-2} using Cu NPs "small" as catalyst with Nafion as binder and a catalyst loading of 0.7 mg cm^{-2} on glassy carbon: (a) plot of the applied current density and the resulting potential at the WE, (b) graph with the calculated *FE*s time-resolved. The experiment is conducted in the H-type electrolyzer using a 0.1 M $KHCO_3$ electrolyte. 54
37 CO_2RR at a constant current density of -20 mA cm^{-2} using Cu NPs "small" as catalyst with Nafion as binder and a catalyst loading of 0.7 mg cm^{-2} on glassy carbon: (a) plot of the applied current density and the resulting potential at the WE, (b) graph with the calculated *FE*s time-resolved. The experiment is conducted in the H-type electrolyzer using a 0.1 M $KHCO_3$ electrolyte. 55
38 CV curves using two different types of Cu NPs as catalyst with Nafion as binder and a catalyst loading of 2 mg cm^{-2} on a GDL: Cu NPs "big" are depicted in green and Cu NPs "small" in blue. The measurements are performed in a potential range from -0.1 V to -1.1 V vs. RHE prior to the IR correction with a scan rate of 20 mV s^{-1}. The experiments are conducted in the static liquid-phase electrolyzer "FlexCell" using a 1 M $KHCO_3$ catholyte. 56
39 CO_2RRs at a constant current density of -100 mA cm^{-2} using two types of Cu NPs as catalyst with Nafion as binder and a catalyst loading of 2 mg cm^{-2} on a GDL: (a,c) plot of the applied current density and the resulting potential at the WE using the Cu NPs "big" in (a) and the Cu NPs "small" in (c); (b,d) graph with the calculated *FE*s time resolved using the Cu NPs "big" in (b) and the Cu NPs "small" in (d) (G: gas side, C: catholyte side). The experiments are conducted in the static liquid-phase electrolyzer "FlexCell" using a 1 M $KHCO_3$ catholyte. 58
40 SEM images of the CuAg NPls (a) grown on Ag foil and (b) grown in solution. Additionally, a cross-section image of a GDE prepared with the CuAg NPls grown in solution is shown in (c). 60

41 CO_2RRs using (a) CuAg NPls as catalyst with Nafion as binder and a catalyst loading of 1.4 mg cm^{-2} on a GDL [12] and (b) Ag NPls added with commercial Cu NPs as catalyst with Nafion as binder and a catalyst loading of 1.4 mg cm^{-2} on a GDL. The experiments are conducted at a constant current density of -100 mA cm^{-2} in the static liquid-phase electrolyzer "FlexCell", using a 1 M $KHCO_3$ catholyte and a CO_2 gas flow of 20 mL$_n$ min^{-1}. Note: The experiment in (a) is only performed for 70 minutes and the liquid samples are taken after 30 and 70 minutes. 61

42 (a) Plot of the applied current density (-100 mA cm^{-2}) and the resulting potential at the WE using Ag NPls added with commercial Cu NPs as catalyst with Nafion as binder and a catalyst loading of 1.4 mg cm^{-2} on a GDL. (b) CV curves using the Ag NPls added with commercial Cu NPs as catalyst with Nafion as binder and two different catalyst loadings on a GDL: 1.4 mg cm^{-2} is depicted in black and 0.7 mg cm^{-2} in green. The experiments are conducted in the static liquid-phase electrolyzer "FlexCell" using a 1 M $KHCO_3$ catholyte and a CO_2 gas flow of 20 mL$_n$ min^{-1}. 62

43 CO_2RR at a constant current density of -100 mA cm^{-2} using Ag NPls added with commercial Cu NPs as catalyst with Nafion as binder and a catalyst loading of 0.7 mg cm^{-2} on a GDL: (a) plot of the applied current density and the resulting potential at the WE, (b) graph with the calculated *FE*s time-resolved. The experiment is conducted in the static liquid-phase electrolyzer "FlexCell" using a 1 M $KHCO_3$ catholyte and a CO_2 gas flow of 20 mL$_n$ min^{-1}. Note: The experiment ends already after 60 minutes. Still, for better visual comparison with other experiments, the same axis excerpt is shown. 63

44 CO_2RR at a constant current density of -100 mA cm^{-2} using solely a GDL as GDE: (a) graph with the calculated *FE*s time-resolved, (b) plot of the applied current density and the resulting potential at the WE. For easier comparison, the resulting potential of the measurement of figure 43 is also shown. The experiment is conducted in the in the static liquid-phase electrolyzer "FlexCell" using a 1 M $KHCO_3$ catholyte and a CO_2 gas flow of 20 mL$_n$ min^{-1}. 64

45 CO_2RR at a constant current density of -300 mA cm^{-2} using Ag NPls added with commercial Cu NPs as catalyst with Nafion as binder and a catalyst loading of 1.4 mg cm^{-2} on a GDL: (a) plot of the applied current density and the resulting potential at the WE, (b) graph with the calculated *FE*s time-resolved. The experiment is conducted in the liquid-phase electrolyzer "FlexCell", which is modified to a flow cell, using a 1 M $KHCO_3$ catholyte and a CO_2 gas flow of 20 mL$_n$ min^{-1}. Note: The experiment ends already after 90 minutes and the gas injections are started on the catholyte side instead of the gas side. 65

46 Time-resolved *FE*s of a CO_2RR with a constant current density of -300 mA cm^{-2} using Ag NPls added with commercial Cu NPs as catalyst with Nafion as binder and a catalyst loading of 1.4 mg cm^{-2} on a GDL. The experiment is conducted in the in the liquid-phase electrolyzer "FlexCell", which is modified to a flow cell, using a 1 M $KHCO_3$ catholyte and a CO_2 gas flow of 60 mL_n min^{-1}. 66
47 Time-resolved *FE*s of CO_2RRs with a constant current density of -100 mA cm^{-2} using CuAg NPls as catalyst with two different binders and a catalyst loading of 1.4 mg cm^{-2} on a GDL: (a) with Piperion as binder [12], (b) for easier comparison, the graph with Nafion as binder is shown again (compare figure 41a) [12]. The experiments are conducted in the static liquid-phase electrolyzer "FlexCell" using a 1 M $KHCO_3$ catholyte and a CO_2 gas flow of 20 mL_n min^{-1}. 67
48 Time-resolved *FE*s of CO_2RRs with a constant current density of -100 mA cm^{-2} using CuAg NPls as catalyst with Piperion as binder and a catalyst loading of 1.4 mg cm^{-2} on a GDL: (a) using an increased CO_2 gas flow of 60 mL_n min^{-1}, (b) using a new CuAg NPls powder with a CO_2 gas flow of 60 mL_n min^{-1}. The experiments are conducted in the static liquid-phase electrolyzer "FlexCell" using a 1 M $KHCO_3$ catholyte. 68
49 Time-resolved *FE*s of a CO_2RR with a constant current density of -100 mA cm^{-2} using CuAg NPls as catalyst with Piperion as binder and a catalyst loading of 1.4 mg cm^{-2} on a GDL. The experiment is conducted in the liquid-phase electrolyzer "FlexCell", which is modified to a flow cell, using a 1 M $KHCO_3$ catholyte and a CO_2 gas flow of 60 mL_n min^{-1}. 70
50 Time-resolved *FE*s of CO_2RRs with a constant current density of -100 mA cm^{-2} using solely the Ag NPls as catalyst with Piperion as binder and a catalyst loading of 1.4 mg cm^{-2} on a GDL: (a) performed in the unmodified static liquid-phase electrolyzer "FlexCell" (b) using the static liquid-phase electrolyzer "FlexCell" modified to the "pressure mode". The experiments are conducted using a 1 M $KHCO_3$ catholyte and a CO_2 gas flow of 60 mL_n min^{-1}. Note: No liquid samples are taken. 72
51 Time-resolved *FE*s of CO_2RRs with a constant current density of -100 mA cm^{-2} using solely the Ag NPls as catalyst with Piperion as binder and a catalyst loading of 1.4 mg cm^{-2} on a GDL: (a) performed with a current pulse of +950 mA prior to the CO_2RR and in the unmodified static liquid-phase electrolyzer "FlexCell" (b) in addtion to (a) the cell is modified to the "pressure mode". The experiments are conducted using a 1 M $KHCO_3$ catholyte and a CO_2 gas flow of 60 mL_n min^{-1}. Note: No liquid samples are taken and the gas injections are started in (b) on the catholyte side instead of the gas side. 73

52 Top view SEM images of GDEs prepared with Ag NPls as catalyst and Piperion as binder taken after the CO_2RR: (a) with an applied current pulse of +950 mA for 5 s prior to the CO_2RR (b) without a current pulse. 74
53 (a) CV curves and (b) XRD patterns of GDEs using Ag NPls as catalyst with Piperion as binder and a catalyst loading of 1.4 mg cm^{-2}: Data from measurements without an applied current pulse of +950 mA for 5 s prior to the CO_2RR are depicted in black and with in green. The data are acquired after the CO_2RR. In (b), additional XRD patterns of a GDL as well as a Ag and C reference pattern from the ICS database are shown.[85] 74

C List of Tables

1 CO_2 reduction reaction (CO_2RR) products on Cu electrodes with the amount of CO_2 (x), H_2O (k), transferred electrons (z), and OH^- (y) required per molecule of product. In addition, the standard reduction potential E° at pH = 6.8 versus RHE is listed.[22] 7

2 Faradaic efficiencies (FEs) of ethanol and ethylene and their ratios for different bimetallic Cu-Ag catalysts from the literature. 10

3 List of supplier and purity of the used chemicals (ACS: Fulfills the requirements for an analytical chemical as defined by the American Chemical Society, BP and USP: Fulfills the purity requirements of the British and United States Pharmacopoeia, respectively; MEK: methyl ethyl ketone.) 21

4 Composition of the different synthesis solutions (S1: seeding solution 1, S2: seeding solution 2, P1: plating solution 1, P2: plating solution 2, and EDTA: ethylenediaminetetraacetic acid). 23